UNIVERSITÉ DE STRASBOURG

ÉCOLE DOCTORALE PHYSIQUE ET CHIMIE-PHYSIQUE

Institut de Physique et Chimie des Matériaux de Strasbourg

THÈSE

présentée par :

Kerstin BÜCKER

Soutenue le **10 octobre 2017**

Pour obtenir le grade de : **Docteur de l'université de Strasbourg**

Discipline/ Spécialité : **Physique – Chimie physique**

Characterization of Pico- and Nanosecond Electron Pulses in Ultrafast Transmission Electron Microscopy

---

THÈSE dirigée par :
  BANHART Florian   Professeur, Université de Strasbourg

RAPPORTEURS :
  KOCIAK Mathieu   Directeur de recherche, LPS – CNRS Orsay
  HYTCH Martin   Directeur de recherche, CEMES – CNRS Toulouse

---

AUTRES MEMBRES DU JURY :
  LOISEAU Annick   Directrice de recherche, LEM – ONERA – CNRS Chatillon
  RABU Pierre   Directeur de recherche, IPCMS – CNRS Strasbourg

Acknowledgment

To start with, I want to express my profound gratitude to my supervisor Florian Banhart for giving me this PhD position and thereby the opportunity to plunge into the exciting field of ultrafast TEM. I very much appreciate his trust, allowing me to explore the new instrument autonomously. And of course, I am very thankful for his guidance throughout these three years.

Very important in order to complete this PhD thesis, I want to thank all jury members and in particular those who are obliged to read through all these pages in order to write the required report: Mathieu Kociak and Martin Hytch, I am very grateful for your effort! My thankfulness also goes to Anick Loiseau and Pierre Rabu.

All this work would not have been possible without my closest coworker Matthieu Picher. I want to express my warmest thanks, not least for taking me serious from the first day on - me the PhD student who has never before worked on a TEM. Thank you for all the very constructive discussions. It was a joy to work besides you.

Equally, this work would not have been possible without the profound support of our collaborator Thomas LaGrange. You were the first person I met in the lab, when you were finishing the installation on behalf of IDES. It was a warm welcome into this exciting new field of research. With a lot of patience, you tried to teach me as much as possible in the limited time. Furthermore, your constant advise and assistance as soon as you switched back to research at the EPFL is priceless for the achievements made throughout this thesis.

Further assistance has to be acknowledged, especially of the optics department at the institute. I owe my sincere thank to Olivier Crégut, who was always ready to help with any laser issues and who patiently tried to bring nonlinear laser physics home to me. I should also thank Jean-Pierre Vola for the implementation of electronic safety features.
Similarly, other member of the institute were always happy to help. In particular, Nicolas Bayer from the facility management and workshop was instantly on site, Corinne Bouillet gave her best with any issues concerning conventional electron microscopy. For all administrative concerns I want to thank Céline Guillet.

I'd like to thank all members of the institute for welcoming me and making this place the one it is. It is impossible to name all who I owe acknowledgment, but I'll still name a few. Thanks to all members of ADDEPT. It was a joy to be part of your team and organize social and scientific events for the institute. And in particular, a very warm thanks to all PhD students and post-docs of *Place du Café*, it was an honor to be the last one joining this international group of friends centered around a coffee machine :-D. Gaël, Dominik, Ondrej, Silvia, Céline, Tindara, Julien, Manu, Florian, François, Guillaume, Dimitra, Vadym and Olga - you were my new family when I came to Strasbourg and you all left far too soon... I especially appreciate the last survivors Michael and Nicolas who supported me until the very end (or nearly).

Also, I am very grateful to Ferdaous who shared the office with me. Thank you for being there, for all the interesting discussions, for the mental support and for making every day in the office so much more joyful. I also thank Assia who took over this task for the last months. I am very happy to have met Tsiky, even though you did not spend much time in Strasbourg, you became a dear friend. To Virginie, I really appreciate all your support in whatever question I had.

Finally, I am so grateful to my family and friends back in Germany, who always support me even though I tend to disappeared abroad and hardly have time for them. And of course, I owe so much to my beloved partner. Thank you for your infinite support.

Contents

List of Abbreviations

Acronyms

CBED	convergent-beam electron diffraction
CCD	charge coupled device
DP	diffraction pattern
DTEM	dynamic transmission electron microscopy
EELS	electron energy loss spectroscopy
EXAFS	extended X-ray absorption fine structure
FEG	field emission gun
FFT	fast Fourier transformation
FWHM	full width at half maximum
IDES	Integrated Dynamic Electron Solutions Inc.
MOD	modulator
NEXAFS	near edge X-ray absorption fine structure
PINEM	photon induced near-field electron microscopy
PP	pulse picker
TEM	transmission electron microscopy
TEM_{xy}	transverse electromagnetic mode
UED	ultrafast electron diffraction
UTEM	ultrafast transmission electron microscopy
ZLP	zero loss peak

Natural Units

c	speed of light in vacuum ($= 3 \times 10^8$ m/s)
e	elementary charge ($= 1.6 \times 10^{-19}$ C)
h	Planck's constant ($= 6.626 \times 10^{-34}$ Js)
m_e	electron mass ($= 9.1 \times 10^{-31}$ kg)

Units

A	ampere
Å	ångrström ($= 10^{-10}$ m)
b	barn ($= 10^{-28}$ m^2)
C	coulomb

eV   electronvolt ($= 1.6 \times 10^{-19}$ J)

Hz   hertz

J   joule

K   kelvin

kg   kilo gram

m   meter

s   second

V   volt

W   watt

Ω ohm

Variables

C_C chromatic aberration

C_S soherical aberration

d distance

$E_{h\nu}$ photon energy

E_{kin} kinetic energy

Q charge

QE   quantum efficiency

R resistance or reflectivity

t time

t_0 time zero

U (acceleration) voltage

v speed

W work function

α convergence angle

γ relativistic Lorenz factor

Δ_0 FWHM of temporal convolution in PINEM scans

ΔE energy with

Δt temporal delay

Δt_e temporal length of the electron pulse

Δt_h temporal delay: off-axis halo - central emission

Δt_p temporal length of the photon pulse

Δt_r temporal delay: shank-emission ring - central emission

θ convergence angle

λ wavelength

ϱ_e electron current

Introduction

Since the early days researchers strive to understand the world we are living in. Looking more and more into detail, magnifying instruments emerged and development went from magnifying glasses via optical microscopes up to electron microscopes, enabling atomic resolution. However, static images are insufficient for the utmost ambitions of a global understanding. We need to observe how things move. We want to understand the dynamics. This way, underlying elementary processes can be deciphered.

We observe often that the smaller objects, the faster they tend to move, which makes their observation particularly challenging. The importance was not least emphasized in 1999 as the Nobel Prize for chemistry was awarded to Ahmed Zewail for shaping a new field named femtochemistry. [1] "Femtochemistry is concerned with the very act of the molecular motion that brings about chemistry, chemical bond beaking, or bond formation on the femtosecond time scale." [2] Indispensable prerequisite was the development of pulsed femtosecond lasers which enabled the penetration into this time scale.

Recently, a new scientific community emerged around *ultrafast transmission electron microscopy*, aiming at the combination of best real-space imaging resolution with high temporal resolution. To achieve this goal, a conventional transmission electron microscope is coupled with a fs-laser systems to operate the microscope in a pump-probe approach. This way, the temporal resolution is defined by the duration of the electron probe pulse and the capability to finely change its delay to the pump pulse, which initiates the transformation. This enhances the temporal resolution up to ten orders of magnitude in comparison to conventional TEM with continuous beams.

In 2014 a new ultrafast TEM was installed at the Institute of Physics and Chemistry of Materials in Strasbourg (IPCMS) in the frame of the national excellence program (*Investissement d'Avenir*, project EQUIPEX-UTEM). I joined as a PhD student right after the installation of the TEM and the integration of the laser system for stroboscopic operation. In fact, a two week overlap with a scientist from IDES represented an intense training course. At that time, the resolution tests presented in section 4.2.1 were carried out. The synchronization of pump and probe pulses was left for me to do, as well as "la prise en main" meaning to gain experience on how the various parameters change the performance of the microscope. My own work starts in section 4.2.2.

After three months, M. Picher joined the group as post-doctoral scientist and became a close co-worker for all instrumental studies. T. LaGrange, staff scientist at the Ecole Polytechnique Federale de Lausanne, became a valuable collaborator.

This thesis comprises two background chapters, covering a general overview on ultrafast dynamics and a more elaborated chapter on ultrafast electron microscopy. The experimental work is divided in two parts, presented in chapter 4 and 5.

The first experimental part deals with the pre-installed stroboscopic operation mode, containing a detailed parametric study which revealed fundamental electron beam dynamics and serves to formulate guidelines in order to adapt the instrument to different experimental needs.

The second experimental part covers a different operation mode, working with single, intense electron pulses. This required the implementation of an additional laser. All design, installation and integration into the existing UTEM were done in our small group around Prof. Banhart, in close collaboration with T. LaGrange, especially for the electronic coupling. Subsequently, a detailed analysis of the new system was carried out and will be presented in this chapter.

Ultrafast Dynamics

CONTENTS

This chapter presents an overview of the domain of ultrafast dynamics. Instruments based on X-rays and electron beams will be presented and discussed, differences will be considered. A historical overview will outline the development of ultrafast electron microscopy and the research groups working in this topic at the present day.

2.1   Origin of Ultrafast Experiments

Ultrafast experiments emerged around optical set-ups. Working with two pulsed laser beams, the pump-probe approach forms the basis of this domain. It allows the study of transient states by optical spectroscopy.

2.1.1   Pump-Probe Approach

The pump-probe approach became a standard technique in time-resolved experiments, when continuous detection is too slow to capture the dynamic process.

It consists of two consecutive pulses, separated by an adjustable delay. The first pulse excites the sample (pump), the second one probes the state of the sample at a given time after excitation, see schematic in figure 2.1. Repeating the experiment with different delays allows to trace the evolution of the process which happens after the excitation of the sample.
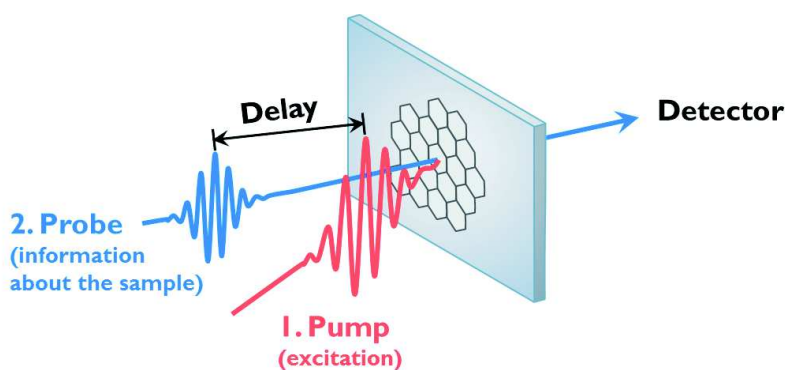

Figure 2.1: *Schematic of the pump-probe technique. A pump pulse excites the sample. The transient state is probed after a changeable delay by a probe pulse. The transmitted signal is captured by a detector.*

The nature of the observed process can be very diverse, from chemical and biochemical reactions in solution, to physical transformations such as phase change, [3] (re-)crystallization, [4] change of magnetic properties etc. [5] Also the nature of the pulses can vary enormously. For instance the sample can be excited with light pulses, other electromagnetic wavelengths (IR for heating, UV, X-rays), electric pulses or ultrasonics. As a probe pulse X-rays are very often used nowadays, but it can also be other electromagnetic radiation or an electron pulse. Finally, the detection can be done in various ways. One can measure the absorption, detect diffraction patterns or even do imaging.

In fact, the pump-probe approach is a versatile technique that can be implemented in a huge range of setups. It is upon the researcher to select appropriate conditions, in order to selectively excite the process of interest, as well as to follow a characteristic feature which gives the best information about the transformation under investigation.

The *temporal resolution limit* is primarily given by the length of the probe pulse. For instance the ongoing development in ultrashort laser technology pushes the resolution limit in optical pump-probe measurements. Nowadays, attosecond resolution can be attained. The second aspect is the capability to finely tune the delay between pump and probe, which also contributes to the temporal resolution limit.

2.2   Historical Overview

Nowadays, most published results in the field of ultrafast science are obtained using X-ray pulses from large scale facilities. With techniques such as pulse slicing [6,7] or free electron lasers [8,9] pulses around 100 fs duration can be obtained. It might be surprising that the fist time-resolved synchrotron experiments were only carried out in 1984 with a resolution of just 300 µs. [10,11] Whereas Bostanjoglo published 50 ns resolution using a pulsed electron microscope seven years earlier, in 1977. [12] Nevertheless, the field of X-ray studies evolved much faster and allows time resolved pump-probe experiments with sub-picosecond resolution as a standard method since the beginning of the 21st century. [13]

Initially, synchrotrons worked with continuous beams. They were developed to achieve electromagnetic radiation of very short wavelength for structure analysis, following the principle of resolution being limited by the wavelength of the incident beam. With *X-ray scattering* the crystalline structure of a sample can be studied, either in reflectivity from bulk material, in transmission using thin films or even liquid jets. [14] Furthermore, *absorption spectroscopy* using such high-energetic radiation provides information about the electronic or geometric structure of a sample. Near edge X-ray absorption fine structure (NEXAFS) for instance probes the excitation of core electrons into unoccupied states which deciphers the electronic structure of the sample. Information about the local chemical environment, including coordination sites and bond lengths, can be obtained using extended X-ray absorption fine structure (EXAFS). [15] However, at first these methods were limited to static measurements as the dynamics happening at the atomic scale are mostly several orders of magnitude faster than what can be resolved by detectors operating with continuous beams.

Later on, the generation of short and intense X-ray pulses from large-scale facilities enabled time-resolved pump-probe experiments. Mills and coworkers started the era of time-resolved X-ray absorption on myoglobin, studying the recombination with carbon monoxide after photolysis. [16] They used X-ray absorption spectroscopy and followed the position of the iron edge as a function of time. The CO coordinates to the iron atom sitting inside the protein. The formation of this bond changes the chemical environment of the iron and thus the position of the iron edge, making it the ideal signature to follow the recombination dynamics.

Lab size X-ray sources exist for some basic measurements. But as soon as high temporal resolution or high intensity are required, there is no way around large scale facilities (synchrotron or free-electron lasers). These offer highly intense and coherent beams, short pulses and a wide tuneability of the wavelength. A large range of science can be studied nowadays, like photochemistry, photobiology or physics in vacuum or gas atmosphere, bulk, films or liquids. [17]

However, even besides the limited beam time, X-rays are not always the ideal tool. A critical value is the ratio of beam damage versus useful scattering event, which produces the information about the sample. In general, X-rays have a scattering cross-section $10^4 - 10^6$ times lower than electrons, meaning that far higher beam intensities are needed in X-ray measurements in order to obtain the same amount of information. Therefore, X-rays often produce higher radiation damage to the sample. [18]

More importantly, the capabilities in reciprocal and real-space imaging differ significantly. X-ray diffraction is widely used. [19] The determination of crystalline structures allows the study of lattice dynamics or phase transitions. Recently X-rays are also used in terms of *diffraction microscopy* where real-space images are generated from diffraction measurements. [20] However, direct real-space imaging is the weak point. Here, electron beams achieve far better results. The ability to take high-resolution real-space images in order

to analyze single particles is the major advantage of electron microscopes. X-rays are mostly limited to diffraction measurements from bulk material.

Working with electron pulses has one major inconvenience, which is their charge, inducing repulsion and broadening effects. This drastically reduces the beam quality compared to low-dose continuous electron sources. Electron diffraction setups are very compact compared to electron microscopes, leaving less time for mutual interaction between the electrons inside a pulse. Nowadays, pulsed electron sources for ultrafast electron diffraction (UED) are widely used for the investigation of ultrafast dynamics. [21–25]

Time-resolved electron microscopy stayed relatively unknown and development went slow. The pioneering work at TU Berlin from Bostanjoglo and coworkers consisted of the implementation of *deflector plates* into a standard electron microscope. The continuous electron beam was deflected above an aperture only allowing electrons to pass through in the central position during the shifting of the beam to the other side, where it was blanked again. [12] They excited the sample with ultrasonics and studied phenomena such as phase transitions, crystallization and annealing processes or changes in magnetic material with a temporal resolution of 50 ns. [26] Their biggest issue was the low signal in such electron pulses. Ten years later they moved to another approach which is the generation of electron pulses by *photoemission* after laser irradiation of the emitter. This technique is still used today; it forms the basis of the ultrafast TEM studies presented in this manuscript. At that time, laser technology was limited to nanosecond pulses, so Bostanjoglo did not improve temporal resolution, but increased the number of electrons per pulse by two orders of magnitude. [27] With ongoing laser development, shorter laser pulses and consequently shorter electron pulses could be generated.

A totally different approach to improved temporal resolution is the use of *streak cameras*. Here, processes happening within a single electron pulse can be resolved by the use of fast deflector plates which deviate the electron beam along one axis on the camera, thus transforming one spatial dimension of the image into a temporal dimension. This limits the actual image information to the one remaining dimension. With this approach processes like gap spacing can be investigated in the nano- to microsecond regime. [28] However, only few studies were published using this approach.

2.2.1   State of the Art of UTEM Technology

A challenge apart from the pulse generation itself, is the detection of the signal, especially in terms of signal to noise ratio. Two complementary concepts have been developed to bypass this problem. Each one was promoted by a research team in the US, who took over the task to improve ultrafast TEM (UTEM). Their first results were published around twenty years after Bostanjoglos pioneering work. The group around G. Campbell and N. Browning works with one single illuminating pulse, compromising on temporal and spatial resolution by squeezing a high number of electrons into one pulse for sufficient signal. [29] In contrast, the group around Nobel prize winner A. Zewail aimed at single-electron pulses for highest possible resolution, temporally and spatially. This imposes to integrate over a huge number of pump-probe experiments in a stroboscopic approach, in order to attain adequate signal. [30] This integration entails the major disadvantage of the stroboscopic mode, as it is limited to fully reversible processes. The sample has to relax to its initial state before the next pump-probe experiment is carried out. The repetition rate has to be adapted to the relaxation time of the sample.

Nowadays, several groups around the world work with stroboscopic UTEMs, mostly based on thermionic

gun technology. Especially, former members of the Zewail group founded their own UTEM groups, e.g. in Switzerland (F. Carbone, U. Lorenz), Sweden (J. Weissenrieder) or South Korea (Oh-Hoon Kwon). The group around D. Flannigan is the first to use a self biasing FEI Tecnai instrument. [31] These groups all focus on materials science applications.

Besides, there are few other groups who work on different approaches. The team around C. Ropers built their instrument in Germany since 2010, primarily targeting fundamental physics. They were the first to realize pulsed electron beams using a field-emission electron gun. [32, 33] Nonlinear two-photon photoemission from a sharp tip produces low signal but highly coherent electron pulses, which are crucial for quantum phenomena such as Rabi Oszillations. [34] Recently, they achieved attosecond electron pulses using optical phase modulation. [35] In France, another cold field-emission electron microscope is being adapted for ultrafast operation by F. Houdelier and A. Arbouet. [36]

The complementary single-shot approach allows the study of irreversible processes. Bostanjoglo and coworkers achievd a spatial resolution of approx. 200 nm with pulse durations below 10 ns. [37] The group around N. Browning at Lawrence Livermore National Laboratory installed their instrument in 2006, improving spatial resolution by about one order of magnitude using a 30 ns UV laser for photoemission. [29] They coined the term *dynamic transmission electron microscopy* (DTEM). First studies were carried out on the mixing of metallic layers, followed by crystallization processes. [38, 39] A major improvement came along with the installation of the so called *Movie Mode*. A train of probe pulses is directed to different areas of the detector by a set of deflector plates, allowing the generation of several, temporally delayed images after the excitation of the sample. [40]

Recently, the group around J. Yang at Osaka University, Japan, also entered the single-shot TEM domain. After extensive studies and improvements in UED by the application of MeV acceleration voltages to achieve highly relativistic electrons, [41] they now implement this approach in ultrafast TEM. Due to greatly reduced Coulomb interactions of relativistic electrons they expect femtosecond electron pulses containing 10^9 electrons per square centimeter, enabling single-shot experiments with atomic resolution. [42]

Short time ago, ultrafast transmission electron microscopes were commercialized by IDES (Integrated Dynamic Electron Solutions), an American company specializing on the implementation of this technique into standard JEOL instruments. Their first commercial ultrafast TEM was installed here in Strasbourg in 2014. Until now, several groups around the world have purchased such instruments. It is an expanding field and we can expect further progress in instrumentation in the near future, as well as in its application in material science, namely the understanding of fundamental processes occurring at the nanoscale.

2.3   Ultrafast Science with Photons and Electrons

The work with photon or electron pulses leads to specific challenges. Some fundamental differences will be discussed in this section.

One obvious distinction is their nature. Photons are bosons, having an integer spin of 1, and obey the Bose-Einstein statistics. Electrons, on the other hand, have a spin of $\pm 1/2$ and belong to the class of fermions which follow the Fermi-Dirac statistics. The intrinsic charge of electrons and the resulting Coulomb repulsion effects imply that electrons can not be condensed infinitely to intense electron pulses. [43] In sharp focal points, for example, the electron density is high, thus the mutual interaction between the electrons is strongly enhanced.

By consequence, the beam properties change, such as an expansion of the pulse, a broadening of the energy profile and reduced coherence. Apart from the loss of spatial or energy resolution, the dimensions of the pulse are especially important for pulsed operation, as an expansion in the direction of propagation corresponds to a temporal elongation of the pulse.

In contrast, photons can theoretically be compressed infinitely without lowering the beam properties and reach high intensities in small volumes. Practically, the focusing can be challenging for high photon energies. Diffraction gratings or zone plates have been developed, but show low focusing efficiencies. The minimum spot size is around 20 nm. [43]

Contrary, electrons can easily be focused or deflected due to their charge by electromagnetic and electrostatic lenses. In low-dose applications, sub-atomic beam size can be achieved. As already stated, the limitation here is the interaction between the electrons, leading to a *dose-limited resolution*. For imaging, the dose-limited resolution of electron beams is still one order of magnitude better than of X-rays. [43]

Besides the manipulation and interaction inside the beam itself, also the interaction of the beam with the sample differs. For elastic scattering processes, electrons are mostly attracted by the positively charged nuclei. When passing in close proximity they are deviated from their initial path. X-rays interact with atomic electrons of the sample. [43] As for inelastic processes, electrons can lose or gain any amount of energy while passing through the sample. Photons can only be absorbed entirely; in a second process a photon of a different energy can be emitted. This leads to a stronger background in the spectroscopy of electrons compared to photons.

Regarding sample damage, this occurs for both electron and photon beams. Inelastic interactions can ionize the sample and cause radiolysis. Secondary electrons and photoelectrons can directly cause the breakage of chemical bonds, or travel through the sample and cause further damage. [18] Electron beams, having a high momentum compared to photons, can furthermore cause knock-on displacement damage. However, this process is much slower and therefore often of minor importance. [44]

Cross-sections define the probability of a certain process to happen between an incident wave or particle and another particle. The dimension is an area, usually given in barns (with $1 \text{ b} = 10^{-28} \text{ m}^2$). For the interaction of a probe beam with the sample, e.g the elastic scattering, the cross-section is an important value to estimate the part of the incident beam which actually interacts with the sample and gives the researched signal. Table 2.1 lists values for electron and X-ray beams. The latter are generally divided in two sub-categories being soft and hard X-rays, below and above a photon energy of 2 keV. [45] The scattering cross-sections (elastic and inelastic) depend on the material itself, but generally differ several orders of magnitude between electron beams and X-rays.

Table 2.1: *Typical electron and X-Ray scattering properties.*

	Electrons (at 200 keV)	Hard X-rays (8 keV)	Soft X-rays (400 eV)
Scattering cross-sections / b	$\sim 10^6$ [11]	$1 - 10$ [11]	$1 - 10^2$ [18]
Ratio inelastic/elastic scattering events	3 [18]	10 [18]	$10^3 - 10^4$ [18]
corresponding wavelength / m	2.5×10^{-12}	1.5×10^{-10}	3×10^{-9}

For imaging and diffraction an important parameter is the ratio of the inelastic scattering, which potentially harms the sample, to the desired elastic scattering. For hard X-rays it is three times the ratio of electrons,

for soft X-rays it is three orders of magnitude higher. This is the reason why R. Henderson argues that electrons should be used to outrun radiation damage. [18] Nevertheless, the destruction of a sample does not necessarily prevent measurements, as it is obvious from the technique called "diffract-before-destroy", which is well established today. [46, 47]

In summary, electrons seem to be the ideal probe considering the potential in real-space imaging and the high cross-section leading to low radiation damage. Electron beams are challenging to handle, especially in pulsed operation with a high electron density, but the advantages prove that it is worth the effort.

Ultrafast Electron Microscopy

CONTENTS

This chapter focuses on several aspects of ultrafast transmission electron microscopy. Fundamental interactions of the electron beam are presented. The generation of electron pulses are discussed, followed by a technical description of the instrument on the example of the UTEM in Strasbourg, and a presentation of the operation modes.

3.1 General

Ultrafast electron microscopy is the application of the pump-probe technique in electron microscope. Transmission electron microscopes are known for their high spatial resolution, routinely capable of imaging atomic lattices. Today's high performance microscopes reach sub-ångström resolution. [48, 49] However, conventional transmission electron microscopes (TEMs) are restricted in temporal resolution by the signal to noise ratio in the detection. For CCD cameras, which are mostly used to capture the image or diffraction pattern, the acquisition frequency is limited to the order of $\sim 10^{-2}$ s. Most nanoscale processes occur in the micro- to femtosecond domain and can therefore not be resolved.

The implementation of pump-probe experiments into an electron microscope adds the high temporal resolution. Figure 3.1 shows various material transformations arranged according to their spatial and temporal range. The red square shows the working conditions of a conventional TEM. Only slow processes such as diffusion-limited transformations or dislocation dynamics can be studied here. Whereas ultrafast TEM gives access to all processes inside the light blue rectangle, such as defect formation, phase transformations, nucleation phenomena or magnetic changes (switching of domains, remagnetization etc). The compromise is a slight loss in spatial resolution due to repulsion effects inside the electron pulse.
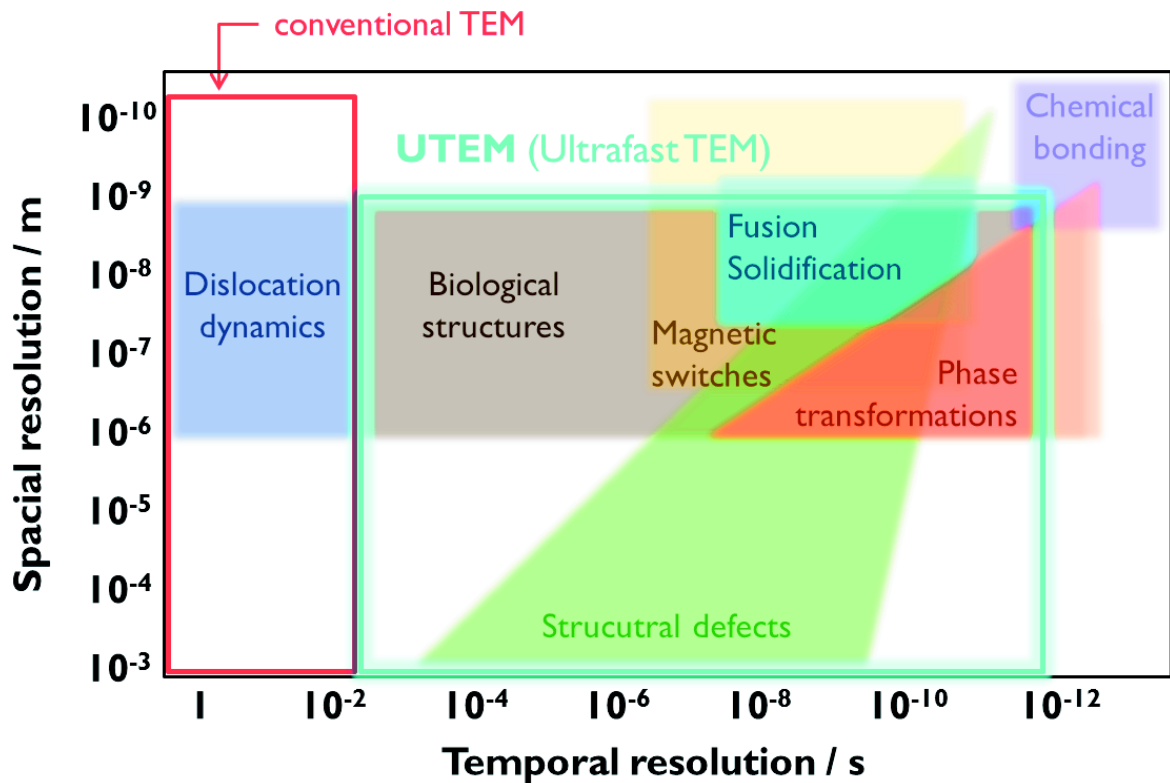

Figure 3.1: *Dynamic processes displayed according to the spatial and temporal resolution required for observation. The red rectangle shows the accessible range for conventional TEM. Encircled in light blue are all processes open to ultrafast TEM. Adapted from [26].*

The number of electrons required per image can be approximated using the Rose criterion. [50] Electron dose calculations in [51] yield a minimum of 100 electrons per pixel for an adequate image quality, which is a total of 10^8 electrons for a 1 megapixel image. Diffraction patterns require less electrons, a total of 10^4 is

sufficient. As discussed in [51], this approximation is done for bright field imaging, a detection technique requiring high signal. Furthermore, the calculations are quite conservative so these values rather serve as rough orientation.

In conventional TEM operating with a continuous electron beam, in average only one electron at a time is present in the column. The required electron dose is achieved by a suitable exposure time. Contrary, in ultrafast TEMs operating with electron pulses which contain a large number of electrons, their mutual interactions are no longer negligible. They are a major issue and will be a center of interest in chapter 4.

3.2   Fundamental Electron Interactions

3.2.1   Electron-Electron Interactions

The nature of electrons being charged particles brings along numerous challenges when working with high electron density. In the following, the main phenomena are presented.

The term *Coulomb interactions* is used as a general expression, describing repulsion effects due to the intrinsic charge of the particles. In practice, a more precise distinction is often hardly possible as many phenomena coincide. However, theoretical studies present a whole variety. These are primarily divided in homogeneous and inhomogeneous effects, depending on whether they can be modeled based on a continuous spatial charge distribution or if the stochastic nature of individual particles has to be considered. [52] Furthermore, the resulting change can occur longitudinally (in the direction of propagation) or laterally (perpendicular to the propagation).

The most important homogeneous phenomenon is the *space charge effect*, including the Child's law. The latter states a fundamental limit of electron density in a diode setup, which is defined by the applied voltage over a certain distance. [53] In the case of an electron microscope this law defines a limit to the charge density inside the accelerator, between electron emission and anode. Effectively, this longitudinal space charge effect can limit the photoemission.
The lateral space charge describes a beam expansion perpendicular to the propagation. The effect is particularly pronounced at low propagation speed, resulting in a long interaction time, and in areas of high electron density, such as focal points. The result is similar to a defocusing of the electron beam, which can be corrected in a subsequent focusing step. [54]

In contrast, inhomogeneous effects are generally not reversible by passive external fields as they present an increase in entropy. [52] Elastic electron-electron scattering changes the direction of propagation of each particle. Assessing the longitudinal component, the propagation speed is modified and thus the energy distribution within the electron beam. This aspect is named *Boersch effect*. [55] The lateral component is called *trajectory displacement*. [56] In electron microscopy the particle is shifted with respect to the optical axis, which results in a loss of resolution, and in particular a loss of phase contrast.

3.2.2   Electron-Photon Interactions

An interaction of electrons and photons in free space is not possible due to momentum mismatch. [57] Furthermore, for reasons of energy-momentum conservation a third reaction partner is mandatory to compensate

the momentum when the electron energy is changed by the absorption or emission of a photon. Thus, electron-photon interactions can only be observed in special conditions.

Still such phenomena exist. Some have been theoretically described decades ago and have later on found experimental proof. One example is the inverse Smith-Purcell effect which describes the acceleration of an electron beam by a laser near a metal grated surface. [58] It is based on a momentum shift of photons inside the optical near-field, which is created around the grated surface. In this way the mismatch is overcome in some cases and the photon energy can be absorbed by an electron. Similar is the inverse Cherenkov effect, which describes the acceleration of electrons inside a dielectric medium. [59] More descriptive is the Cherenkov effect itself. When charged particles pass through a dielectric medium with a speed higher than the speed of light in this medium, the electrons are decelerated and emit the excess energy as photons. Momentum conservation is provided by the surrounding medium. [60] The most prominent example is the blue glowing of water which surrounds nuclear reactors. The opposite process, the uptake of speed by photon absorption in a dielectric medium is called inverse Cherenkov effect.

Another possibility to overcome the mismatch issue is a momentum or energy broadening. Based on the uncertainty principle formulated by Heisenberg, for a particle which is confined in space, the momentum can not be determined precisely. Thus, using near-fields around nanoscale objects, the photon is highly restricted spatially such that the momentum turns out broad. [61] The same applies to very short, temporally confined pulses which will be broad in energy. Within this framework an electron microscopy technique has been developed, which will be presented in the following subsection.

Photon Induced Near-field Electron Microscopy

The first idea to probe local optical excitations of nanostructures by TEM was presented in 2008. [62] Following theoretical calculations on interaction probabilities, electron energy gain spectroscopy was proposed to reveal hyperfine details in the optical response of nanostructures. G. de Abajo and M. Kociak predicted the uptake of one photon energy by an electron traveling through the optical near-field, an aloof spectroscopy technique as the electrons pass in close proximity and not through the sample.

The experimental proof was published one year later by Barwick and coworkers, who named this technique photon induced near-field electron microscopy (PINEM). [63] They observed a change in electron energy during pump-probe experiments on their ultrafast electron microscope. Looking at EEL spectra, they found a dramatic change in the shape of the zero-loss peak upon temporal alignment of photon pump and electron probe pulse on the sample, see figure 3.2. The black curve shows the unperturbed zero-loss peak of an electron pulse arriving 2 ps before the photon pulse. The red spectrum is taken at temporal overlap. The intensity at 0 eV is greatly reduced, new peaks appear at each side of the ZLP. The distance between two peaks is exactly one photon energy. This shows that electrons can gain or lose entire quanta of $h\nu$ while passing through the optical near-field, which is in accordance to the predictions. The inset shows that an uptake of up to 8 $h\nu$ can been observed. Profound theoretical investigation on this subject can be found in [57, 64, 65].
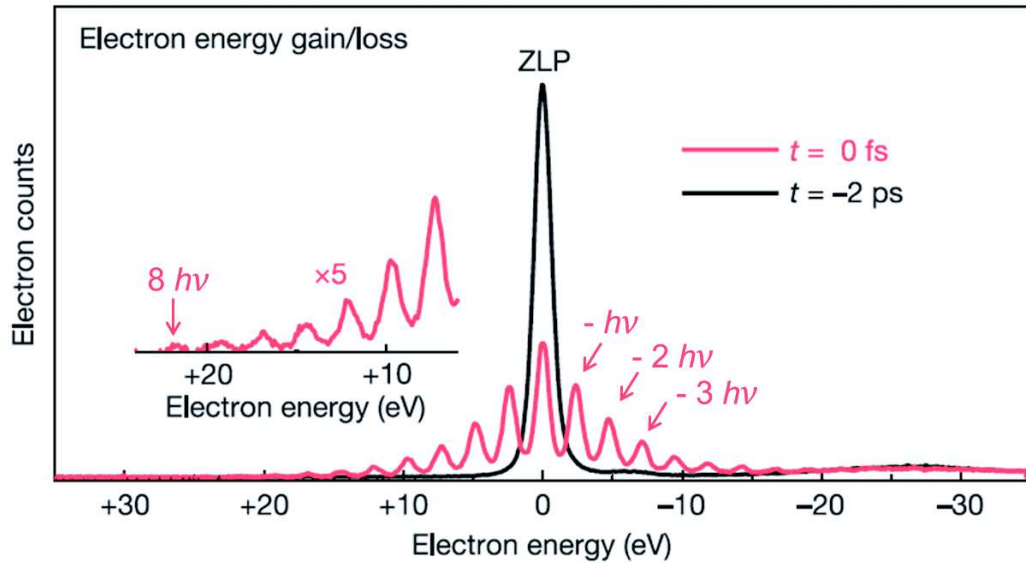
Figure 3.2: *Electron energy loss spectra of silver nanowires irradiated with an intense fs laser pulse. The zero-loss peak is shown before the arrival of the photon pulse (black) and at temporal overlap with the photon induced near-field (red). Inset: Positive energy range multiplied by 5, indicating the absorption of up to 8 quanta of photon energy. Adapted from [63].*

Photon induced near-field electron microscopy or spectroscopy can be used to study the presence of the optical near-field. By analyzing the zero-loss peak, information about the existence, strength and orientation can be gained. With appropriate equipment energy filtered images can be taken. For instance by selecting only side-band electrons to form the image the near-field can be visualized. Figure 3.3 shows two examples. The first one presents a biological sample. Flannigan *et al.* demonstrate the temporal evolution of the near-field, as well as a dependency on the orientation of the linearly polarized laser which generates the near-field. The second example uses multi-layered graphene, where the edges of graphene sheets are greatly enhanced in PINEM, in conventional bright-field imaging the layers are hardly visible as contrast is weak.
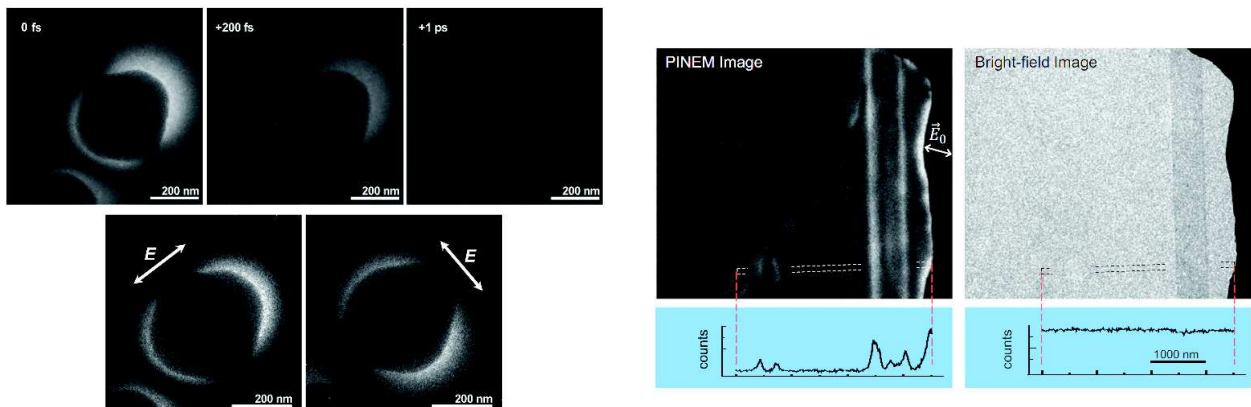
(a) *Protein vesicle, shown in the top row at different time delays. Bottom row: PINEM images generated with differently polarized fs laser light. Taken from [66].*

(b) *Graphene layers, imaged with PINEM and conventional bright-field imaging. Image intensity profiles from the dotted area are shown below each image. Taken from [67].*

Figure 3.3: *Literature examples showing advantages of PINEM images. The temporal profile and polarization dependance of the near-field can be studied. Also, it can hugely enhance the contrast of light samples giving almost no Z-contrast in conventional TEM.*

In [68] Plemmons *et al.* demonstrate a detailed temporal analysis by modeling electron energy loss spectra. Changing the delay between optical pump and electron probe pulse, the evolution of the photon-electron-interaction is obtained. In figure 3.4a the calculated time-dependent energy spectrum is displayed. Each spectrum corresponds to a vertical line with the intensity shown in false colors. The intense zero-loss peak is visible as the colorful horizontal line in the middle of the plot. Around time $t = 0$ parallel side-bands appear, corresponding to the gain or loss of entire quanta of the photon energy.
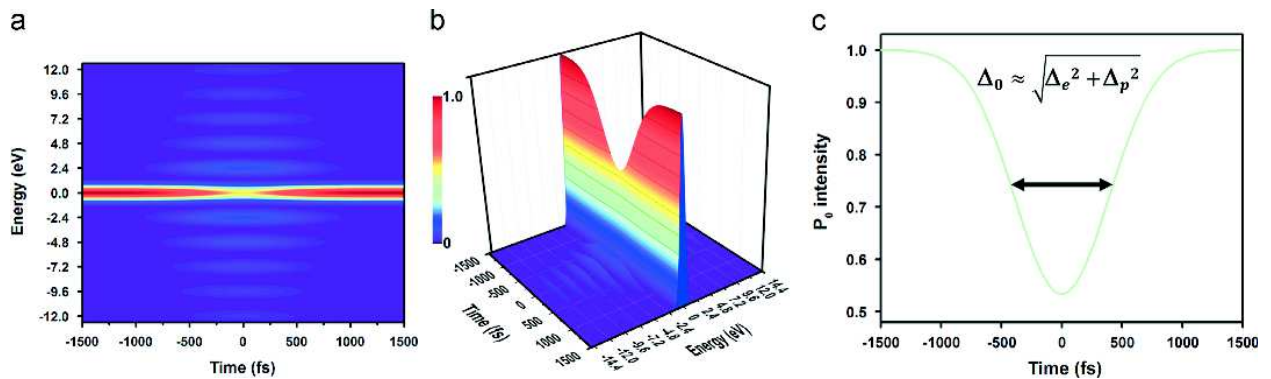

Figure 3.4: *Calculated temporal evolution of the electron energy spectrum. (a) 2D and (b) 3D representations of the time/energy phase space, intensity displayed in false color. (c) Temporal cross-section of the zero-loss peak. At weak-interaction limit the full width at half maximum can be approximated as the convolution of electron and photon pulse duration (Δ_0). Taken from [68].*

In the three dimensional plot (figure 3.4b) the depletion of the zero-loss intensity is clearly visible as the inverted Gaussian shape, which is extracted in figure 3.4c. At weak-interaction limit this temporal cross-section of the zero-loss peak can be approximated as the convolution of the electron and photon pules.

$$\Delta_0 \approx \sqrt{\Delta_e^2 + \Delta_p^2} \tag{3.1}$$

with Δ_0: FWHM of cross-section, Δ_e: electron pulse,
Δ_p: optical photon field.

This equation clarifies, that either the photon pulse and its corresponding near-field can be studied with a known electron probe, or the reverse which is to probe the electron pulse with a known optical field. In fact, photon induced near-field microscopy is an ideal tool in ultrafast TEM as it gives access to the electron pulses "hidden" inside the microscope. Furthermore, it can be used for the synchronization of the optical pump and the electron probe pulses.

3.3   Electron Pulse Generation

The *external photoelectric effect* is a widely used mechanism to generate electron pulses in ultrafast electron microscopy. Electrons are emitted from bulk material after photon irradiation. In order to estimate the amount of electrons actually leaving the bulk material into the vacuum a number of effects have to be considered.

Figure 3.5 shows the amount of emitted electrons (as photoemitted charge Q) versus the laser power at constant wavelength. The dependency is not linear but shows *saturation* characteristics. This intrinsic limitation of the material is due to electron transport mechanisms in the bulk, which limit the photoemission

at high laser power.The maximum efficiency of the photoelectric effect can be determined from the slope in the low-energy regime, where saturation does not play a role. It is called the *quantum efficiency* (QE), defined as the number of electrons per number of photons. In this example of LaB$_6$ $\langle 100 \rangle$ it is 2.4×10^{-4} for photons of 355 nm wavelength.
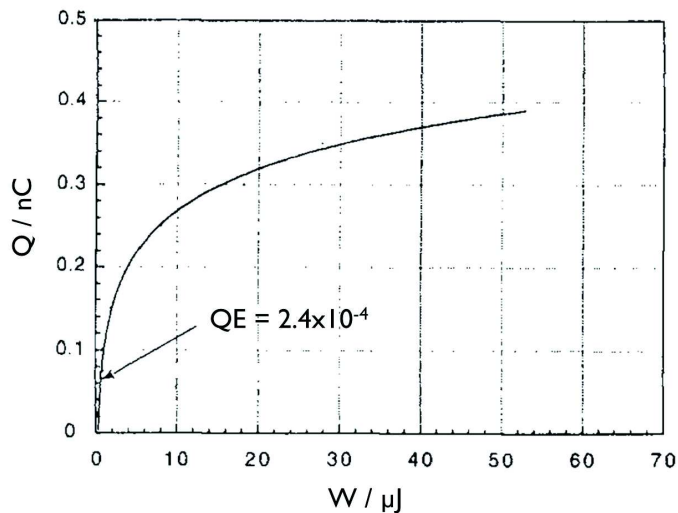

Figure 3.5: *LaB$_6$ $\langle 100 \rangle$: Photoemitted charge as a function of the laser power (at 355 nm). The slope at low laser energy represents the quantum efficiency. Adapted from [69].*

Interestingly the quantum efficiency does not only depend on the material itself, but it varies hugely with the photon energy, as it can be seen in figure 3.6. The decimal power of the quantum efficiency is shown on the vertical axis as a function of the photon energy $h\nu$.
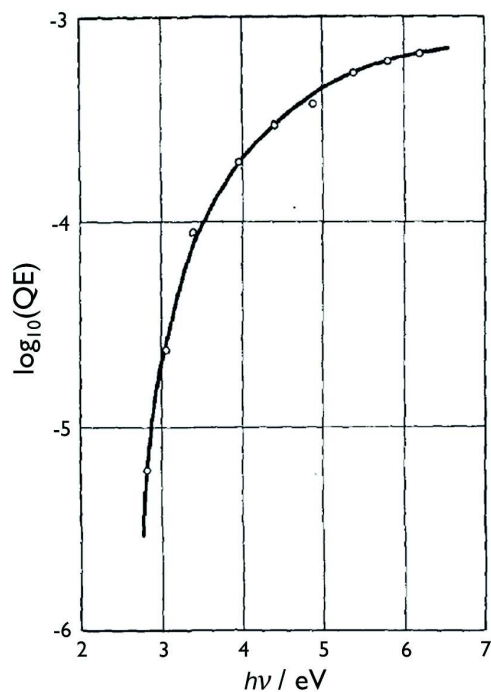

Figure 3.6: *Dependance of the quantum efficiency as a function of the photon energy for LaB$_6$. Adapted from [70].*

The quantum efficiency correlates with the square of the photon energy, which is described by the Fowler law,

see equation 3.2. [71] Thus, the choice of the laser wavelength is crucial for the performance of a photocathode. A good quantum efficiency can only be achieved with lasers of short wavelength. Besides, the Fowler law is regularly used to determine the work function of a material. [72,73]

$$QE \propto (E_{h\nu} - W)^2 \qquad (3.2)$$

Fowler law, with QE: quantum efficiency,
$E_{h\nu}$: photon energy, W: photoelectric work function.

For LaB_6 a common UV laser of 266 nm wavelength has a quantum efficiency of approximately 5×10^{-4} electrons emitted per absorbed photon. The difference between the photon energy and the work function results in a kinetic energy of the emitted electrons:

$$E_{h\nu} = W + E_{kin} \qquad (3.3)$$

with $E_{h\nu}$: photon energy, W: work function, E_{kin}: kinetic energy.

In this example, the photoemission from LaB_6 ($E_{h\nu} = 4.66$ eV at 266 nm, $W_{LaB_6} = 2.6$ eV) results in a kinetic energy of 2 eV. The attempt to increase the quantum efficiency by using higher photon energies will result in a higher kinetic energy of the electrons. As a low initial kinetic energy spread is mandatory for high resolution UTEM and in particular for electron energy loss spectroscopy, the standard emitter used in electron microscopes is not ideal.

The group at Lawrence Livermore around N. Browning chose tantalum as emitter. It has a work function of 4.1 eV [74] and provides a quantum efficiency of 10^{-5} at 4.8 eV photon energy. [75] The resulting kinetic energy spread is only 0.6 eV. All trends discussed previously for LaB_6 remain valid, but the exact values differ for each material. For instance an increased photon energy will always increase the quantum efficiency.

A closer look at the *work function* reveals that literature mostly lists average values for each material. In fact the work function depends on the crystallinity, as can be seen in table 3.1. In single crystal photocathodes this detail needs to be considered. But most cathodes are polycrystalline and the laser beam diameter is large compared to the grain size of the crystal domains, thus the use of the averaged value is appropriate.

Table 3.1: *Work function of tantalum for different crystal orientations.* [74]

W / eV	$\langle 110 \rangle$	$\langle 100 \rangle$	$\langle 111 \rangle$	polycrystalline
Ta	4.95	4.10	3.95	4.1

These theoretical considerations show an upper limit for the photoemission. In reality further difficulties have to be overcome. First of all, every surface has a certain reflectivity. Reflected photons are subtracted, even before the quantum efficiency is considered. Second, every emitter has a damage threshold above which ablation and evaporation occur, which correlates with the laser power. Consequently, the laser power can not be increased infinitely for compensation. And third, there is negative charge accumulating at the surface of the material, hindering further electron emission. The application of an external field can help by accelerating free electrons away from the surface. And even more, an external field can change the potential barrier experienced by electrons while leaving the bulk into the vacuum.

A practical aspect regarding the work function is contamination on the surface. This also changes the work function. Hence, it is important to clean the photocathode regularly, usually done by heating to evaporate impurities.

A UTEM requires a high number of electrons per pulse for sufficient signal to noise ratio while maintaining a low initial energy spread (E_{kin}). A good compromise is the use of tantalum as photocathode material in combination with an ultraviolet laser.

3.4　Ultrafast Transmission Electron Microscopes

3.4.1　General Presentation of the Instrument

In the following, all major components of the ultrafast electron microscope are presented. A special focus lies on the particularities correlated to the implementation of the laser system and the operation of the microscope using electron pulses. A schematic is displayed in figure 3.7, showing an ultrafast TEM with thermionic electron gun and Wehnelt assembly.
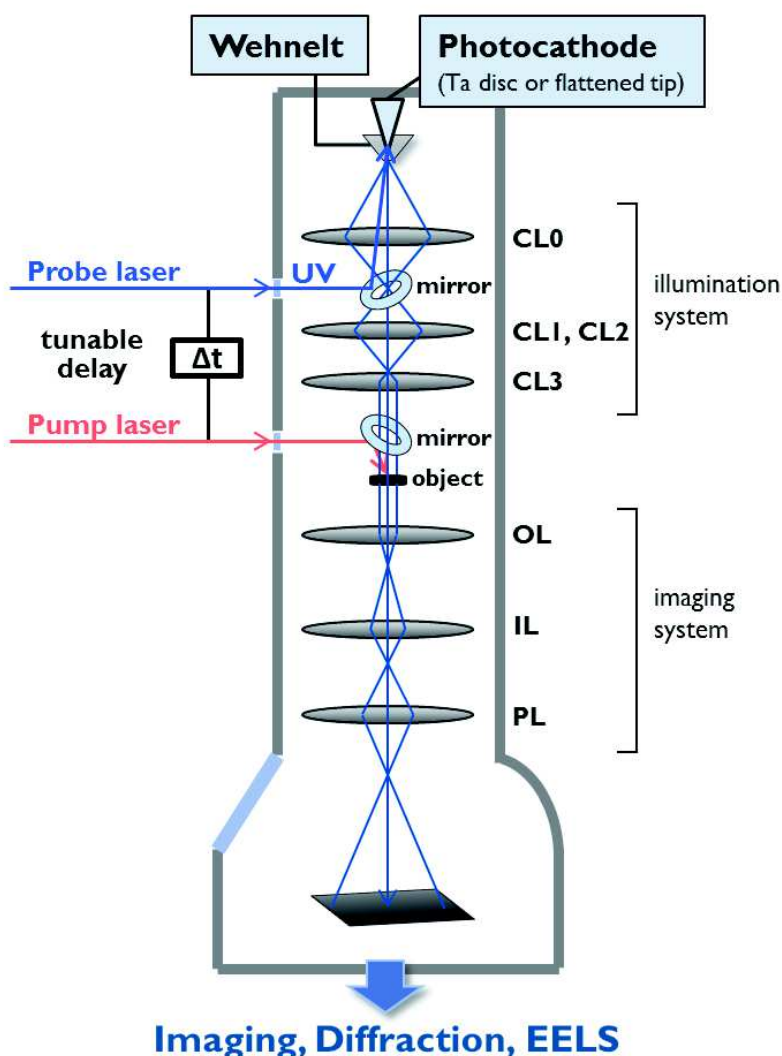

Figure 3.7: *Schematic drawing of the ultrafast transmission electron microscope with thermionic gun and Wehnelt electrode. Two synchronized lasers are coupled into the microscope, one pump laser (red) to excite the sample and the probe laser (blue) to generate electron pulses.*

Electron Gun

Transmission electron microscopes consist of a vertical column, evacuated and X-ray shielded. At the top of the column, the electron gun is located, for which two main concepts are established. A thermionic electron gun relies on the emission of electrons from a hot surface. The emitting filament is heated by an electric current above a threshold temperature, where surface electrons possess enough energy to overcome the work function and leave the bulk material. The filament can be made of various materials and have different shapes. The other concept is a field emission gun (FEG). Here, an electrostatic field is applied to a very sharp tip, which lowers the potential barrier and bends the band structure in such a way that electrons can leave the bulk by tunneling through the barrier. Field emission guns provide highly coherent electron beams, ideal for quantum or interference experiments, e.g. holography. The thermionic gun is a more robust setup, mostly used for material sciences or biological samples. In the following, a thermionic UTEM will be described.

In this case, the emitting filament is called *photocathode*, as the electrons will be emitted through laser irradiation due to the external photoelectric effect. Special requirements have to be considered. First, the cathode has to stay cold during photoemission. A continuous background emission would blur the electron pulse and lower the temporal precision. Second, the cathode surface needs to resist the intense laser irradiation without ablation or surface reconstruction in order to guarantee a reproducible photoemission. Normally, a tip-shaped cathode is used to achieve best coherence (ideally emission happens in one single point). For the emission of intense electron pulses a bigger surface is advantageous. A sharp tip can not deliver a sufficiently high number of electrons (up to 10^{10} are needed). Appropriate shapes are a truncated cone (flattened area of several micrometers) or a disc of several hundred micrometers in diameter. With a laser spot of approximately 150 μm in diameter, the disc allows the highest electron flux due to the large emission area. However, the electrons are less coherent. Consequently, the cathode shape is the first parameter to compromise between electron beam intensity and coherence depending on the needs of the experiment.

Wehnelt Electrode

The photocathode is enclosed by a Wehnelt assembly with an adjustable bias. The Wehnelt is a metallic cone with a small circular opening at the bottom (~1.2 μm). A schematic is displayed in figure 3.8. A high voltage (acceleration voltage) is placed between the cathode and the anode, modified by a potential on the Wehnelt which makes the Wehnelt cone more negative than the cathode. This bias voltage is variable. It contains a self-biasing loop, which adjusts to an averaged electron emission current, and several resistors tunable by the operator. The self-biasing is only effective in thermionic emission. In pulsed operation the averaged current is too low.

The Wehnelt bias voltage induces an electrostatic field. This defines the emission area on the cathode and represent a potential barrier for the electrons on their way through the opening towards the anode. At the same time, the electric field act as an electrostatic lens focusing the emitted electrons onto the optical axis. It forms a first cross-over (referred to as *gun cross-over*), with a certain diameter and convergence angle, which is the virtual source (object) for the subsequent lenses in the TEM illumination system.
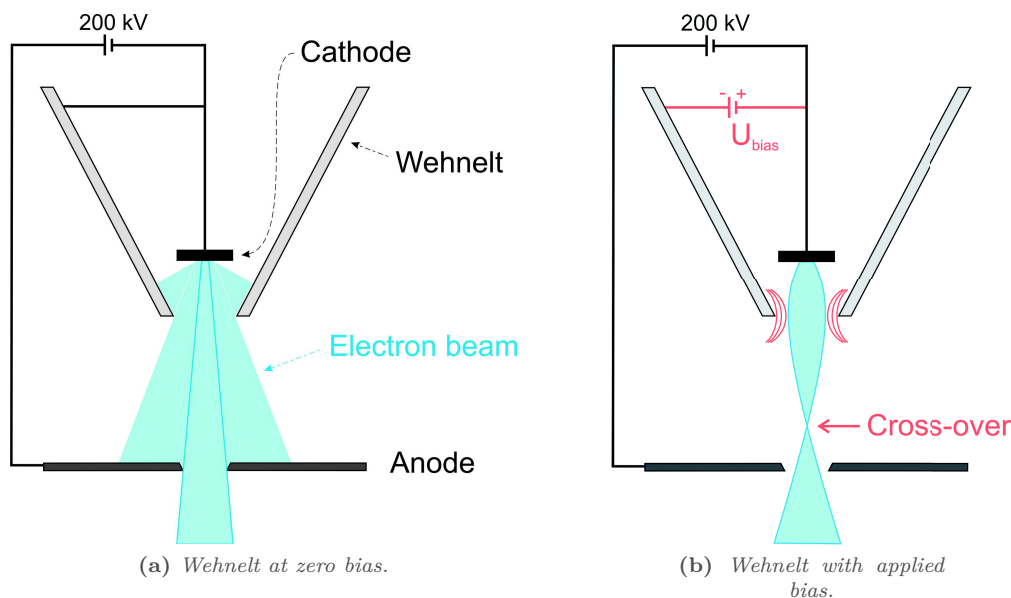
(a) *Wehnelt at zero bias.*   **(b)** *Wehnelt with applied bias.*

Figure 3.8: *Schematic drawing of the photocathode inside a Wehnelt assembly. The adjustable bias collects the emitted electrons and focuses the beam into a gun cross-over and through the anode.*

At low bias voltage many electrons are lost inside the Wehnelt cone as they are not focused onto the optical axis. At high bias, most electrons are collected and focused into a sharp gun cross-over with a high convergence angle.

Laser System

The integration of the laser beams into the TEM column requires some additional components. The beams are coupled into the microscope column through fused silica windows, mirrors are installed in the optical axis to project the beam onto the cathode or the specimen respectively. These mirrors have a drilled hole to let the electron beam pass through. Symmetry is an important issue here. The electron beam has to be symmetrically surrounded by the mirror, otherwise contamination immediately causes a deviation of the electron beam. The hole is small compared to the diameter of the mirror. Ideally, the laser beam is positioned right next to the hole, in closest proximity to the optical axis.

The UV laser is called *probe laser* even though it is not directly our probe beam, but it generates the probe electrons by photoemission. A tantalum or molybdenum mirror is used inside the microscope to direct the laser onto the cathode. The integration of the optical components required an extra segment between the anode and the illumination system. In order to compensate for the elongation of the column, an additional condenser lens (CL0) was installed right below the anode. It allows to focus the electrons through the hole of the mirror, but also to collect electrons emitted in a high angle. Evidently, the coherence will decrease when electrons of a large range of emission angles are mixed. However, as mentioned before, it is crucial for pulsed operation to maximize the number of electrons per pulse to obtain sufficient signal intensity. Thus, the CL0-lens is a key to compromise between signal and coherence.

For the excitation of the sample a second pulsed laser beam, the *pump laser* beam, is integrated. Herefore, an aluminum mirror is positioned right above the objective pole piece, which projects the laser beam onto the sample. The use of short laser pulses is crucial for quasi instantaneous excitation, in order to have a well

defined start of the reaction. The wavelength of the pump laser depends on the material transformation, e.g. infrared radiation for thermal excitation or visible light for optical processes.

Finally, the two laser beams have to be synchronized. The path length of the pump laser has to be compared to the entire probe assembly containing the UV laser path, as well as the path of the electron pulse with a delay for emission, acceleration and propagation until reaching the sample. Ultimately, a *tunable delay* is a mandatory component for pump-probe experiments. This can be either an optical delay line, changing the path length of one laser beam with respect to the other, or an electronic delay connected to the laser hardware.

An adequate laser needs to fulfill several requirements. The wavelength has to match the work function of the cathode material, the pulse energy needs to match the required number of electrons per pulse, including all losses and the specific quantum efficiency, the repetition rate must be adapted to the experimental needs. Bedsides, the *laser profile* plays an important role. The most prominent shapes are Gaussian and flat-top, which differ in their transverse electromagnetic mode (TEM_{xy}).

For photoemission of intense electron pulses, Coulomb interactions are a big concern. These can be minimized when the electron density is evenly distributed, especially at the cathode. This requires a uniform photoemission which can only be achieved if the laser intensity is homogeneously distributed throughout the laser pulse (transverse and longitudinal). With this reasoning, flat-top laser beams are ideal. However, the optical setup is challenging, as a flat-top beam presents a complicated shape of oscillations in the focal point. To maintain the homogeneous flat-top profile the beam can not be focused onto the cathode but the image has to be relayed and downsized by telescopes. These optics are sensitive and thus not very convenient in their application.

The use of a Gaussian laser profile allows simplified optics as the beam can be focused onto the cathode. The alignment is more robust and user-friendly. The downside is a non-uniform intensity distribution, a non-uniform photoemission and therefore increased Coulomb interactions for pulses comprising the same number of electrons. Still, most ultrafast electron microscopes operate with Gaussian shaped laser beams (TEM_{00}). Evidently, the beam profile needs to be supervised in order to avoid multi-mode contributions which might arise from slightly damaged optics.

3.4.2 Techniques of Ultrafast TEM

In the development of ultrafast electron microscopy two operation modes have emerged. The application area of these techniques which will be discussed here.

Stroboscopic Mode

The stroboscopic mode was mainly promoted by the group around A. Zewail at Caltech. The aim is best spatial and temporal resolution. Therefore, the electron pulses are as short as possible, ideally containing one single electron. The compromise is the integration over thousands or millions of pump-probe experiments in order to accumulate sufficient information content for a meaningful result. This process is repeated at different time delays between pump and probe in order to collect data throughout the whole process under investigation.

A femtosecond laser system is used in this setup. The laser output is split in two beams, one serving as pump beam exciting the sample, the other is used to generate the electron probe pulses. Therefore, the fundamental infrared laser beam is frequency quadruplicated to yield ultraviolet photons for efficient photoemission. A schematic drawing is shown in figure 3.9. An optical delay is installed in one laser beam, changing the path length with respect to the other beam.
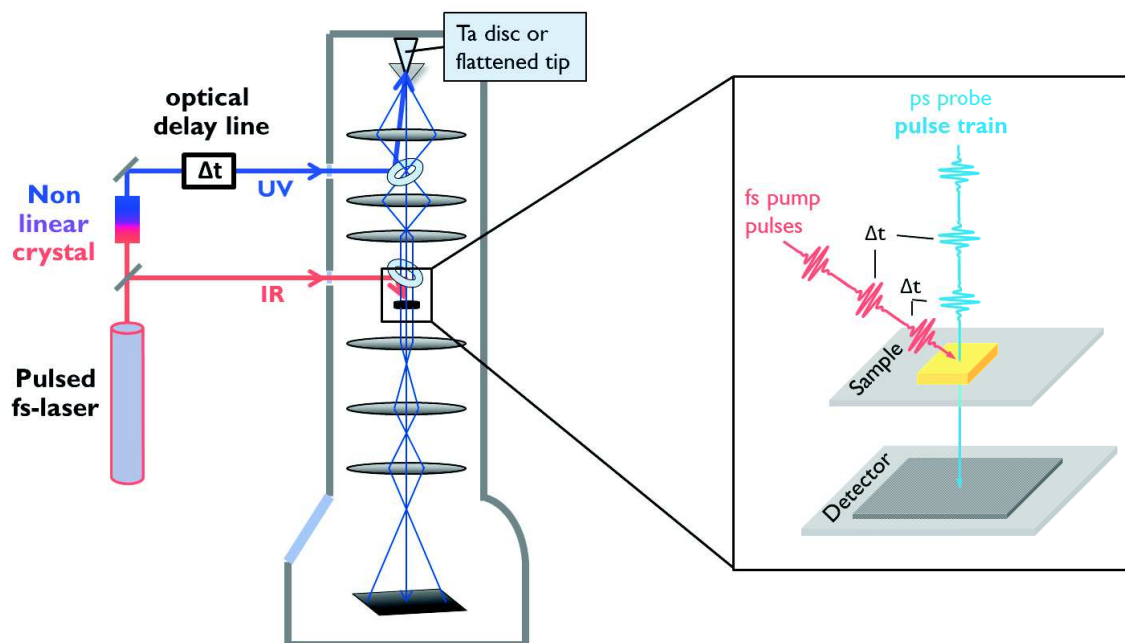

Figure 3.9: *Schematic drawing of the stroboscopic operation mode. In the left part shows the integration of the laser system into the TEM. A femtosecond laser system is used, the output is split in pump and probe beam. The right part demonstrates the situation at the sample during the experiment. A train of short electron pulses is accumulated, by repeating the same pump-probe experiment.*

During the experiment, trains of pulses are sent onto the sample, each pair of pump and probe pulse separated by the same temporal delay. The repetition rate of the laser defines the time between two consecutive pump-probe experiments, and has to be adapted to the relaxation of the sample, ensuring a complete recovery of the initial state. This brings along the biggest disadvantage of the method, which is the limitation to perfectly reversible processes. Furthermore, the sample has to endure a large number of excitation-relaxation cycles without deterioration. Finally, any drift of the sample during the acquisition is detrimental.

The feasibility of the operation with single-electron pulses is highly questioned, especially for real-space imaging. According to the Rose criterion a total of 10^8 electrons are needed for sufficient image quality (signal to noise ratio on the detector). Considering a repetition rate of 1 MHz and the general loss of 99% of all electrons throughout the TEM column, an exposure time of three hours is obtained. This seems impossible regarding sample drift. Single-electron pulses may be manageable for spectroscopy and diffraction experiments, where exposures integrated over $10^4 - 10^5$ electrons have a sufficiently high information content for good quality results. Also, a slight sample drift is not dramatic. However, a stroboscopic UTEM intended to work in imaging mode has to use multi-electron pulses.

Using a femtosecond laser system, the spatial pulse length is in the sub-millimeter domain (e.g. 0.1 mm for 400 fs pulses). A multi-electron pulse suffering from Coulomb interactions and beam expansion generally loses one order of magnitude in temporal resolution relative to the laser, resulting in the picosecond regime. Regarding spatial resolution, phase contrast imaging is possible yielding atomic resolution.

Single-Shot Mode

The complimentary approach is the single-pule mode, which has primarily been developed in the group around N. Browning at Lawrence Livermore National Laboratory. Here, one single electron pulse is used to form the image. This opens UTEM to irreversible processes, a fundamental achievement on the expense of resolution. In order to capture a materials transformation, the experiment has to be repeated on a different sample area for every delay, or a train of probe pulses has to be used. The latter adds high demands on the detector system.

In general, the single-shot setup requires the use of two laser systems. The excitation of the sample is identical to the stroboscopic mode. A fs-pump laser insures the quasi instantaneous excitation in order to have a well-defined start of the reaction. The generation of the electron probe pulse is done by a nanosecond laser. Figure 3.10 shows a schematic drawing. The coupling of the two lasers is done electronically, including an electronic delay.
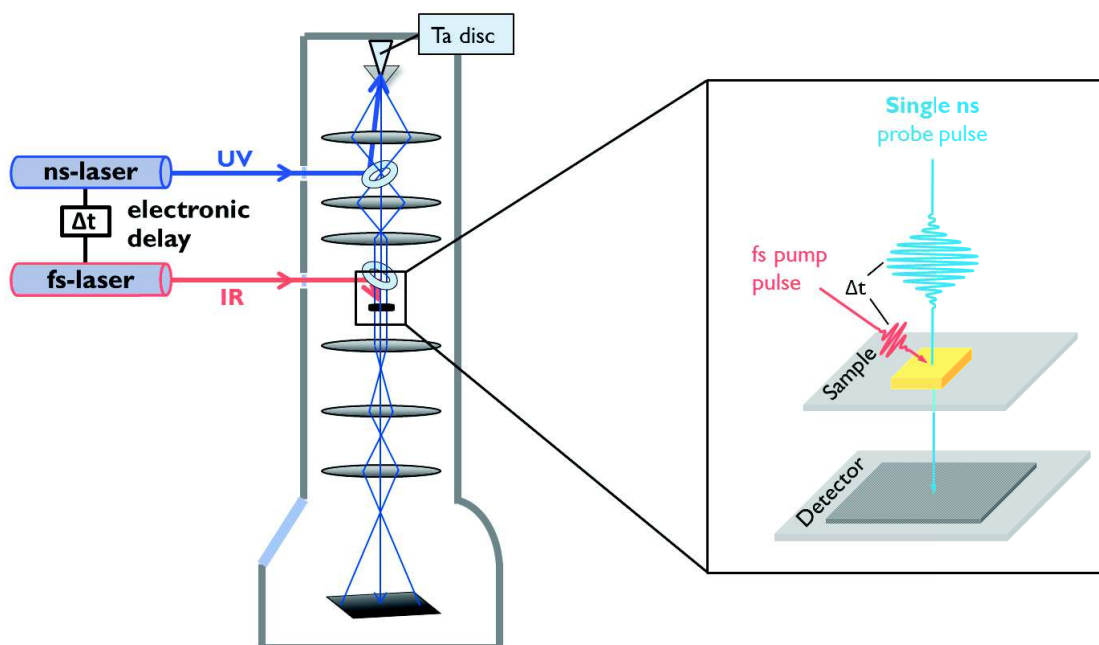

Figure 3.10: *Schematic drawing of the single-shot operation mode. In the left part shows the integration of two lasers, a femtosecond pump laser and a nanosecond probe laser to generate intense electron pulses. The right part demonstrates the situation at the sample during the experiment. One single electron pulse is used to form the image.*

The necessity for a nanosecond laser system arises from the required number of electrons per pulse. One single pulse has to contain all electrons needed for the formation of an image, diffraction pattern or spectrum. Considering the pronounced losses within the column, around 10^{10} electrons should be generated at the gun for single-shot imaging. To achieve such high numbers, it is inevitable to use longer UV laser pulses compared to stroboscopic operation. Keeping the electron density roughly in the same order of magnitude, a pulse length of several nanoseconds has been found a good compromise. This corresponds to a length of meters. The resulting spatial resolution is in the nanometer regime with scattering contrast being the main contribution in imaging.

Stroboscopic UTEM - A study of Electron Pulse Dynamics

CONTENTS

This chapter contains the first experimental part of my thesis. A parametric study of the stroboscopic operation mode will be presented, aiming at a fundamental understanding of the electron beam dynamics. Furthermore, guidelines will be formulated to help choosing appropriate settings depending on the experimental needs. This knowledge will serve as a basis for materials sciences applications.

4.1   The Stroboscopic Setup

The ultrafast transmission electron microscope in Strasbourg is the first "commercial" UTEM. It is based on a JEOL 2100 with thermionic gun and Wehnelt electrode with adjustable bias. The standard cathode has been replaced by tantalum, either in the shape of a disc (840 µm in diameter) or a truncated tip (90° angle, flattened area 16 µm in diameter).

The TEM has further been modified by the company Integrated Dynamic Electron Solutions Inc. (IDES) who added the optical components. This includes two optical tables, which are attached to both sides of the microscope column, using the same anti-vibration system to improve the stability of the system. Furthermore, two optical quartz windows and aluminum mirrors have been integrated into the TEM column. The first pair is positioned right above the pole pieces to direct the pump laser beam onto the sample (referred to as *IR-window* and *IR-mirror*), the second pair sits above the condenser system to send the probe laser beam towards the photocathode (*UV-window* and *UV-mirror*). As described in section 3.4 an additional condenser lens *C0*, as well as a drift section have been added to collect higher angle electrons at the expense of coherence.

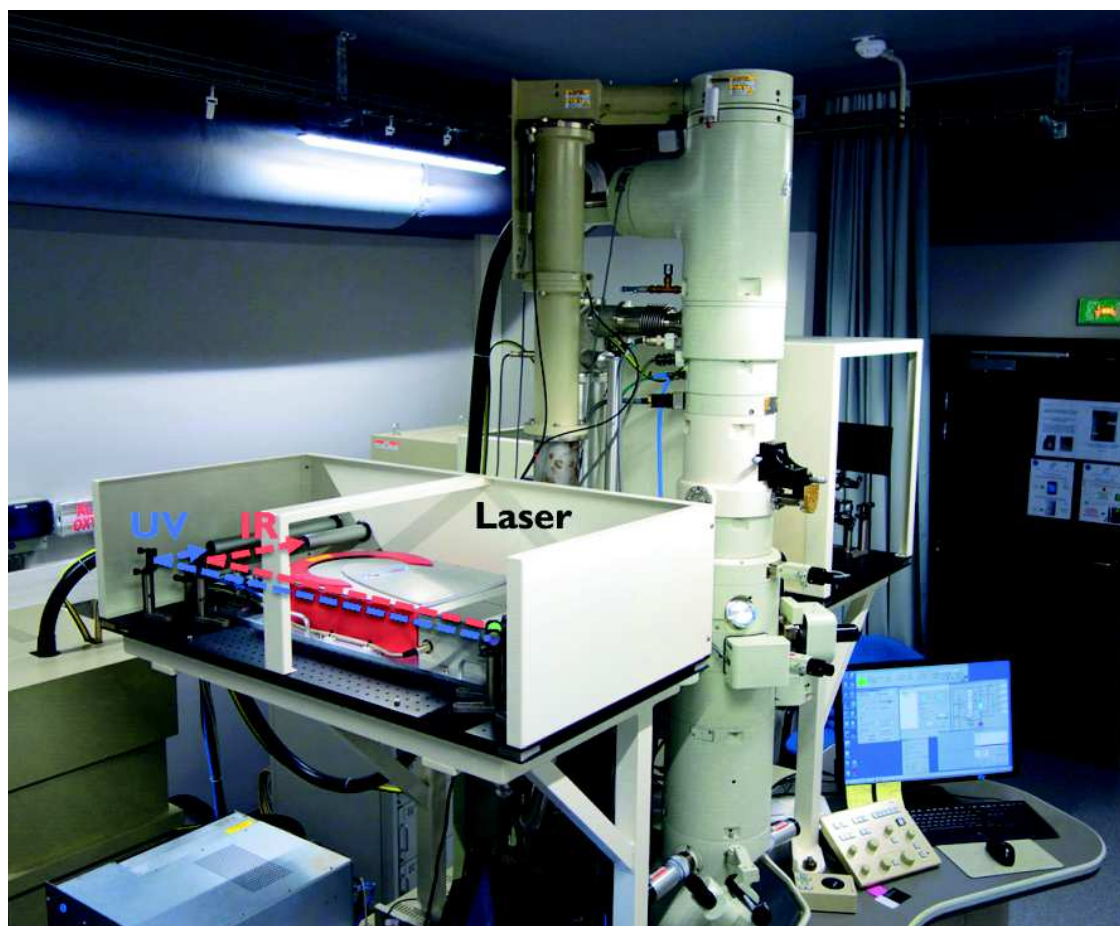Photos taken right after the installation of the setup are shown in figure 4.1 and 4.2.

Figure 4.1: *Photo showing the UTEM in Strasbourg. The left optical table contains the laser head with the UV module.*
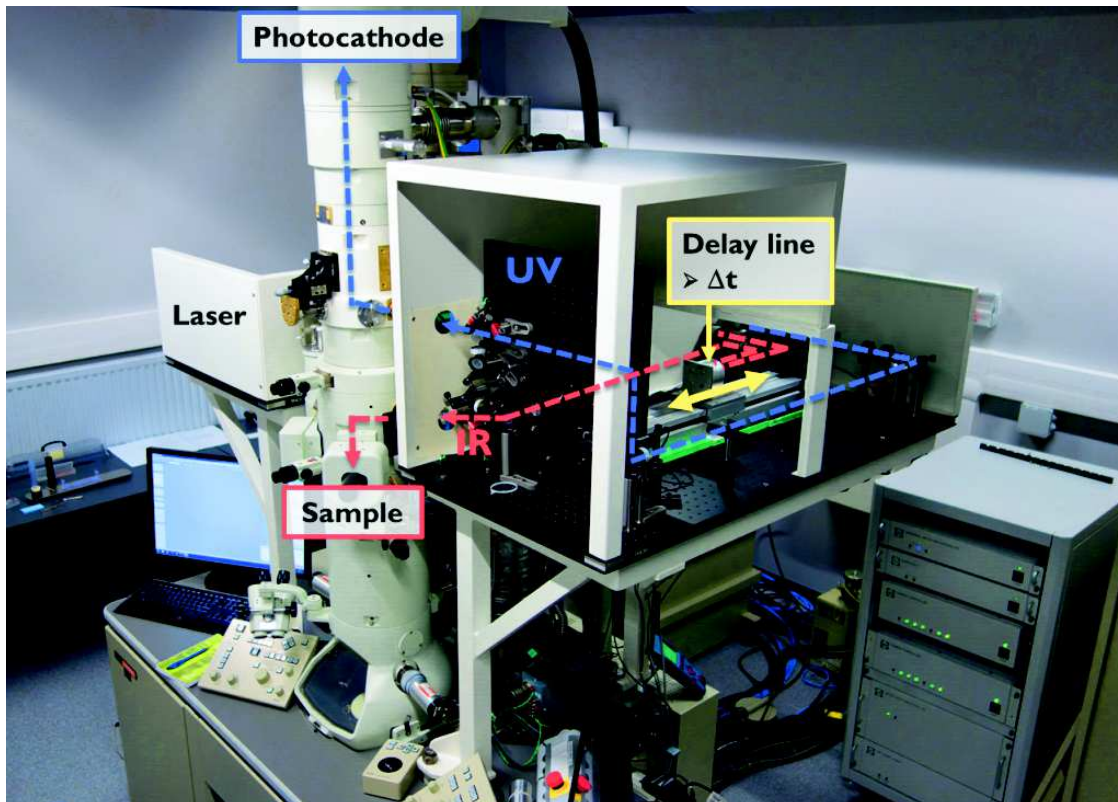
Figure 4.2: *Photo showing the right side of the UTEM in Strasbourg. The right optical table contains most optical components, in particular the optical delay line.*

The optical system is based on the femtosecond fiber laser Satsuma from Amplitude. It comprises two UV-modules for fourth harmonic generation, optimized for low and high repetition rates (below or above 2 MHz). The laser profile is Gaussian shaped. Table 4.1 lists the specifications of the laser system. The converion efficiency from IR to UV scales nonlinearly with the input IR power. Detailed measurements can be found in the appendix A on page 103.

Table 4.1: *Specifications of the Amplitude Satsuma fiber-laser system.*

fundamental wavelength	1030 nm
4th harmonic	258 nm
pulse duration	370 fs
repetition rate	0 - 40 MHz
total power IR	10 W

The laser wavelength and especially its fourth harmonic have been chosen with respect to the work function of the photocathode material. Tantalum is used as photoemitter, which has an average work function of 4.1 eV. [74] The 258 nm laser corresponds to a photon energy of 4.8 eV, resulting in an intrinsic kinetic energy spread of 0.7 eV according to equation 3.3. The quantum efficiency is 10^{-5}. [26] As shape of the tantalum emitter a disc or a truncated tip will be chosen according to the experimental requirements. Advantages of each shape are investigated in detail throughout this chapter. The high repetition rate allows greatly reduced acquisition times, in the limit given by the recovery of the sample.

A schematic of the optical tables is presented in figure 4.4. The left table supports the laser head. A combination of half-wave plate and polarizing beam-splitter prior to the UV-module allows to vary the amount of infrared radiation which will be converted to UV. Herefore, the half-wave plate rotates the linear polarization of the fundamental beam. Depending on the angle different fractions of the beam are transmitted or reflected at the beam splitter, see schematic in figure 4.3.
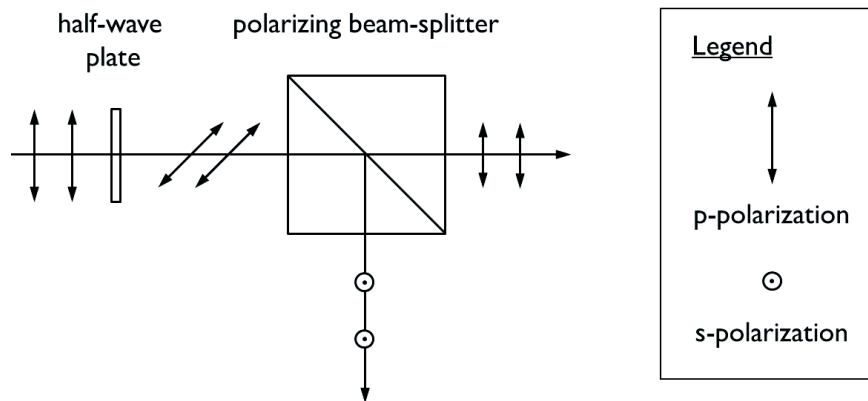

Figure 4.3: *Schematic drawing of a laser beam attenuation unit composed of a half-wave plate and a polarizing beam-splitter cube.*

Outside the laser box the UV laser passes through a Keplarian beam expander, composed of two confocal lenses (f_1 = 700 mm, f_2 = 150 mm), to magnify the beam diameter by a factor of 4.7. On the right table another unit of half-wave plate and beam-splitter are installed to be able to finely tune the UV laser power, independently of the initially chosen ratio of IR to UV. The transmitted beam continues towards the microscope, the reflected portion can be measured in a detector for online monitoring of the used laser power. Finally, at the end of the UV path a third lens is installed with a focal length of 1 m to focus the beam onto the photocathode.

The infrared laser beam also contains the attenuation unit of half-wave plate and beam-splitter, as well as a telescope, slightly hidden on the right optical table, and a focusing lens. For design reasons and path lengths, the optical delay line is included in the IR path. It is composed of a rail and a corner-cube, which is positioned on a movable unit. The advantage of the corner-cube compared to two separate mirrors is that entrance and exit beam are always parallel, facilitating alignment. When the corner-cube is moved upwards the IR path is shortened, thus the pulse arrives earlier at the sample compared to the probe pulse. This effectively increases the delay between pump and probe pulses.
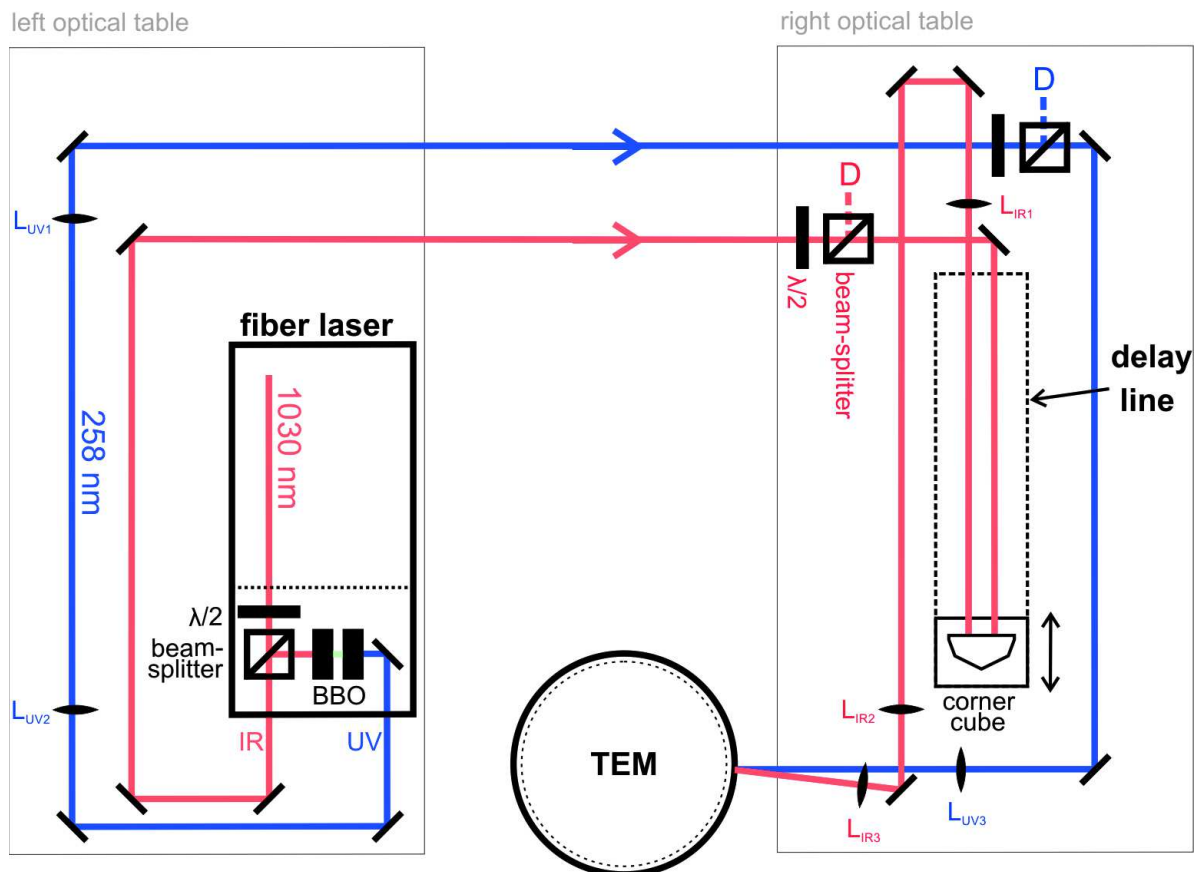
Figure 4.4: *Schematic drawing of the optical setup for stroboscopic UTEM in Strasbourg. Key components: laser system (fundamental wavelength 1030 nm) with beam splitter and 4th harmonic module using nonlinear BBO-crystals. Each beam path contains a combination of half-wave plate and beam-splitter for power attenuation, a Keplarian beam expander (L_1, L_2), and a focusing lens (L_3) before entering the TEM. The IR path contains an optical delay line with corner cube on a movable support.*

4.2   Finalization of the setup

All following data was taken at the UTEM in Strasbourg throughout my PhD project.

4.2.1   Resolution Tests with Photoelectrons

The spatial resolution was determined using a standard test sample of gold nanoparticles, the sample was not excited. A moderate UV laser power of 15 mW at 2 MHz repetition rate was used for the image shown in figure 4.5a. Atomic fringes are clearly visible throughout the nanoparticle. The fast Fourier transformation (FFT) clearly shows the [111] plane with a spacing of ~2.3 Å. Even the [002] spot of 2.0 Å is weakly present. It can be stated that phase contrast imaging is possible when the microscope is operated with multi-electron pulses, yielding lattice resolution.
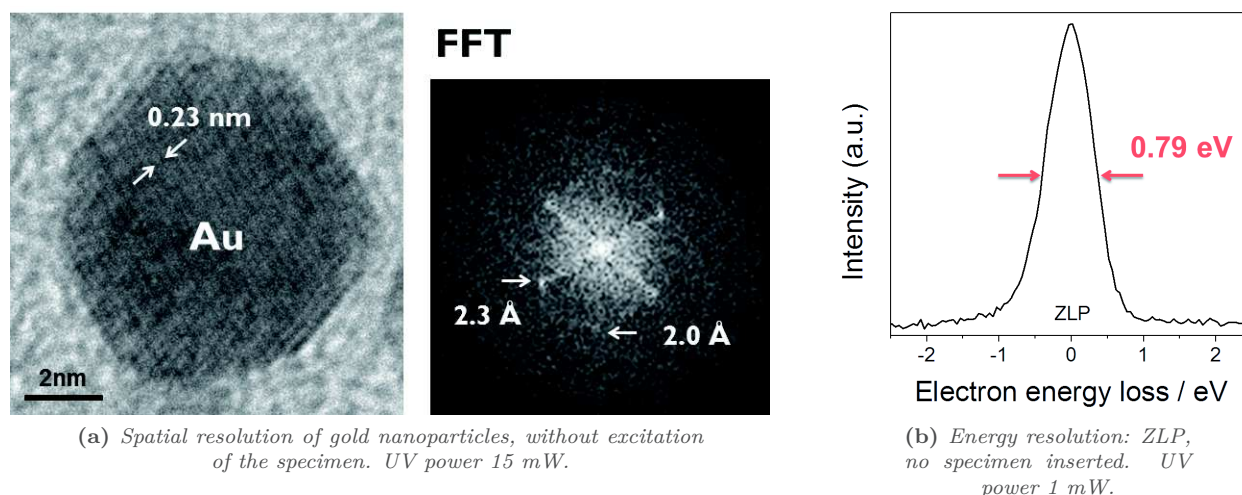
(a) *Spatial resolution of gold nanoparticles, without excitation of the specimen. UV power 15 mW.*

(b) *Energy resolution: ZLP, no specimen inserted. UV power 1 mW.*

Figure 4.5: *Resolution tests of the photoelectron beam in stroboscopic operation mode. The UV laser was operated at a repetition rate of 2 MHz.*

The energy distribution of the electron pulses was determined by electron energy loss spectroscopy (EELS) without any specimen. A lower laser power of 1 mW was used. Figure 4.5b shows the zero loss peak (ZLP) with a width at half maximum of 0.79 eV. This is very close to the theoretical limit of 0.7 eV, caused by the intrinsic kinetic energy distribution of the electrons generated at the cathode.

4.2.2   Synchronization of Pump and Probe pulses

For the synchronization of the pump and probe pulses, photon induced near-field electron microscopy (PINEM) was exploited. The test sample contains silver needles of a diameter between 150 and 300 nm, which were deposited on a copper TEM-grid, see figure 4.6. The high electron density makes silver an ideal sample, as the effect is very pronounced (collective oscillation of plasmons with the electron wave).
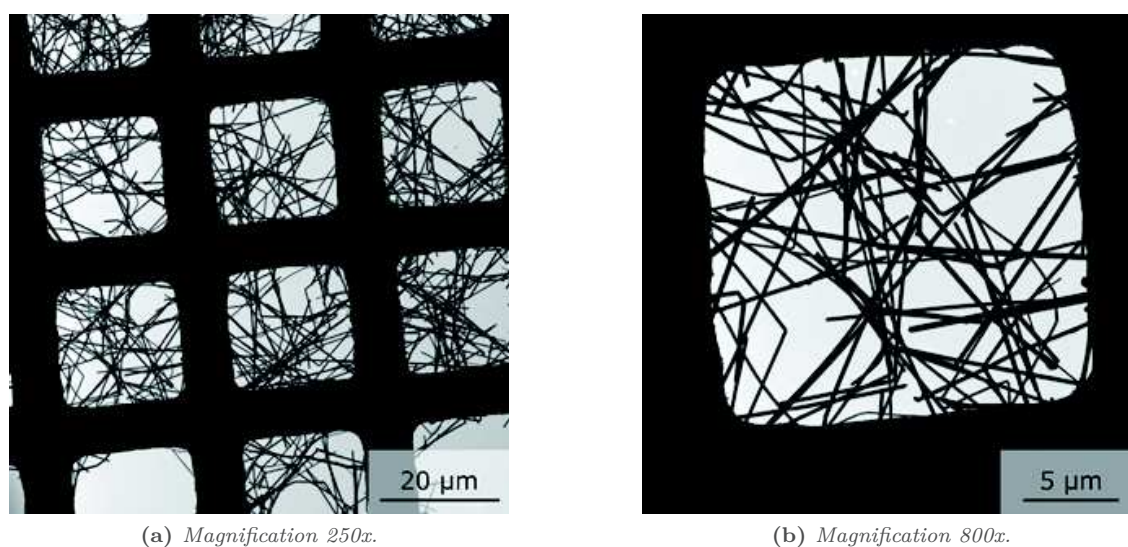

(a) *Magnification 250x.*

(b) *Magnification 800x.*

Figure 4.6: *TEM images of the PINEM test sample containing silver needles deposited on a copper grid.*

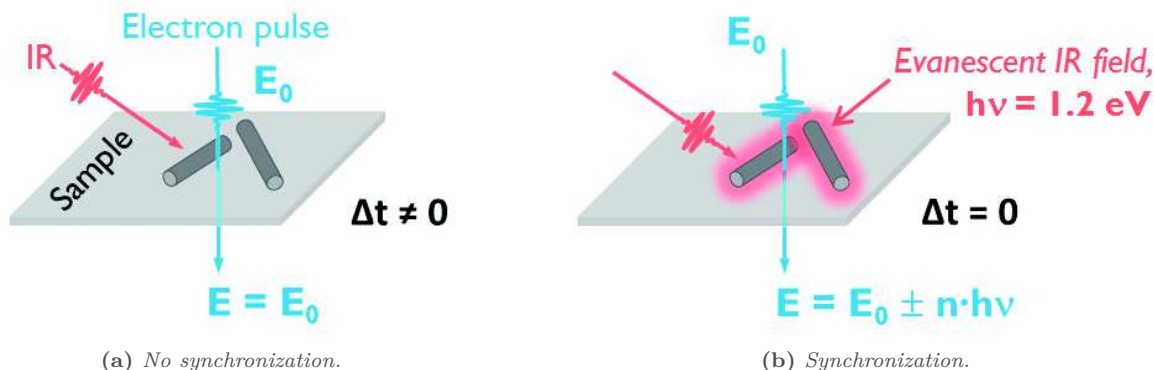Figure 4.7 shows a sketch of the different situations at the sample when the electron pulse passes through.

(a) *No synchronization.*

(b) *Synchronization.*

Figure 4.7: *Schematic of photon induced near-field electron microscopy (PINEM) on silver nanorods used to synchronize pump and probe pulses at the sample. The electrons can lose or gain entire quanta of photon energy while passing through the evanescent optical near-field.*

The sketch demonstrates the aloof spectroscopy with the electron pulse passing in close vicinity to a silver nanorod. Without synchronization (figure 4.7a) no interaction occurs and the electrons keep their initial energy E_0. As soon as pump and probe pulses are synchronized (figure 4.7b) the interaction with the evanescent near-field changes the energy distribution of the electron pulse. Electrons can gain or lose entire quanta of the photon energy $h\nu$.

This change of the electron energy upon synchronization was followed by electron energy loss spectroscopy (EELS). Figure 4.8 shows the relevant zero loss peak region.
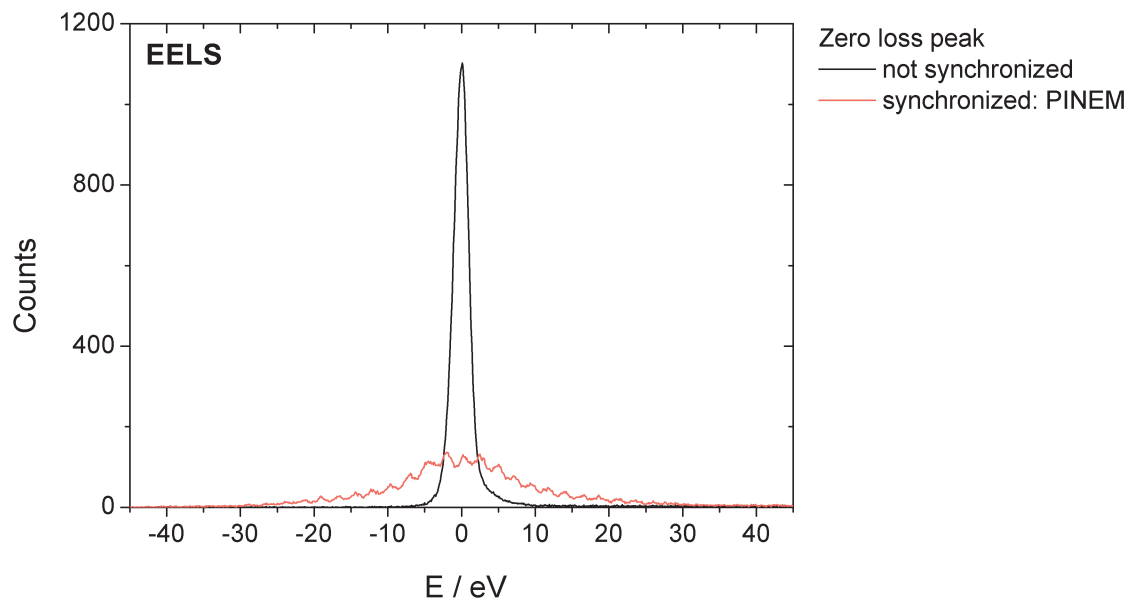

Figure 4.8: *Electron energy loss spectra of the zero loss region, with and without synchronization (PINEM). As sample silver needles were used.*

Obviously, the two curves are strikingly different. The black spectrum, without synchronization, shows one intense zero-loss peak 2.2 eV (FWHM). The red spectrum is located in the lower part of the plot. The intensity of the ZLP is greatly reduced, and more than eight side peaks can be distinguished on each side of

the central peak. The distance between these peaks is exactly one $h\nu$. Each peak corresponds to the uptake or loss of a certain number of photon energy. The area below both curves is equal, as the total number of electrons is constant.

The high resolution of the side peaks visible in figure 4.8 requires tedious work, for instance to select the optimum sample position and magnification, as well as matching pump and probe intensities in order to achieve a situation where almost every electron interacts with the optical near-field. To simply determine the synchronization of pump and probe, it is sufficient to look for a drop in intensity, coupled with a broadening of the ZLP. In fact, this will be used extensively throughout this chapter as an indirect tool to detect and measure the electron pulse.

4.3   Experimental Procedure

The electron microscope provides no direct way to observe and analyze the electron pulses. Photon induced near-field electron microscopy was once again used to gain indirect access to the electron pulses, in order to characterize them under various conditions. The same silver test sample was used.

The acquisition of EEL spectra at different temporal delays between pump and probe pulses traces the evolving overlap between optical near-field and electron pulse. Such a set of EEL spectra will be referred to as *PINEM scan*. High resolution of individual side peaks is not necessary, as described above.

In the following, the PINEM interaction is demonstrated using my own measurements. Three scenarios will be discussed, in order to explain the method of analysis used throughout this chapter.

4.3.1   Data Analysis

Figure 4.9 shows the first example. In the top part the PINEM scan is displayed as a 2D-chart, which allows an easy observation of the changing zero-loss peak while the delay was varied. Each horizontal line corresponds to an EEL spectrum, with its intensity displayed in false colors. The temporal delay of pump and probe (Δt) is changed on the y-axis. In the lower part of this figure the intensity of the zero-loss peak (ZLP) is shown as a function of the delay, which corresponds to a vertical section of the upper chart along $E = E_0$.

Such scans provide three important elements of information. First of all, the synchronization (t_0) of the photon and electron pulse at the sample is at the moment of biggest change of the ZLP. Second, the convolution Δ_0 of the electron pulse with the optical near-field can be extracted from the lower plot according to [68], see also section 3.2.2 on page 13. And of course, the energy distribution ΔE of the unperturbed electron pulse can be extracted from an EEL spectrum far away from synchronization.
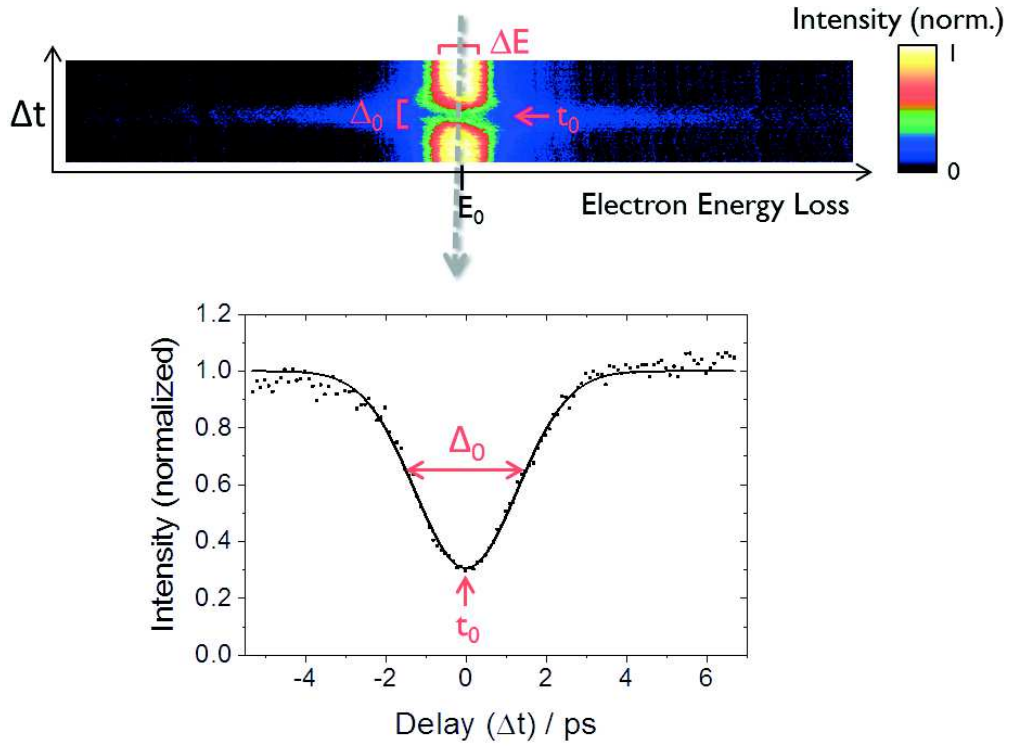
Figure 4.9: *Example of a PINEM scan. Upper part: At various delay between pump and probe (Δt) EEL spectra are taken. Each horizontal line corresponds to an EEL spectrum, the intensity is normalized and displayed in false colors. Important variables extractable: energy distribution of the ZLP (ΔE), temporal convolution of optical near-field and electron pulse (Δ_0) and the synchronization (t_0). Lower part: Vertical section of the PINEM scan at $E = E_0$, giving the intensity profile of the ZPL as a function of Δt.*

With equation 3.1 the electron pulse duration can be estimated. The life time of the optical near-field is short compared to the laser pulse length (around 10 fs [68] *vs.* 370 fs). Thus, we can write:

$$\Delta_0 \approx \sqrt{\Delta t_e^2 + \Delta t_p^2}$$
$$\Delta t_e \approx \sqrt{\Delta_0^2 - \Delta t_p^2}$$

with Δ_0: FWHM of cross-section, Δt_e: electron pulse duration,
Δt_p: photon pulse duration.

In this example Δ_0 is 3 ps. Resolving the equation with $\Delta t_p = 370$ fs yields a Δt_e of 2.98 ps, which is very close to Δ_0. Consequently, the photon field duration is negligible in this example. For longer electron pulses the photon field duration further loses importance. Throughout this thesis, the shortest electron pulses measured are in the order of 2 ps. Thus, it can be generalized that

$$\Delta t_e \approx \Delta_0 \ . \tag{4.1}$$

However, this analytical method attains its limitations as soon as the zero-loss peak is broader. Figure 4.10 shows the effect of the optical near-field on a peak of 7.5 eV (FWHM). The stacked and normalized spectra were taken with increasing delay between pump and probe pulses from the bottom of the graph to the top. At t_0 the zero-loss peak shows a little dip. Before and after t_0 only the shape of the peak edges is changed.
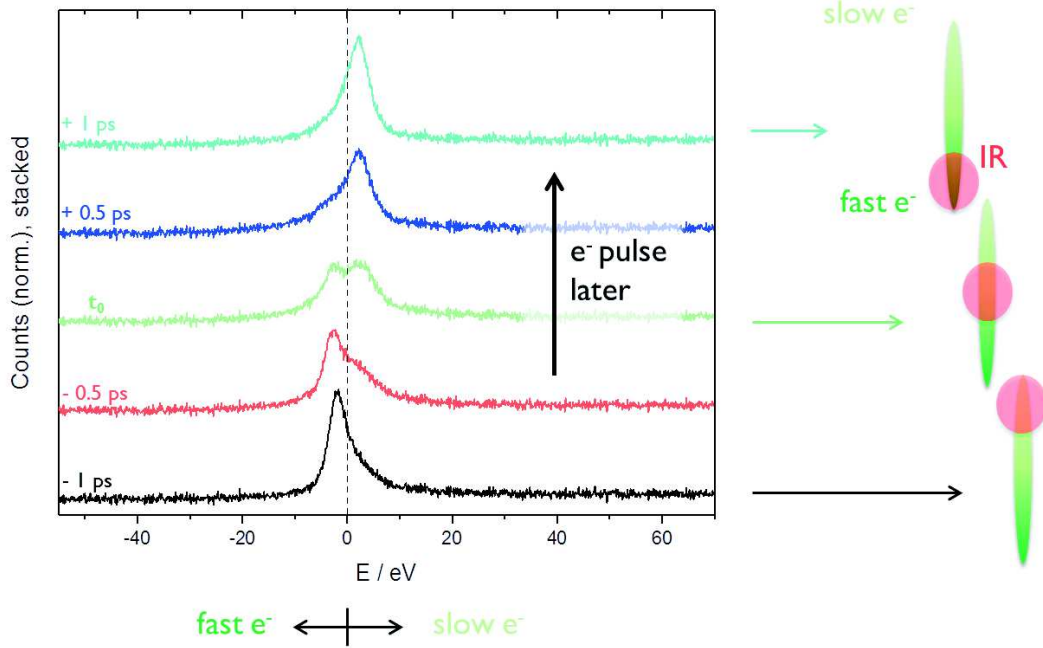
Figure 4.10: *Example of EEL spectra from a PINEM scan with medium ΔE. At different pump-probe delay the optical near-field causes a diminution of only distinct parts of the ZLP, visible as a change in the shape of the peak. It provokes a shallow tail on one side of the peak, or a dip in the center of the ZLP upon synchronization.*

If the electron pulse duration is longer than the presence of the optical near-field, only a fraction of the electron pulse interacts with the latter. A temporally long electron pulse is equivalent with a longitudinally elongated electron pulse. Interaction scenarios with the optical near-field are shown in the schematic on the right hand side of the graph. Snapshots are sketched, which cover the short moment when the photon field is present and the interaction occurs. By varying the delay between electron and photon pulse, different slices of the elongated electron pulse interact with the photon field. Assuming that fast electrons have a higher energy (speed) than slow ones, the electron pulse must comprise an energy dispersion from high energy electrons at the front and slow electrons forming the tail (represented with dark to light green color). At $t_0 - 1$ ps (black curve at the bottom of the graph), the electron pulse arrives earlier than the photon pulse. Hence, the upper end of the electron pulse composed of slow, low-energy electrons overlaps with the optical field. In the EEL spectrum slow electrons that further lost quanta of $h\nu$ provoke the tail on the right hand side of the zero-loss peak. Those who gained energy sum up with the fast electrons which passed the sample before the near-field occurred, which gives the steep edge on the left side of the peak. The inverse happens when the fast electrons overlap with the optical field ($t_0 + 1$ ps, petrol-colored curve at the top of the graph). When the middle slice of the electron pulse interacts with the near-field (green curve) a dip is created at $E = 0$ eV, as electrons which gained or lost energy are shifted outwards in the spectrum.

For electron pulses having an even higher energy distribution, an example of the PINEM interaction is given in figure 4.11. Here ΔE is 220 eV large, which can be achieved by the use of high laser power and low Wehnelt bias voltage. The curve at the bottom of the graph presents the energy distribution without interaction. It shows a sightly inclined plateau with two peaks at lowest and highest electron energy. Again, the stacked spectra are taken with increasing pump-probe delay. The interaction zone (shown in red) moves through the spectra towards higher electron energy upon increasing delay. A depletion is visible in the energy range where electrons interact with the near-field. Furthermore, two peaks on either side arise, caused by those

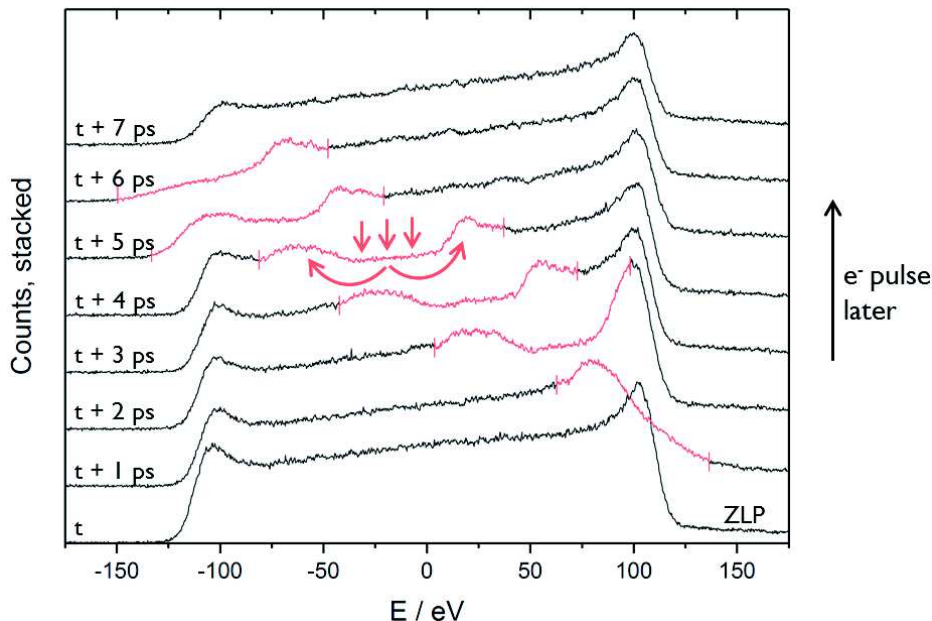electrons summing up with higher or lower energy neighbors (see red arrows).

Figure 4.11: *Example of EEL spectra from a PINEM scan with high ΔE. The interaction zone (red) propagates through the ZLP with changed pump-probe delay. This shows as shallow tales on either side of the zero loss peak or for inner slices as a dip with two two neighboring peaks caused by the electrons which lost or gained energy (indicated by red arrows).*

A temporal profile of the ZLP intensity at $E = E_0$ can not represent the whole interaction of the broad electron pulse with the optical near-field. The convolution according to equation 4.1 would yield a false electron pulse duration, far below the actual value.

In summary, the change in EEL spectra due to an interaction with the optical near-field appears very differently depending on the initial shape of the ZLP (Gaussian shape with reduced intensity upon PINEM, Gaussian shape with changing edges, or broad flat-top distribution with a propagating dip). Throughout the following studies, pulses of these diverse shapes have to be compared. Therefore, no standardized, numerical method can be applied to determine the convolution of electron and photon field and thereby the electron pulse length. All PINEM scans were analyzed manually, the beginning and end of the interaction were noted and the electron pulse duration was calculated. This guarantees comparable results for qualitative considerations whatever the pulse energy width.

4.3.2   Conversion of the Wehnelt Bias

The Wehnelt setup contains one resistor of 4800 MΩ behind the emitter, resulting in a current of 42 µA at 200 kV acceleration voltage. This current passes through the bias resistors. In photoelectron mode the self-biasing loop is not effective as the emission current is too low. This simplifies the situation and leaves three resistors, see figure 4.12. One is fixed at 2 MΩ, two others are variable up to 20 MΩ and 5 MΩ, corresponding to the regulations named *coarse* and *fine* respectively. This results in a minimum bias of 83 V (2 MΩ) and a maximum bias of 1125 V (27 MΩ). The minimum represents quasi zero effect on the emission, no gun gross-over is produced. At the maximum value the emission is fully extinct. This range gives full flexibility to the operator, knowing that the Wehnelt bias is a parameter which changes numerous

characteristics of the electron beam (emission area, gun cross-over, convergence angle, etc.). Evidently, a pronounced effect on the electron pulse characteristics is expected.
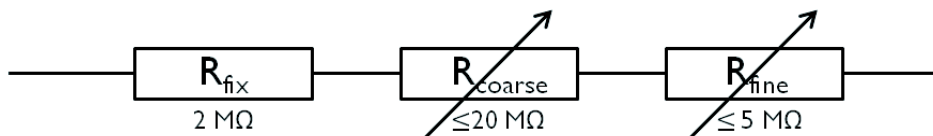

Figure 4.12: *Schematic drawing of the series of bias resistors.*

The software displays only a rough bias setting at a scale of 1 to 9 for each variable resistor, with 1 being the maximum resistance and 9 being none. Furthermore, 4 steps lay between each number, which are not monitored by the software. In order to convert the bias setting to a specific voltage, the following procedure has been developed: The bias is noted in steps of 0.25, with the lowest being 1 and the highest being 9.75. This way the integer part corresponds to the number displayed by the software. This setting number will be converted into a percentage of the maximum resistance, as demonstrated in figure 4.13.
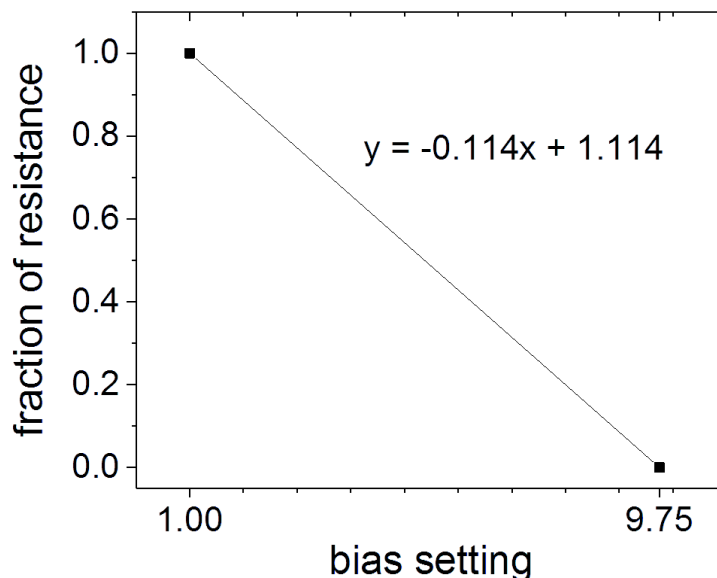

Figure 4.13: *Conversion of the bias setting to a percentage of the resistance.*

In approximation, the conversion of the bias setting to a fraction of the resistance is $y = -0.1x + 1$. The total bias voltage can be calculated as follows:

$$
\begin{aligned}
R_{Bias} &= R_{fix} + R_{coarse} + R_{fine} \\
R_{Bias} &= 2 \text{ M}\Omega + coarse \cdot 20 \text{ M}\Omega + fine \cdot 5 \text{ M}\Omega \\
\boldsymbol{U_{Bias}} &= [2 \text{ M}\Omega + (-0.1 \cdot coarse \ setting + 1) \cdot 20 \text{ M}\Omega + (-0.1 \cdot fine \ setting + 1) \cdot 5 \text{ M}\Omega] \cdot 42 \text{ μA}
\end{aligned}
$$

with R: resistance and U: voltage.

This conversion contains a round-off error resulting a minimum bias voltage of 109 V (instead of 83 V) and a maximum of 1030 V (instead of 1125 V). It has to be noted that the resistors are motorized in the high-tension tank and posses a *hysteresis*. This means that one step up and one step down does not result

in the same bias value. This is evident from the emission pattern. Consequently, the round-off error can be neglected.

To minimize the hysteresis error, all experiments were started at minimum bias voltage. The resistance was progressively increased to the desired values but never decreased within a series of measures.

4.4   Study of Electron Pulse Dynamics

Every electron pulse is characterized by its temporal pulse length, the energy distribution and the number of electrons contained in one pulse. In ultrafast TEM these characteristics translate in temporal resolution, spatial and energy resolution, as well as signal intensity.

All accessible instrumental parameters were tested systematically to study their influence on the pulse characteristics. Specifically, the UV laser power was studied (which drives the number of electrons per pulse), the photocathode shape and position inside the Wehnelt cone (the gap between cathode and Wehnelt aperture; both parameters change the emission pattern), the bias voltage applied on the Wehnelt electrode and all electromagnetic lens currents (each defining cross-overs throughout the column).

The electrostatic Wehnelt electrode has multiple influences on the electron beam. The applied bias voltage defines the emission area on the cathode, the extraction field and electrostatic potential, the size of the gun cross-over and its position within the acceleration path (propagation speed of electrons). These drive Coulomb interactions such as space charge or Boersch effect and the interaction time. Furthermore, the Wehnelt bias controls the photoelectron current by the amount of electrons leaving the Wehnelt cone.

4.4.1   The UV Laser Power

The first component investigated is the UV laser. Its pulse energy defines the number of photoemitted electrons per laser pulse and thus the number of electrons contained in each electron packet. In a first experiment the current on the viewing screen was measured as a function of the UV laser power. This current scales linearly with the number of electrons hitting the screen. Series were taken at different Wehnelt bias setting (color-coded), all other parameters were kept constant. The result is shown in figure 4.14, lines are drawn between the data points as guide to the eye.

The graph shows an increasing current with increasing laser power. This trend is valid for all Wehnelt bias settings, being more pronounced at low bias voltage. As expected, the current on the viewing screen and thus the number of electrons per pulse is increased with increasing laser power.
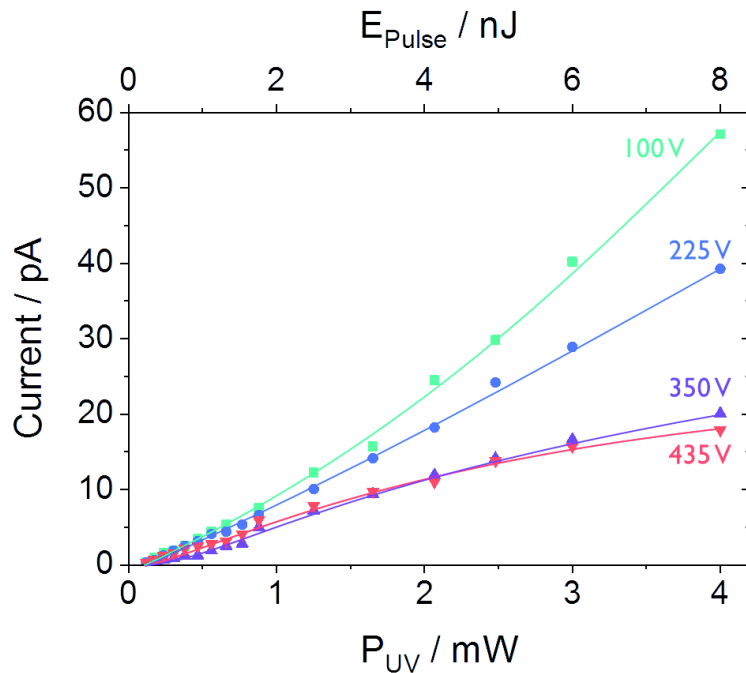
Figure 4.14: *Evolution of the averaged electron beam current measured on the viewing screen as a function of the UV laser power. Series were measured at different Wehnelt bias settings, displayed in color code. As guide to the eye curves were drawn, connecting the data points. A a Ta disc at 760 μm distance of the Wehnelt aperture was used. The laser operated at 500 kHz. The corresponding pulse energy is displayed on the upper axis.*

Subsequently, PINEM scans were carried out at different UV laser power in order to study the impact of the different number of electrons per pulse on the resulting energy distribution ΔE and the pulse length Δt_e. Again, series have been taken at different Wehnelt bias settings, all other parameters were kept constant.

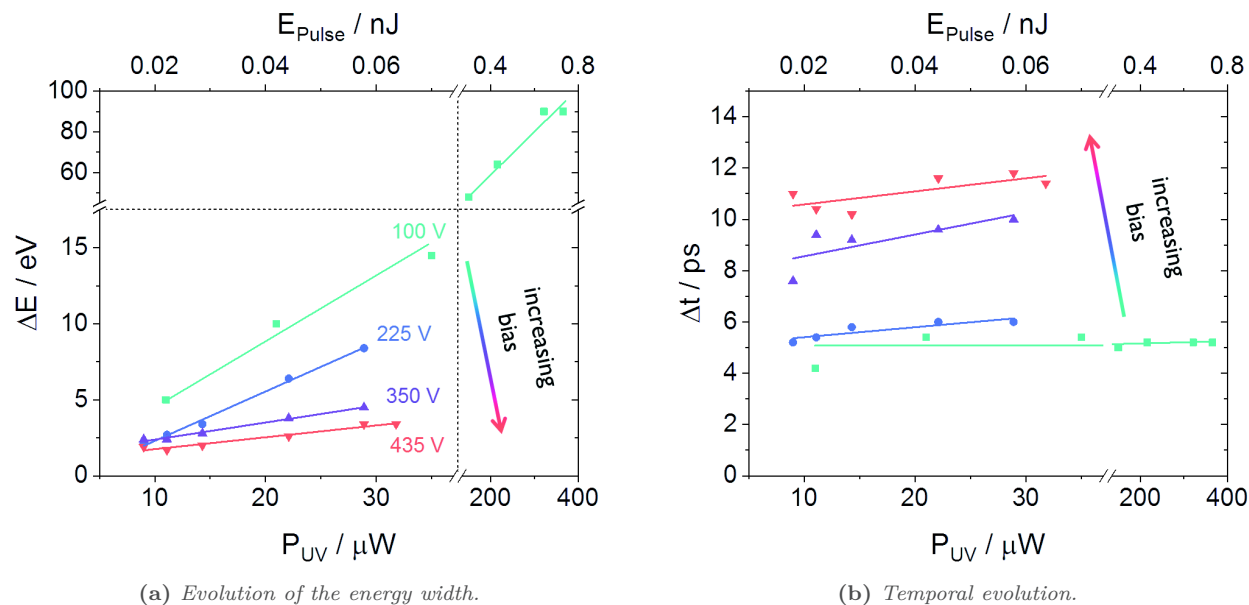**(a)** *Evolution of the energy width.*

(b) *Temporal evolution.*

Figure 4.15: *Influence of the UV laser power on the resulting electron pulse characteristics. Series were measured at different Wehnelt bias settings, noted in color code. A a Ta disc at 760 μm distance of the Wehnelt aperture was used. The laser operated at 500 kHz.*

The energy distribution increases linearly with increasing laser power, which corresponds to an increasing number of electrons per pulse as observed just before. The slope varies with the applied Wehnelt bias again being more pronounced for low Wehnelt bias. The temporal length of the electron pulse appears to increase very modestly with the laser power. All trends are consistent whatever bias voltage is applied.

4.4.2 The Wehnelt Bias

In this section, the influence of the Wehnelt bias voltage on the electron pulse characteristics will be presented.

Temporal Resolution

The temporal evolution of the electron pulse over the complete range of Wehnelt bias is shown in figure 4.16. The blue triangle represent data taken with a truncated tip, the green dots represent a disc-shaped cathode. The big Wehnelt-cathode gap of 760 µm is illustrated with dark colors and a solid line (guide to the eye), the short gap of 550 µm is visualize by light color and the dashed lines.
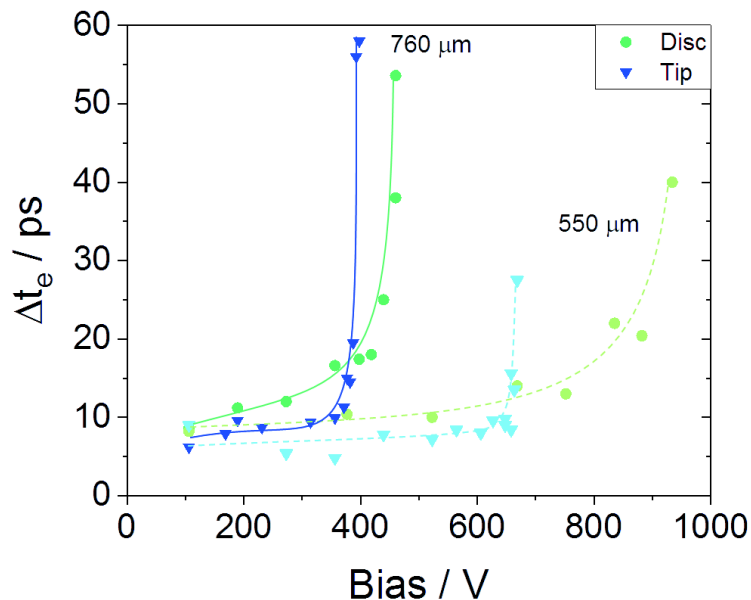

Figure 4.16: *Evolution of the electron pulse length as a function of the Wehnelt bias, measured for two different cathode-Wehnelt gaps and emitter shapes. Truncated tip in dark and light blue triangles, disc in green dots. Dark color and solid lines represent a distance of 760 µm, light color and dashed line 550 µm. Each curve shows two regimes. At first Δt_e increases gently, after a threshold bias the pulse length strives towards infinity.*

In each curve two regimes are clearly visible. The first one shows a very gentle increase. After a threshold value the temporal length strives towards infinity. This behavior is similar for all cathode shapes and positions.

Further statements can be made. First, for a shorter gap the threshold is shifted to higher bias values. Also, the bias range is larger, which allows electrons to reach the detector.
Second, the change from one regime to the other is abrupt for the truncated tip and more gradually for the disc-shaped emitter. This suggests an important role of the shape and emission area inside the field lines of the Wehnelt electrode.

The existence of two regimes in the evolution of the temporal pulse length does not concur with an explanation purely based on Coulomb interactions. The Wehnelt bias brings along other effects which have to be considered.

Emission Characteristics

The shape of the electron emission pattern depends strongly on the applied Wehnelt bias. This can be observed by focusing the electron beam with the condenser lens (CL3) onto the sample level without any specimen inserted, which means projecting and magnifying the gun cross-over ("virtual cathode") onto the detector. The evolution of the emission pattern with increasing Wehnelt bias is shown in figure 4.17 for both cathode shapes.
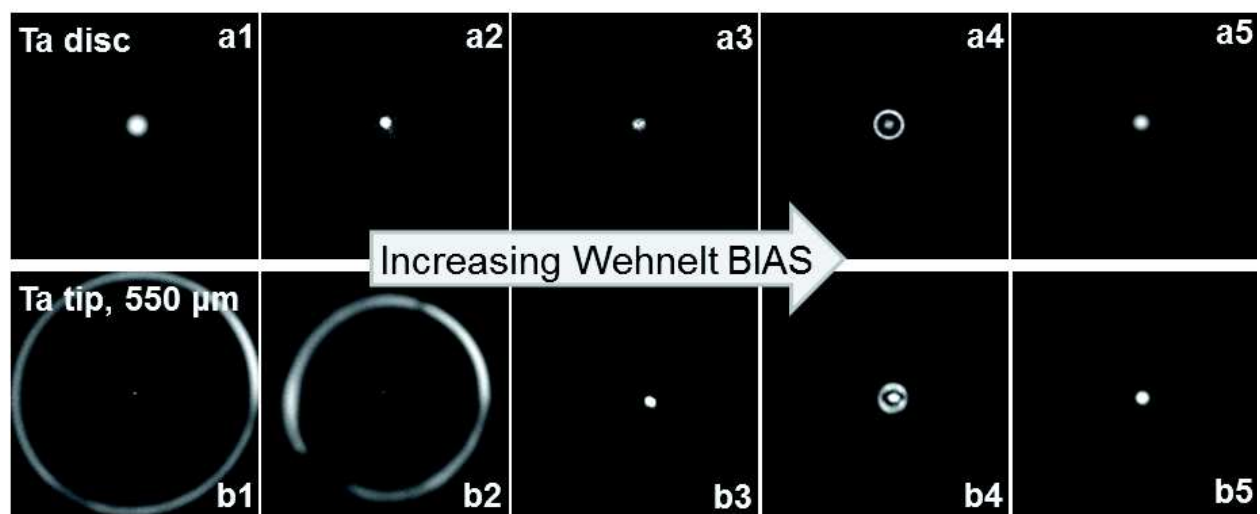

Figure 4.17: *Evolution of the photoelectron emission patterns with increasing Wehnelt bias. The focal plane of the electron beam is projected on the detector. In (a) the emission of the tantalum disc at 550 µm is shown here, the evolution is similar for other distances or tip-shaped emitters at 550 µm. In (b) the emission of the truncated tantalum tip at 550 µm is presented.*

The emission from the tantalum disc is shown in the upper row. A bright, big spot is observed at minimum bias (a1), which progressively shrinks and loses intensity when the bias is increased (a2-a3). At a certain threshold a small halo appears (a4) which shrinks and merges with the central emission spot upon further increased bias (a5). The united emission spot is particularly bright but extinguishes rapidly when the bias is increased even further. This evolution is qualitatively the same for any disc-Wehnelt gap, as well as for the truncated tip at large distance. Only the exact bias values to achieve the individual patterns vary with the distance of the cathode to the Wehnelt aperture.

The tip-shaped emitter at a short distance from the Wehnelt aperture shows an exceptional emission pattern, which is displayed in the lower row of figure 4.17. A large ring-shaped emission is present around the central spot at low Wehnelt bias (b1). This ring shrinks at higher bias until it merges with the central emission (b3), right before the small halo appears (b4) and merges (b5) as described above.

The presented patterns were acquired with photoelectrons. Theoretically, they are equivalent in thermionic emission, except that working at low bias is not possible as electric arc discharges occur and the high tension would shut down.

These evolutions were discussed for conventional electron microscopy more than sixty years ago, when the thermionic electron gun was developed. [76] It is based on detailed considerations of the inhomogeneous electric field inside the Wehnelt cone. Since then, standard working conditions were established at fairly high Wehnelt bias where the small halo has merged with the central emission, the so-called "saturated beam". It is known that the small halo is formed by off-axis electrons emitted from the flat cathode surface with a high angle to the optical axis. The "hollow-beam" is formed due to the spherical aberrations of the electrostatic Wehnelt lens. A high bias is capable to focus these off-axis halo-electrons through the apertures inside the microscope in order for them to reach the sample.

The big ring emitted by the tip-shaped cathode can be attributed to shank emission from the side-walls of the filament. All contributions are schematically summarized in figure 4.18. The origin of the ring-shaped shank emission zone also lies in the electric field distribution. Above the emission zone the electrostatic potential is too high for electrons to leave the bulk material or they are directly rejected back to the surface. Below the emission zone, the electric field is too weak to focus the electrons out of the Wehnelt cone. With increasing bias the emission zone shifts down along the tip, until it reaches the height of the flattened area where no separate shank emission is possible any more. This corresponds to figure 4.17-b3. Apparently, an even higher bias is required to focus off-axis electrons emitted from the flattened area down along the microscope.
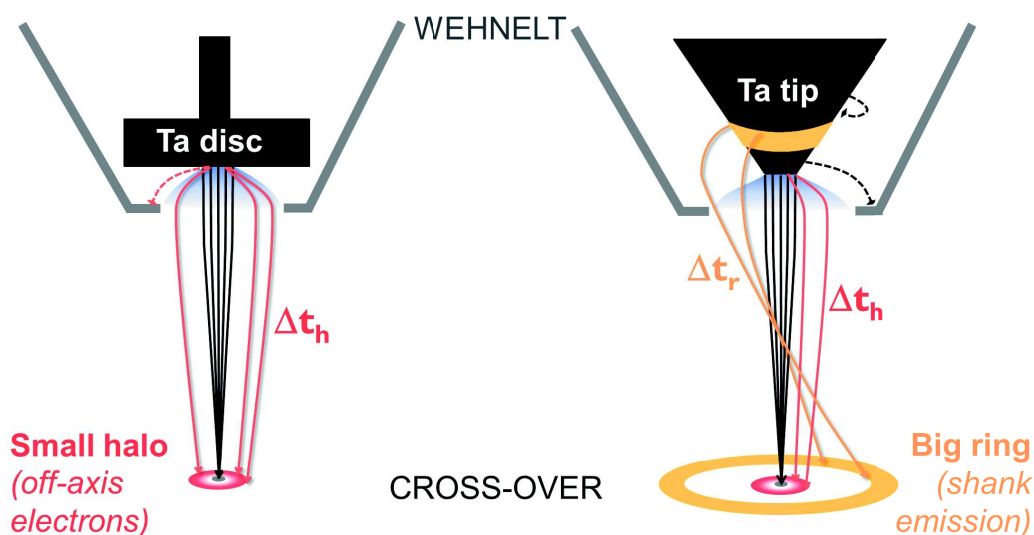

Figure 4.18: *Schematic drawing of the two emitter shapes and their electron emission. The projection in the focal plane of the gun cross-over represents the virtual cathode. The disc shows two electron populations being central emission parallel to the optical axis and emission in a high angle, the off-axis emission forms a small halo in the focal plane. The conical emitter shows additional shank-emission form the side walls which produces a big ring in the emission pattern.*

The emission pattern demonstrate that the spherical aberration of the Wehnelt electrode discriminates the emitted electrons into populations which travel distinct paths and possess different convergence angles. The temporal component of the UTEM allows to study individual areas of the emission pattern in detail, especially with respect to the arrival time at the sample.

Arrival Times

At first, the arrival time of the central emission spot is studied as a function of the Wehnelt bias. All other contributions have been sheltered by apertures. The result is presented in figure 4.19. The measurements are calibrated for each emitter shape and cathode-Wehnelt gap with zero shift for minimum bias. All curves show a nonlinear shift of t_0 with increasing bias voltage. The electron pulses are progressively retarded. The shape of the curve is slightly different depending on the emitter shape.
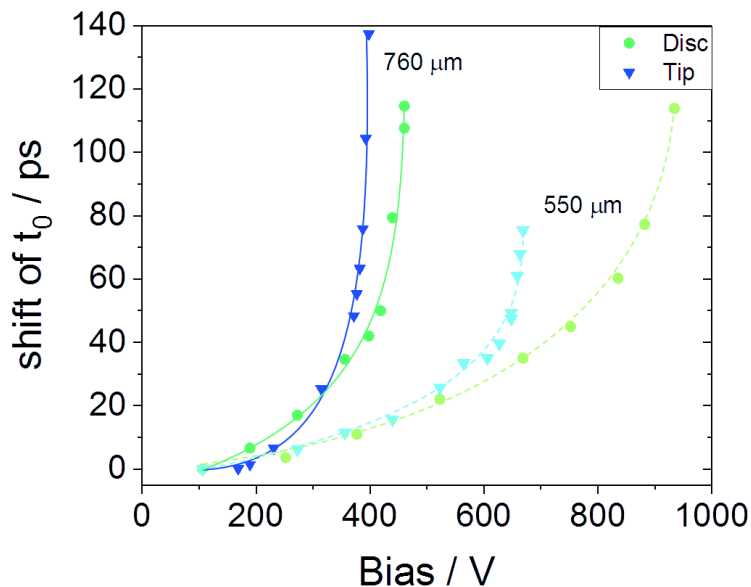

Figure 4.19: *Evolution of the arrival time t_0 of the electron pulse as a function of the Wehnelt bias for different cathode-Wehnelt gaps and emitter shapes. Only the central emission is considered. Truncated tip in dark and light blue triangles, disc in green dots. Solid line shows a distance of 760 μm, dashed line 550 μm.*

With increasing bias voltage the electrons experience a weaker extraction field on the cathode surface, as well as a higher potential barrier while exiting the Wehnelt cone. These two effects sum up and retard the electrons. At the bigger cathode-Wehnelt gap the electrons have to overcome a longer distance inside the cone and are thus stronger affected by the electrostatic potential. This explains the pronounced retarding effect and the shorter bias range in which electrons are able to leave the Wehnelt cone and reach the detector.

The disc-shaped emitter shows a smoother rise than the truncated tip. The same behavior was observed for the electron pulse length. This could be attributed to the large emission area of the disc compared to the small flattened area of the truncated tip.

In a second experiment, different zones in the emission pattern of a truncated tip were analyzed separately. Herefore, the electron beam was focused onto the sample and the specific region was positioned above the entrance of the spectrometer. Figure 4.20a shows data from the tip at a small cathode-Wehnelt gap. The blue triangles represent the central emission whereas the yellow rings correspond to the shank emission. A schematic sketch above the graph visualizes the emission pattern corresponding to the different bias values. The small halo was investigated at higher cathode-Wehnelt gap, in order to exclude shank emission. The result is shown in figure 4.20b. Again, the central emission is represented by blue triangles, the halo is depicted with small red circles. In these graphs the error bar is used in an unusual way indicating the temporal length of the individual electron population.
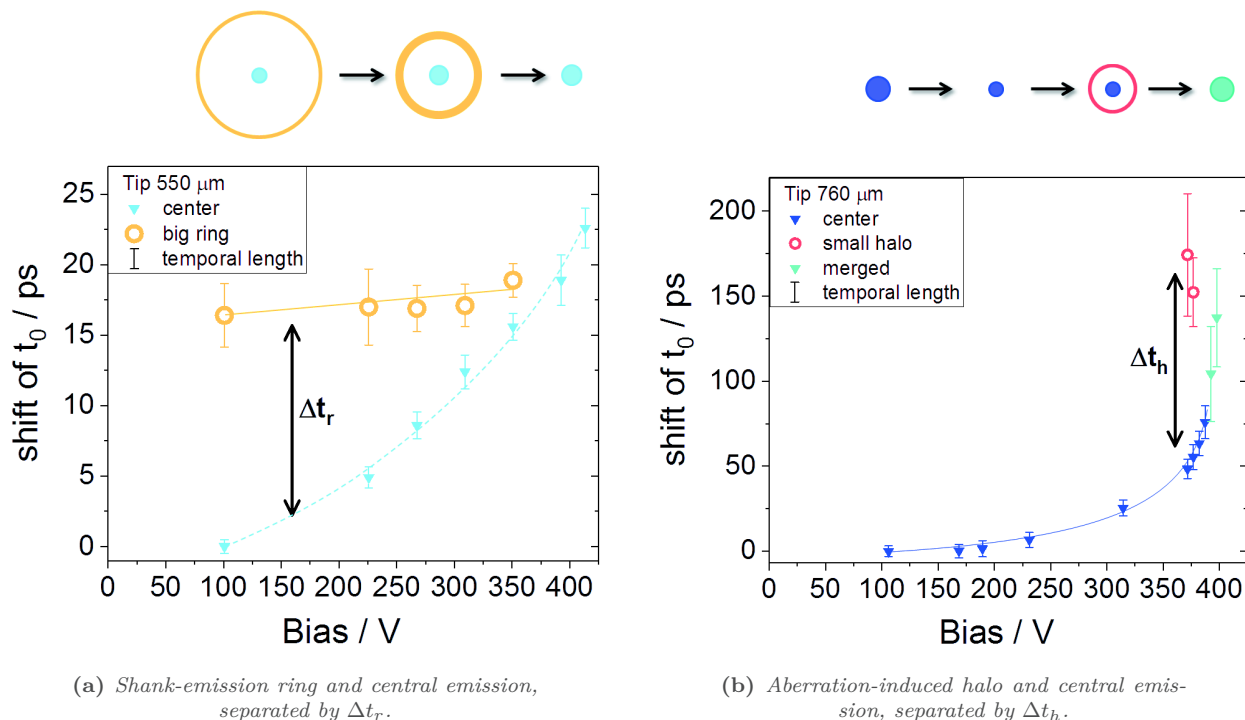
(a) *Shank-emission ring and central emission, separated by Δt_r.*

(b) *Aberration-induced halo and central emission, separated by Δt_h.*

Figure 4.20: *Shift of the arrival time t_0 measured separately for the different electron populations. The error bar is used in an unusual way here, indicating the temporal length of the electron population. Note the different scales on the ordinate.*

The graphs show a strikingly different behavior for the individual electron populations. As before, the central emission shifts smoothly with increasing bias. The shank emission in figure 4.20a does not seem to be strongly influenced by the bias. The arrival time stays almost constant, but is retarded with respect to the central emission at the same Wehnelt bias voltage. At minimum bias the shank emission arrives 17 ps after the central spot.

The small halo (figure 4.20b) only appears in a short bias range; two measurements could be carried out before it merged with the central emission (represented as petrol colored triangles). The halo appears at a bias of 370 V where it is delayed by 120 ps with respect to the central emission. This huge time difference (Δt_h) decreases rapidly and converges with the shift of the central emission. The central spot itself reaches a pronounced shift when the halo is incorporated. Regarding the temporal length which is indicated by the error bars, the central emission shows short Δt_e until the merging of the halo where it increases drastically. The halo, on the other hand, shows a huge temporal length of 70 ps when it first appears, decreasing rapidly to 40 ps before the halo merges with the central emission spot. The length of the merged electron pulse is about the sum of the individual populations right before merging (40 ps + 20 ps = 60 ps).

The observation that areas of the emission pattern show distinct arrival times clearly states a co-existence of individual electron populations caused by different emission angles and trajectories.

A closer look at the shank emission rises the question why the arrival time stays almost constant. The retarding effect of the Wehnelt potential should be in the same order of magnitude as for the central emission. This suggests a second contribution with the opposite trend, which could be the path length. Shank emission happens above the flattened surface of the cathode, so the electrons need to cover a longer distance until they reach the Wehnelt aperture compared to the central emission. Furthermore, as these electrons are emitted far from the optical axis, their path comprises deviations from the optical axis as the electrons go

through several cross-overs on their way to the detector. With increasing bias the shank emission zone shifts down along the tip reducing the additional path length inside the Wehnelt. Their emission is also closer to the optical axis. Plus, the higher focusing strength of the Wehnelt electrode produces an electron beam, which converges close to the optical axis, further reducing the additional path length. (Ray path simulations showing the convergence of the electron beam at different Wehnelt bias can be found in the appendix B on page 104.) In summary, an increasing Wehnelt bias reduces the additional path length of the shank emission with respect to the central emission. Combined with the retarding effect, the arrival time of the shank emission stays almost constant.

The off-axis halo-electrons must encounter a huge potential barrier when the bias is just strong enough to focus them out of the Wehnelt cone. Their trajectory takes them extremely close to the circumference of the Wehnelt aperture (at slightly lower bias voltage the electrons would crush on the inside of the Wehnelt). In addition to the potential barrier, also the trajectory down the microscope comprises strong deviation around the optical axis, all adding up to the large shift above one hundred picoseconds. With increasing bias the off-axis electrons quickly converge with those directly emitted on-axis. This explains why the delay between central spot and halo (Δt_h) decreases rapidly, and the arrival times and emission patterns merge shortly thereafter.

Qualitatively, this trend is valid for any off-axis halo-electron population, no matter the Wehnelt gap or emitter shape.

The co-existence of the two electron populations could be proved in one single PINEM scan, shown in figure 4.21a. In contrast to previous measurements, the beam was not focused onto the sample but slightly spread by the lens current of the condenser lens in order to mix the electron populations. In the long PINEM scan over 250 ps two areas can be identified where the zero-loss peak is broadened (indicated with arrows). A cross-section of the side-band region ($E = 13$ eV $\pm\, 3.5$ eV, white shaded area) nicely shows the broadening as a signal increase. This spectrum is superimposed in white on the left-hand side of the plot.

In figure 4.21b such cross-sections of the side-band region are displayed for a set of long PINEM scans. The values of the Wehnelt bias were finely tuned around the co-existence of both populations. The corresponding emission patterns (taken with focused electron beam) are shown right next to each spectrum. As calibration the arrival time at minimum bias is set to zero, every spectrum is normalized.

The bottom spectrum at minimum bias shows one single peak of the central on-axis emitted electrons. With increasing Wehnelt bias this peak is shifted to later arrival time, at the same time it broadens progressively. At a bias of 655 V the spectrum shows a second peak arriving 75 ps later. The following spectrum at 660 V again shows two peaks, which are closer together. The first peak follows the trend described for the on-axis electrons and is retarded, whereas the second peak arrives earlier than at lower bias. The top spectrum at 675 V shows one broad peak at intermediate arrival time. The corresponding emission pattern shows that the electron populations start to merge.
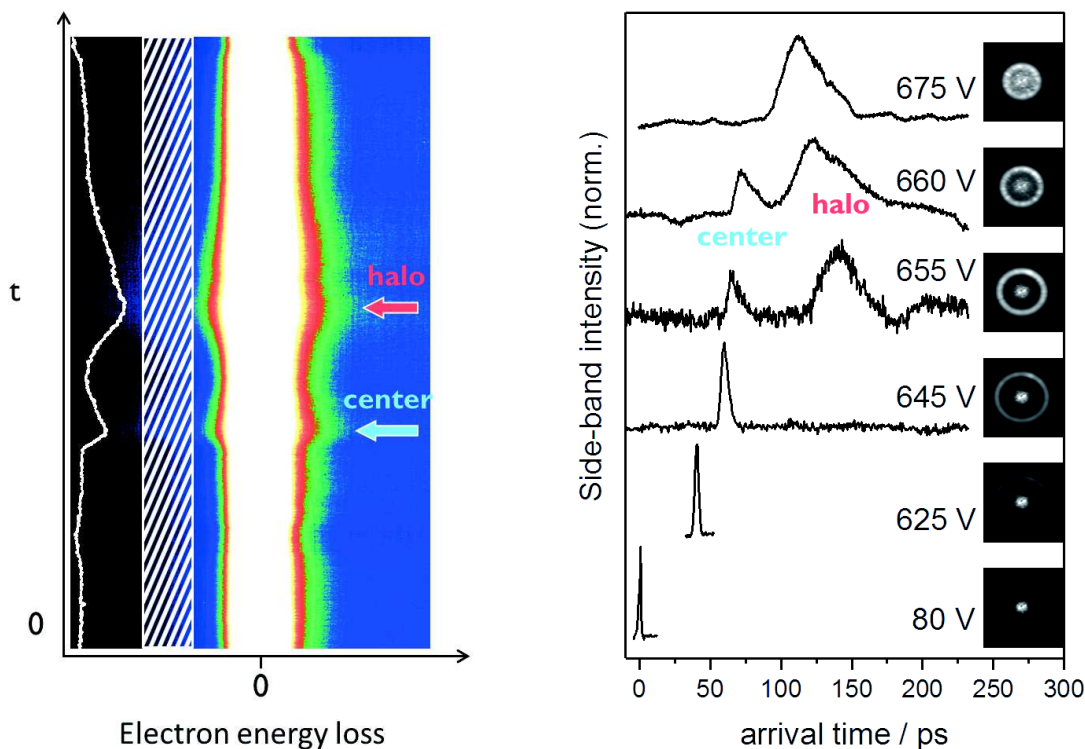
(a) *PINEM scan at a Wehnelt bias of 660 V. FWHM of the ZLP is 2.7 eV.*

(b) *Intensity profiles of side-band region as a function of the arrival time for different bias settings. Corresponding emission profiles on the right.*

Figure 4.21: *PINEM experiments showing the co-existence of two electron populations with different arrival times. A cross-section of the side-band region at $E = 13$ $eV \pm 3.5$ eV is extracted (white shaded area in a). This intensity profile better visualizes the PINEM interactions as distinct peaks - inset in a: white curve on black background In b: stacked and normalized intensity profiles from PINEM scans with different Wehnelt bias. Temporal shift and broadening of the peaks can be seen for the central beam and off-axis halo separately (left and right peak respectively).*

These measurements unambiguously prove the co-existence of two separate electron populations, which can be attributed to on-axis (central spot) and off-axis emission (halo). It should be mentioned, that just upon the appearance of the halo at 625 V, its portion on the total emission is so low that no second peak can be observed. Only in a short bias range when both populations exist to equal extent two separate peaks are visible. As soon as the halo merges with the central emission spot, one joint broad peak at intermediate arrival time is measured. This concurs with the arrival time measurements presented in figure 4.20b, except that here one single measurement captured both populations.

Temporal Resolution - Summary

With this completed picture, the temporal behavior of the electron pulse can be explained. The first regime of moderate pulse elongation comprises exclusively central on-axis emission. After a certain threshold value of the applied Wehnelt bias, off-axis electrons are focused out of the Wehnelt cone and down onto the sample. These electrons are drastically retarded with respect to the central emission due to an increased potential barrier close to the Wehnelt edge and especially due the longer trajectories. Merging both populations results in a huge temporal elongation of the resulting electron pulse in the second high-bias regime.

Energy Resolution

Besides the temporal resolution, the potential application of an ultrafast electron microscope also depends on the energy resolution. Studies about the evolution of the energy distribution inside the electron pulses is presented in this section.

The evolution of the energy distribution (FWHM) as a function of the applied bias at the Wehnelt electrode is displayed in figure 4.22a. For the same settings, the total electron current on the viewing screen was measured (figure 4.22b), which linearly scales with the number of electrons per pulse.
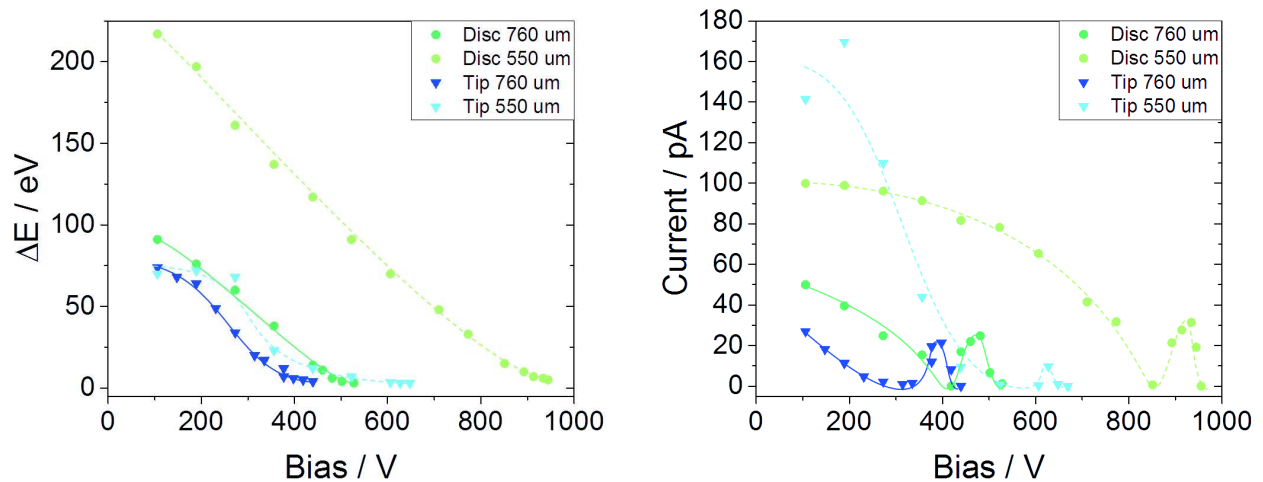
(a) *Energy distribution (FWHM) of the total emission.*

(b) *Total current on the viewing screen.*

Figure 4.22: *Evolution of the energy distribution and total current measured at viewing screen as a function of the Wehnelt bias for two different cathode shapes and positions. Truncated tip in dark and light blue triangles, disc in green dots. Dark color and solid lines represent a distance of 760 μm, light color and dashed lines 550 μm.*

For every cathode shape and position the energy distribution is the highest at minimum bias, decreasing drastically with increasing Wehnelt bias. A similar behavior is observed for the current as a function of the Wehnelt bias. Looking for example at the light green dots which represent the measurements from a disc shaped cathode at small cathode-Wehnelt gap, the current is the highest at low bias, decreasing to a local minimum at ~850 V. Upon further increased bias the current shows a peak before the emission is completely extinct. The position of the peak corresponds to the bias voltage where the small halo appears in the emission pattern. The behavior is qualitatively consistent for any cathode shape and position. The tip at short gap shows an unusually high current at low bias. This will be further investigated in the following experiment.

The data presented above demonstrate, that the emergence of the small halo causes an increase in current, thus increases the number of electrons reaching the detector. This seems logical as a second electron population is added to the on-axis emitted electrons. Contrary, the energy distribution is not influenced by the mixing of the populations. In consequence, the off-axis halo-electrons must possess an energy width inferior or equal to that of the on-axis electrons for the given Wehnelt bias at which the halo appears.

The emission from the truncated tip at small cathode-Wehnelt gap is investigated in more detail, measuring different contributions separately. In figure 4.23 the shank emission is represented as yellow circles, central emission with black triangles.
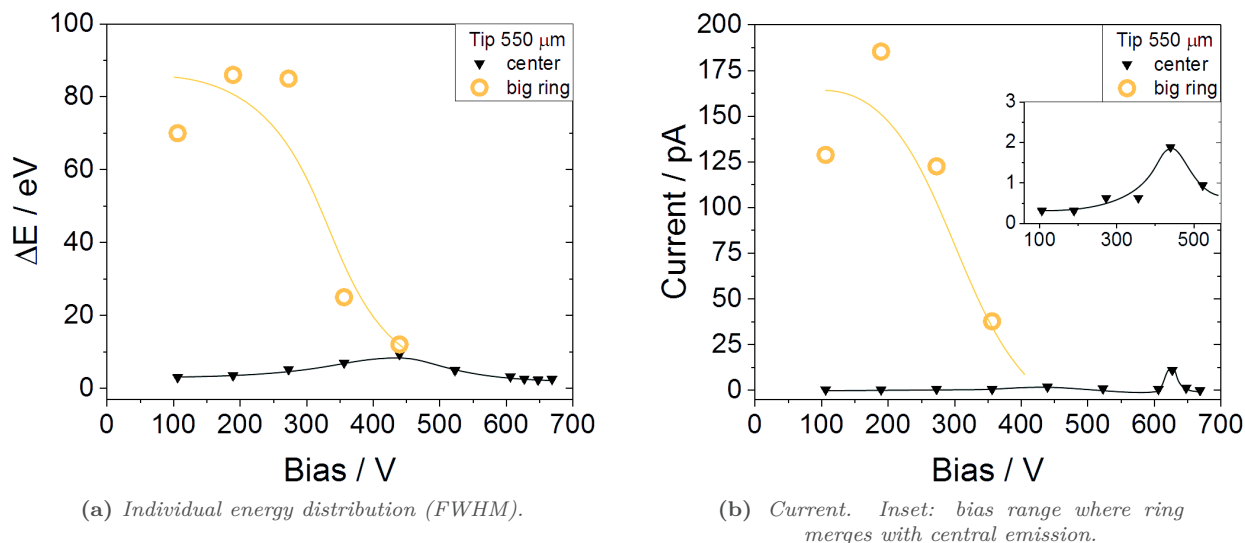
(a) *Individual energy distribution (FWHM).*

(b) *Current. Inset: bias range where ring merges with central emission.*

Figure 4.23: *Evolution of the energy distribution and current as a function of the Wehnelt bias, measured individually for the shank-emission ring and the central emission of the truncated tip at 550 µm. Curves are added to the data points as guide to the eye.*

The evolution of the energy distribution (figure 4.23a) differs greatly for the central emission and the shank electrons. The shank emission shows a high ΔE around 80 eV at low bias, which drops rapidly until the shank electrons disappear. The central emission has a low energy distribution below 10 eV throughout the whole bias range, showing one peak around the extinction of the shank emission.

The measured currents show a similar behavior in figure 4.23b. The shank emission contributes a high current at low bias, decreasing until complete extinction. The current of the central spot is generally weak, only twice rising above 2 pA. The first small peak is enlarged in the inset. It coincides with the extinction of the shank-emission. The second and more pronounced peak is at the bias threshold where the aberration-induced halo appears, as discussed above.

These individually measured electron populations demonstrate, that the unusually high total current of the tip emitter at short Wehnelt gap (figure 4.22b) originates from the shank emission, which does not exist for other cathode shapes and positions.

The correlation of current and energy distribution can signify a reduced number of electrons per pulse, a reduced electron density and thus less Coulomb interactions and especially Boersch effect. However, the laser pulse energy is kept constant. It seems surprising that the Wehnelt bias limits the photoemission to this extent.

An alternative explanation can be chromatic filtering. This would imply that the filtered electrons either posses high or low energies in order for the resulting fraction to be more homogeneous in energy. Herefore, the electrons would have to be spectrally dispersed.

The shank emission ring being the electron population with the highest current, allows a detailed analysis at high magnification of various positions within the ring. In figure 4.24a EEL spectra are shown for different zones of the shank-emission (blue and red spectra), as well as a spectrum containing all ring-electrons (black spectrum).
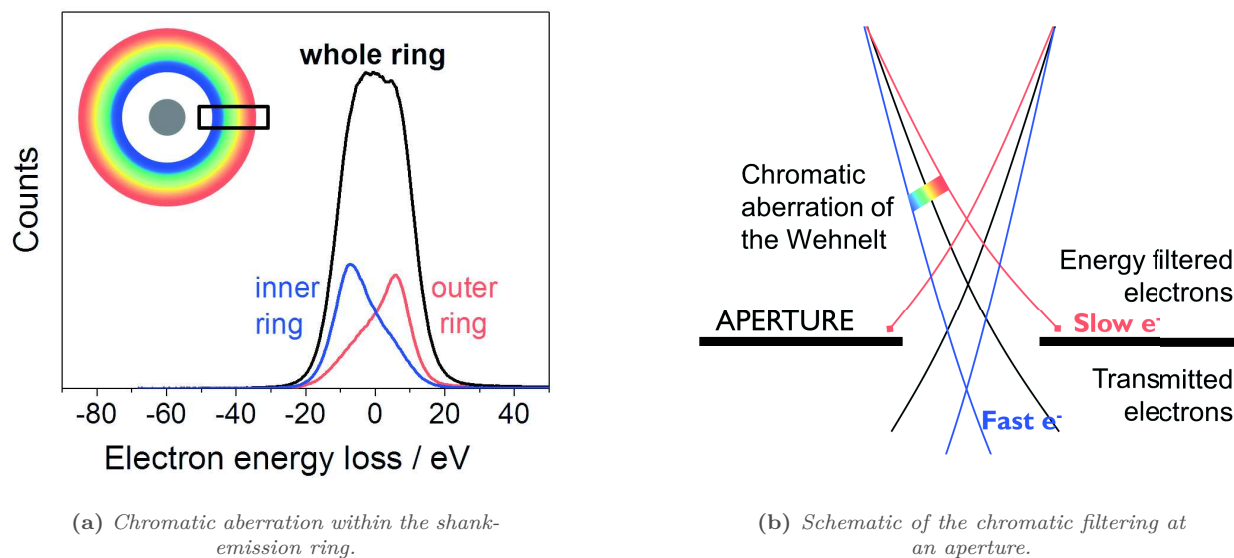
(a) *Chromatic aberration within the shank-emission ring.*

(b) *Schematic of the chromatic filtering at an aperture.*

Figure 4.24: *Chromatic aberration shown within the big shank-emission ring of the Ta-tip at 550 µm at minimum Wehnelt bias. The rainbow scheme indicates the energy distribution with red being low energy (outer ring) and blue representing high energy (inner ring). The schematic sketch in (b) demonstrates the chromatic energy filtering effect.*

The blue spectrum taken from the inner ring shows a higher electron energy (negative energy loss equals energy gain) than the red spectrum taken from the outer ring. A schematic drawing in the upper left corner demonstrates the corresponding spectral energy dispersion in rainbow colors, with red representing lowest energy and blue for high energy electrons.

The central emission spot or the small halo do not provide enough counts upon high magnification for good quality spectra. Nevertheless, the same trend has been found with low energetic electrons in the outer sphere and higher energy towards the optical axis.

With this prove for chromatic dispersion inside the emission pattern a chromatic filtering effect can be stated. The reduced energy width together with a reduced current upon increasing Wehnelt bias (figure 4.22) can now be attributed to chromatic filtering.

Most likely, the chromatic aberration of the Wehnelt electrode induces the chromatic dispersion. No other lens current has shown an influence on the energy width of the electron beam, stating that the filtering happens above the condenser lenses. This leaves the Wehnelt as sole electro-optical component, which is furthermore known to have a poor lens quality and a high chromatic aberration. A schematic of the filtering effect is shown in figure 4.24b.

4.4.3   Influence of Other Instrumental Parameters

All lens currents of the illumination and imaging system have been investigated individually using free lens control. For all electromagnetic lenses (including the additional C0 lens), no major effect on temporal or energy width could be observed. These lenses exclusively change the coherence of the electron beam by focusing more or less electrons onto the sample while the rest of the beam is sheltered on apertures. This is the compromise between signal and coherence, as discussed earlier.

4.5   Summary and Discussion of Electron Pulse Dynamics

The comparison of energy spread and signal intensity reveal a severe filtering, which happens upon increased Wehnelt bias. Detailed EELS analysis show a spectral dispersion within the emission pattern. This is the basis for chromatic filtering, whereby the energy distribution and signal are reduced at the same time. With constant apertures, an increased Wehnelt bias enlarges the beam spread and thereby the chromatic filtering. Likewise, the use of smaller apertures can reduce the effective energy width of the electron beam reaching the sample. The poor lens quality of the Wehnelt electrode, especially the high chromatic aberration, is responsible for the spectral dispersion. Consequently, the main energy broadening has to happen within the Wehnelt cone, before the electrons pass through the electrostatic lens.

Generally, Coulomb interactions can happen at various positions throughout the microscope. After the space charge at the cathode surface every cross-over represents a moment of high electron density, where homogeneous and inhomogeneous effects can occur, such as lateral space-charge, Boersch effect and trajectory displacements. According to the chromatic filtering, space charge and Boersch effect at the cathode represents the major contribution to energy broadening. It is sensible, that most interaction happens right after the generation of the electron pulse. The electrons are not yet accelerated and interaction time is high. Also, the maximum number of electrons is present. No filtering has occurred yet, neither chromatic filtering, nor conventional filtering as it happens in any standard TEM (1% of the generated electrons reach the sample in conventional TEM). Certainly, the gun cross-over also plays an important role, as it is located inside the accelerator, where the electrons have not yet achieved their final speed. However, this cross-over can not be investigated independently, as the Wehnelt bias, which is responsible for its formation and exact location, has multiple other influences, which will be discussed later. Subsequent focal points have no measurable effect on neither temporal nor energy spread. This is most probably due to the reduced charge density as electrons were lost in the column, and a shorter interaction time of the fully accelerated electrons. Furthermore, the electron pulses possess a more favorable aspect ratio. Due to temporal elongation to a few picoseconds, the cross-overs are pencil-shaped more than pancake-shaped close to the emission zone.

Regardless of the chromatic filtering, the influence of a given initial energy distribution on the temporal elongation of an electron pulse is worth to be considered. Unfortunately, experimental measurements are impossible as other effects such as filtering overlap. However, a theoretical approximation can be made. In literature [77] the acceleration-propagation model is used for this purpose. It estimates the effect of an initial kinetic energy distribution on the temporal elongation throughout acceleration and propagation in an electron microscope. The initial energy spread ΔE is converted to a momentum spread, which causes an inhomogeneous propagation speed of the electrons.

Supposing a linear acceleration, the following expression is used to approximate the temporal spread in the acceleration regime:

$$\Delta t_{acc} \approx \frac{d}{eU} \cdot \frac{\Delta E}{v_i} \tag{4.2}$$

with d: distance, e: elementary charge, U: acceleration voltage and v_i: initial speed.

In the field-free drift section the pulse length will be further amplified. The additional temporal broadening of the now relativistic electrons can be calculated with

$$\Delta t_{drift} = \frac{t}{\beta^2 \cdot \gamma^3} \cdot \frac{\Delta E}{m_e c^2} \tag{4.3}$$

with t: average travel time, m_e: electron mass, c: speed of light,
and the relativistic factors for 200 keV electrons $\beta = \frac{v}{c} = 0.69$, γ= 1.39: Lorenz factor.

The total electron pulse length is composed of the initial laser pulse length, the elongation in the acceleration regime and the contribution of the field-free propagation:

$$\Delta t_e = \Delta t_{laser} + \Delta t_{acc} + \Delta t_{drift} \ . \tag{4.4}$$

An initial energy spread of 0.6 eV being the theoretical limit upon photoemission (eqn. 3.3) results in a medium kinetic energy $\langle E_i \rangle = 0.3$ eV and a medium initial speed $v_i = \sqrt{\frac{2\langle E_i \rangle}{m_e}} = 3.25 \times 10^5$ m/s. With $d = 0.1$ m and $U = 200$ keV the temporal broadening in the acceleration regime is 0.9 ps. The contribution of the drift section (0.8 m $\rightarrow$ $t = 3.8$ ns @ 2.07×10^8 m/s) yields 4.9 fs. The total temporal pulse length including the laser pulse length of 370 fs is $\Delta t_e = 1.3$ ps.

A large initial energy spread of 200 eV with a medium initial speed of 5.6×10^6 m/s ($\langle E_i \rangle = 100$ eV) results in a temporal broadening of $\Delta t_{acc} = 18$ ps and $\Delta t_{dift} = 1.2$ ps. The overall temporal spread adds up to a pulse length of 20 ps.

These values have to be taken as a rough estimation, as the model is very simplistic. For instance, a homogeneous energy distribution is assumed, which is certainly neither the case in electron pulses photoemitted with a Gaussian laser profile, nor for emission from realistic cathodes having a particular surface structure, grain boundaries, defects, etc. which lead to local "hot spots". Furthermore, the model assumes a homogeneous acceleration (the TEM pocesses 4 acceleraction steps) and no significant change in the gun cross-over. Finally, the formula for the acceleration regime is invalid for very small initial speeds as for $v_i \rightarrow 0$ the temporal elongation would be infinite.

The experimentally determined electron pulse length as a function of the Wehnelt bias showed the existence of two regimes. One low-bias regime implies very moderate temporal elongation, in a second high-bias regime the pulse length seems to explode. The calculated values of some ten picoseconds corresponds to the order of magnitude of the low-bias regime. It can be assumed, that Coulomb interactions are dominating this first regime.

The abrupt increase after a threshold bias results in a second regime, which could experimentally be relayed to another phenomenon. The electrostatic field distribution in the Wehnelt cone causes the electrons, which are emitted at different angles, to discriminate in two separate populations. These are either emitted along the optical axis or off-axis (visible as a *central spot* with a *small halo*). Detailed analysis of the individual electron populations revealed that the off-axis electrons are strongly retarded with respect to the central on-axis emission. This can be related to the strong electrostatic potential barrier experienced near the edges of the Wehnelt aperture, in combination with a longer trajectory path as they deviate around the optical axis while being focused by the illumination lens system. The off-axis halo is sheltered at low Wehnelt bias and only appears when high bias voltages are applies. The threshold between the two pulse length regimes coincides with the appearance of the small halo. The dramatic pulse elongation in the second, high-bias regime can thus be attributed to the mixing of two populations with differing arrival times.

The study of the arrival times furthermore revealed a general retarding of the electron pulse upon increasing Wehnelt bias. The enhanced electric field consequently retains the electrons for a longer time inside the Wehnelt cone before they reach the accelerator. An increased potential on the Wehnelt acts inside the cone in two ways. First, it defines the extraction field which electrons feel on the cathode surface. And second, it creates a potential barrier on the way through the Wehnelt aperture.

With these findings, the evolution of the energy distribution as a function of the UV laser power, which was presented in the very first section of the result, can be fully understood. The measured current on the viewing screen increased as a function of the UV laser power, which corresponds to an increased number of electrons per pulse. This increase is less pronounced for high Wehnelt bias. Here, the chromatic filtering effect comes into play. At high bias more electrons are filtered, thus only few of the additionally generated electrons actually reach the detector. The same behavior is seen in the evolution of the energy spread as a function of the UV power. ΔE increases with increasing laser power, but the effect is less pronounced at high bias.

An additional aspect can be observed in the plot of the electron current. The high-bias curves show a slight trend to saturation. This could be related to lateral space charge inside the Wehnelt cone. The Child's law limits the photoemission if the electron density reaches a certain value due to the retarding effect of the Wehnelt potential.

In summary, the evolution of ΔE and Δt_e were found anti-correlated when the Wehnelt bias is changed. This states that Coulomb interactions can not predominate the characteristics of the electron pulses, as both parameters would have to be correlated. Regarding the temporal pulse elongation, a first regime has been found to match Coulomb interactions. However, the major factor which limits temporal resolution are trajectory effects of electrons leaving the cathode at different angles. The main effect which determines the width of the energy distribution was identified to be chromatic filtering.

4.5.1   Experimental Trade-offs

The important conclusion regarding materials science applications is the realization that not all pulse characteristics can be optimized at the same time. Trade-offs are inevitable between temporal resolution, energy resolution, spatial resolution and signal intensity (signal to noise ratio). The parametric study presented in this chapter can serve as a guide to find appropriate compromises for specific experimental needs.

The emitter shape and position are the first choices to make. A disc-shaped emitter with its large emission area results in high signal but low coherent electrons. The central emission of a truncated tip offers the opposite: highly coherent, low-intensity electron pulses with best temporal and energy resolution. The shorter the distance to the Wehnelt aperture, the more electrons are transmitted resulting in higher signal but again lower coherence.

Special attention should be given to the use of only one electron population. The so-called "saturated emission" used in conventional thermionic emission has to be omitted, as greatly retarded off-axis electrons would be mixed with the on-axis central emission which results in a drastic loss of time resolution.

For most applications the central emission spot of a disc emitter at short cathode-Wehnelt gap will be used. This represents the most versatile configuration, enabling high signal for imaging or a narrow energy width

for EELS experiments after severe chromatic filtering. Figure 4.25 shows a three dimensional plot where the interplay of the key variables Δt_e, ΔE and signal intensity is visualized for the low-Δt_e regime (before the mixing with off-axis electrons). The signal intensity is displayed as electric current measured on the viewing screen. The plot is composed of four color coded series at different bias settings. Within each series the UV laser power was varied, which corresponds to a change of the number of electrons emitted per pulse.
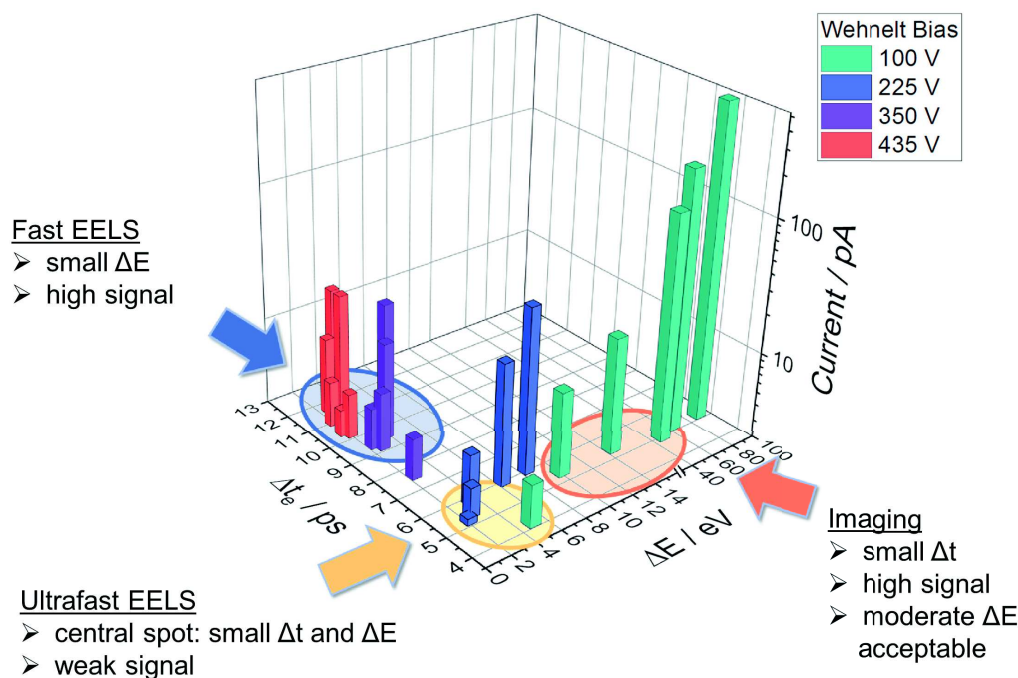
Figure 4.25: *Reference 3D-plot for experimental trade-offs between signal, temporal and energy resolution. The workable low Δt_e regime of a disc-shaped emitter at 760 μm is shown where only central emission is present.*

The graph demonstrates, that high temporal and energy resolution can only be attained with weak electron pulses. For higher signal either temporal or energy resolution has to be sacrificed. Likewise, for best temporal resolution signal and ΔE can be traded off. In fact, signal and ΔE are correlated, whereas Δt_e is anti-correlated because of chromatic filtering. The strong chromatic aberration of the electrostatic Wehnelt lens turns out to be a useful tool to reduce the energy width of the electron pulse.

In imaging, for example, signal intensity is of highest priority. A compromise with moderate ΔE is reasonable, as long as chromatic aberration does not significantly reduce the image quality (see orange region indicated on graph). EELS, on the other hand, requires best energy resolution. In order to gain signal intensity the temporal resolution can be traded off. This, of course, depends on the speed of the sample transformation under investigation. An advantage of EELS is that sample drift plays a minor role, as long as the fine structure is not analyzed in detail. Therefore, longer acquisition times can be managed more easily to compensate low signal. The same applies to electron diffraction, in contrast to real space imaging where drift is detrimental.

Coherence is the main drawback of the large disc-emitter. In this regard, the central emission of a tip-shaped emitter is better by far. However, the amount of electrons which can be extracted from the small emission area is very low. In practice, this often inhibits potential applications; especially imaging is impossible.

A second and more useful characteristic of the tip-shaped emitter is an optimized temporal resolution. As it can be seen in figure 4.16 the temporal length of the electron pulse as a function of bias show two very distinct regimes for tip emitters. The first regime is almost horizontal, meaning the pulse length stays constant throughout the chromatic filtering upon which the energy resolution can be optimized. The ideal setting for ultrafast EELS is around the threshold bias, right before the pulse length increases drastically, because Δt_e and ΔE are minimized at the same time. Evidently all shank-emission has to be sheltered. The easiest way is by choosing a big cathode-Wehnelt gap, where shank electrons are blocked by the Wehnelt. Otherwise, apertures have to be used.

Only in rare cases the use of shank-emission can be advantageous. This electron population is very intense and has a short temporal length. But as the energy distribution is huge, chromatic aberration and low coherence limit high resolution imaging and precludes EELS. For imaging at low magnification it might be sufficient and would enable short acquisition times with high temporal resolution.

Last but not least, the retarding effect of the Wehnelt bias is important to be understood for time-resolved experiments. It does not play a direct role for the experiments, but it clearly states the necessity of calibration every time a parameter has been changed. Most likely, after a successful time-resolved experiment the PINEM-sample will be inserted to post-calibrate the data with the exact same settings.

4.6 Conclusion

The findings of this detailed study allow to trace the electron pulse dynamics in an ultrafast electron microscope with thermionic gun and Wehnelt electrode. The temporal component of this UTEM enabled an in-depth understanding of distinct electron populations described decades ago in conventional electron microscopy, as well as their influence on pulsed operation. Key parameters could be identified for the optimization of time-resolved experiments.

Coulomb interactions mainly occur as space charge and Boersch effect at the cathode surface, a minor contribution happens in the gun cross-over. In both sectors, high electron density and long interaction times coincide. Subsequent focal points have no measurable effect. The impact of Coulomb interactions is primarily visible in an increased energy spread (up to 200 eV). The influence in terms of temporal broadening is of minor importance, the pulse expands up to some ten picoseconds.

The main contribution to temporal pulse elongation is the superposition of distinct electron populations, which was revealed by an accurate analysis of individual electron populations. In this study, the temporal character of the long known populations could be identified. The off-axis halo electrons are strongly retarded with respect to the central on-axis emission (> 100 ps). The shank emission is slightly retarded (~15 ps). The major reason is different trajectories caused by the emission angle and differing potential barriers experienced thereupon. Mixing two electron populations results in very long pulses and thus a great loss of temporal resolution. This happens at the so called "saturated" emission used in conventional electron microscopy, where central emission and halo are merged. Under all circumstances this has to be omitted in pulsed operation.

Comparing the electron pulse length and energy distribution an anti-correlation occurs. This could be related to a chromatic filtering. Due to the chromatic dispersion induced by the Wehnelt electrode, the electron beam is energetically refined when passing through apertures such as the first anode.

Regarding optimum operation for time-resolved experiments, two main parameters have to be adjusted. First, the UV laser pulse energy, which defines the initial number of electrons per pulse and thereby modifies the signal intensity, but also the electron density which plays on all Coulomb interactions. The Wehnelt electrode is the second and most complex parameter. The electrostatic potential controls the emission area, the extraction field on the emitter surface, the potential barrier that electrons have to overcome while passing through the Wehnelt aperture, as well as the position and size of the gun cross-over (inside the accelerator). The strength of the Wehnelt electrode defines the exact height of the cross-over, and thereby the position at different electron energies along the accelerator; the convergence angle sets the volume and shape of the spatial confinement. These factors define the electron density and the interaction time and thereby the extent of Coulomb interactions. Furthermore, the chromatic aberration of the Wehnelt electrode and the resulting chromatic dispersion of the electrons is the basis for chromatic filtering. This is essential to refine the energy distribution of intense electron pulses and make experiments possible. A minor parameter is the additional condenser lens C0, which helps to gain signal (a factor of 10 to 20) on the expense of spatial coherence. The applied voltage is generally kept constant. For fine-tuning the condenser aperture, spotsize, convergence angle and beam spread have to be adjusted.

Single-Shot UTEM - Development and Characterization

This chapter contains the second experimental part of my thesis. The implementation of the nanosecond operation mode into the UTEM will be presented. The potential in imaging, electron diffraction and electron energy loss spectroscopy will be studied, showing the interplay of chromatic aberration, spherical aberration and signal intensity. Directions will be given to obtain optimum results in materials science application.

The results of this chapter will be published in: "Imaging and Electron Energy-Loss Spectroscopy using Single Nanosecond Electron Pulses", K. Bücker, M. Picher, T. LaGrange, F. Banhart, *submitted*.

Particularity of this instrument

At the present day only one other functional single-shot electron microscope exists worldwide. The one in Strasbourg is the first one to be equipped with an electron energy loss spectrometer, enabling an in-depth understanding of the electron pulse properties, as well as the potential for EELS studies.

This ultrafast electron microscope will be a versatile instrument for materials characterization, as it can switch between stroboscopic and single-shot mode, depending on the sample and process under investigation. Knowing that the vast majority of material transformations are irreversible, great interest lies in the development of this single-shot mode.

5.1 Design Considerations

For the investigation of irreversible processes, the number one target of single-shot setups are intense electron pulses without devastating Coulomb interactions. Therefore, a moderate electron density has to be maintained in the pulse. This can be achieved by adjusting the pulse duration and thus the extension along the optical axis of the microscope. However, a long and intense laser pulse can potentially harm the emitter surface, as high energy is applied during a longer time span. Reducing the wavelength of the laser increases the quantum efficiency significantly. Thereupon, the laser power can be lowered while the same number of electrons is emitted. For this reasoning, a nanosecond laser with 5th harmonic module has been chosen to drive the photoemission ($QE = 10^{-4}$ at 211 nm, compared to 10^{-5} at 266 nm [26]). The repetition rate does not play a role for single-shot experiments. Nevertheless, for alignment issues it is useful to have a quasi continuous beam for the human eye, which is the case for a repetition rate of 20 Hz. Table 5.1 summarizes the laser specifications.

Table 5.1: *Specifications of the Litron Nano T laser system.*

5th harmonic	213 nm
pulse duration	7 ns
repetition rate	0 - 20 Hz
pulse energy	0.4 mJ @ 213 nm

The photon energy of 5.8 eV induces a kinetic energy distribution of 1.7 eV upon photoemission from a tantalum cathode ($W_{Ta} = 4.1$ eV [74]).

A Gaussian laser profile (TEM_{00}) was chosen once again. This enables more compact optics, making it possible to integrate the setup onto the existing optical tables. As discussed in detail (section 3.4.1, page 20) the alignment is simpler and more robust.

Approximation of the electron density

The crucial value for energy broadening is the electron density, especially in the gun region where the electrons are not yet accelerated and the interaction time is high. Calculations can give an indication of the feasibility of single-shot TEM, especially regarding EELS experiments.

An exemplary calculation is demonstrated for a low UV energy of 20 µJ. The number of photons per pulse

results form the pulse energy divided by the photon energy:

$$photons/pulse = \frac{E_{pulse}}{E_{h\nu}} \tag{5.1}$$

With a photon energy of 5.8 eV (213 nm), the UV energy of 20 µJ yields a total of 2.15×10^{13} photons per pulse outside the TEM column. The number of photons contributing to photoemission is reduced. Only those reflected by the Mo-mirror and those not reflected by the Ta-cathode will generate electrons with the specific quantum efficiency:

$$electrons/pulse = photons/pulse \cdot R_{Mo} \cdot \frac{1}{R_{Ta}} \cdot QE \tag{5.2}$$

with R: reflectivity.

With $R_{Mo} = 0.5$, $R_{Ta} = 0.7$ and $QE_{Ta, \, 213 \, nm} = 10^{-4}$, the number of electrons emitted per pulse is 3.23×10^8. This value can be related to the pulse length, yielding a number of electrons per time.

$$\varrho_e = \frac{electrons/pulse}{\tau_{UV}} \tag{5.3}$$

with ϱ_e: electron current, τ_{UV}: UV pulse duration.

For a 7 ns photon pulse, 4.6×10^{16} electrons are emitted per second. This value does not represent the actual electron density as the spatial extension of the pulse is not taken into account. Without accurate simulations, it is impossible to estimate the expansion due to space charge. However, the number of electrons emitted per time unit serves to compare different situations at the cathode.

In table 5.2 the single-shot setup is compared to the stroboscopic UTEM. The two setups differ in numerous ways, e.g. the laser wavelength and pulse duration, the resulting quantum efficiency and mirror reflectivity. For each setup, two operation scenarios are depicted at different laser pulse energies.

Table 5.2: *Comparison of the electron density and relevant parameters of the single-shot and stroboscopic UTEM setups in Strasbourg.*

	single-shot UTEM		stroboscopic UTEM	
	low UV	high UV	best EELS (2 MHz, 1 mW)	common operation (500 kHz, 1 mW)
laser pulse energy	20 µJ	565 µJ	0.5 nJ	2 nJ
wavelength	213 nm		258 nm	
photon energy	5.8 eV		4.8 eV	
photons per pulse	2.2×10^{13}	6.1×10^{14}	6.5×10^9	2.6×10^8
UV mirror reflectivity	65% (Mo)		75% (Al)	
Ta-cathode reflectivity	70%		70%	
Quantum efficiency [75]	10^{-4}		10^{-5}	
electrons per pulse	4.2×10^8	1.2×10^{10}	1.5×10^3	6×10^3
laser pulse duration	7 ns		370 fs	
longitudinal extension	2.1 m		0.1 mm	
electron current	6.0×10^{16} s^{-1}	1.7×10^{18} s^{-1}	4×10^{15} s^{-1}	1.6×10^{16} s^{-1}

As desired, the resulting electron densities are in the same range for both operation modes. Nevertheless, the single-shot setup at low UV energy lies a factor of four above the common stroboscopic operation, and even one order of magnitude higher compared to the setting used for best stroboscopic EELS resolution. There, a zero-loss peak of 0.79 eV was achieved (see section 4.2.1 on page 28). The shorter wavelength chosen for the ns-setup provokes a theoretical limit of 1.7 eV, which adds an additional challenge on the way to narrow energy distribution in nanosecond electron pulses.

For the single-shot setup at high UV energy right before the ablation limit, the electron density is even two orders of magnitude above the common stroboscopic operation.

These values represent the situation at the cathode. Evidently, only a fraction of those electrons arrives at the sample and at the detector. Approximately 10% of the electrons emitted at the cathode reach the specimen in pulsed operation. Knowing from the Rose criterion that an EEL spectrum requires $10^4 - 10^5$ electrons, the necessity of careful filtering is evident. With 10^8 electrons per ns-pulse there is some room, but single-shot EELS remains challenging.

5.2   Implementation of the Single-Shot Setup

The integration of the single-shot setup is part of the UTEM project and was done without the help of industrial partners.

5.2.1   Optical Setup

The implementation of the nanosecond laser into the existing UTEM setup requires careful planning. Especially, as quick switching between the two operation modes (stroboscopic and single-shot) should be guaranteed. Both UV lasers (fs- and ns-laser) need to enter the microscope at exactly the same position and angle. This requires a retractable mirror to change from one operation mode to the other.

The new laser was integrated on the right optical table of the UTEM setup, see schematic in figure 5.1. The optical beam path contains the same components as installed in the femtosecond beams (described in section 4.1). These are a Keplarian telescope composed of two convex lenses ($f_1 = 200$ mm, $f_2 = 500$ mm) to expand the beam by a factor of 2.5 and an attenuation unit composed of a half wave plate to change the linear polarization and an adjacent polarizing beam-splitter cube. A schematic of the working principle of the attenuation can be found in figure 4.3 on page 27. A third lens with a focal length of 1 m focuses the beam onto the cathode.
An advantage of the Keplarian telescope, in contrast to a Galilean beam expander, is the cross-over between the two convex lenses. This can be used to optimize the laser beam quality: a pin-hole (150 μm) is inserted in the focal plane as spatial filter.

In order to superimpose both UV-beams, a mirror was mounted on a flip-mount, which is inserted when the nanosecond beam is used, and retracted for stroboscopic fs-operation. This is done right before the TEM column, so that no optical component outside the TEM has to be used by both UV beams. This is crucial, as the beams need different optics with special coatings, optimized for the wavelength and the dose proper to each laser (pulse energy and pulse length vary by several orders of magnitude).
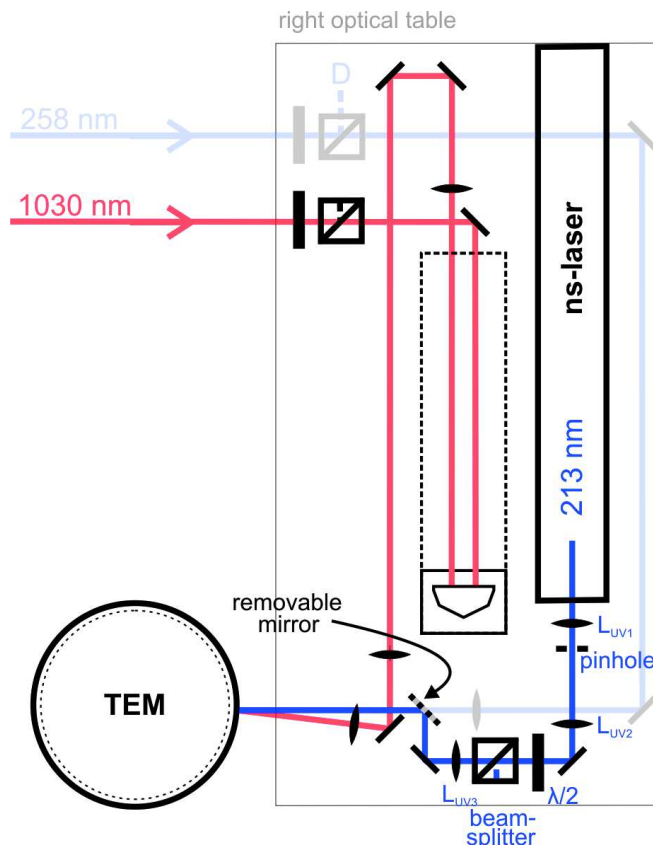
Figure 5.1: *Schematic drawing of the optical setup for single-shot UTEM in Strasbourg. The femtosecond beams are unchanged. The nanosecond laser is integrated on the right optical table. Its beam path contains a Keplarian beam expander (L_1,L_2), an attenuation unit (half-wave plate + polarizing beam-splitter) and a focusing lens (L_3). A mirror positioned on a flip-mount allows to switch between the ns and fs UV-beam.*

The sole commonly used component is the UV mirror inside the microscope. This is inevitable but challenging. The aluminum mirror used in stroboscopic mode turns out to be a bad choice as the reflectivity is too low for the wavelength of the 5th harmonic. Molybdenum was found to present acceptable reflectivity for both wavelengths (table 5.3) as well as a high stability.

Table 5.3: *Reflectivity measurements of the metal mirrors.*

Metal	Reflectivity	
	at 258 nm	at 213 nm
Al	75%	24%
Mo	75%	66%

Special care has to be taken to X-ray safety. The exchange of the UV-mirror inside the TEM changes the wavelength of the emitted X-rays due to electrons hitting the metal mirror. With the aluminum mirror, the adjacent UV-window made of quartz glass was appropriate to absorb the electromagnetic radiation. Al and Si are neighboring elements in the periodic table, therefore Si absorbs X-rays emitted by the Al. Molybdenum, on the other hand, emits radiation of a higher frequency (Mosely's law). Unfortunately, there is no neighboring element in the periodic table which could be used as window material, capable at once of absorbing the electromagnetic radiation, as well as transparent and resistant to UV. Thus, the only solution is heavy X-ray shielding with an assembly of lead and tungsten which encapsulates the whole optical table

in line with the X-rays leaving the microscope through the standard quartz window. This is the front part of the right optical table.

5.2.2 Electronic Coupling

The work with two individual lasers for pump and probe pulses requires an electronic coupling, which includes an electronic delay module. Contrary to the stroboscopic mode, an optical delay is not feasible as the required distances are too long (e.g. 1 µs $\widehat{=}$ 300 m). The precision of electronic delays generally depends on the delay length. In this case of large delays, a high precision instrument is essential.

A schematic of the electronic setup is presented in figure 5.2. The femtosecond laser is used as clocking unit. Its oscillator operates at 40 MHz, which is impossible to be triggered by the nanosecond laser, having a maximum repetition rate of 20 Hz.
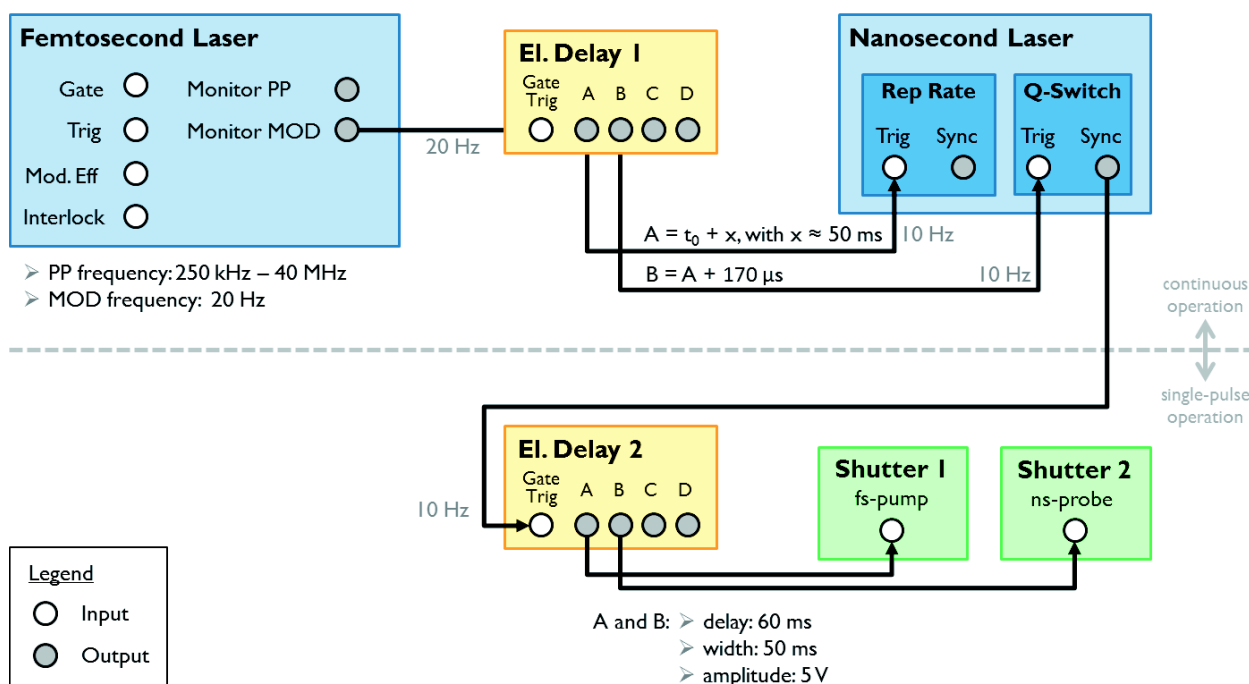
Figure 5.2: *Schematic drawing of the electronic coupling to operate in single-shot mode. The femtosecond laser modulator is the clocking unit, used as time zero for a first electronic delay. This triggers the nanosecond laser, first the flash-lamp and 170 µs later the Q-switch. The latter triggers a second electronic delay, used to actuate the shutters for pump and probe beam.*

The modulator of the fs-laser is set to a frequency of 20 Hz to match the ns-laser. This signal is used as trigger for the first electronic delay module. This then triggers the nanosecond laser, which requires a first signal (channel A) for the flash-lamp and a second one (channel B) 170 µs later for the Q-switch to actually let a pulse through. The signal of the Q-switch is used as input for the second delay module, which will actuate two shutters. These are installed in each laser beam path and generally block the beams. When the delay box sends out a signal the shutters will be opened once to let a pulse through and will be closed shortly after, before a second pulse arrives. Hereby, the single-shot operation is realized.

The schematic in figure 5.3 illustrates the sequence of triggering. In gray at the top of the sketch the internal processes of the femtosecond laser are depicted. The oscillator always operates at 40 MHz. The pulse picker

(PP) then selects the fraction which will be amplified (e.g. 250 kHz). The final pulse energy depends on the PP, as the total power of amplification stays constant. The modulator (MOD) selects among the amplified pulses which ones will exit the laser box. Here, the repetition rate can be adapted to match the nanosecond laser.
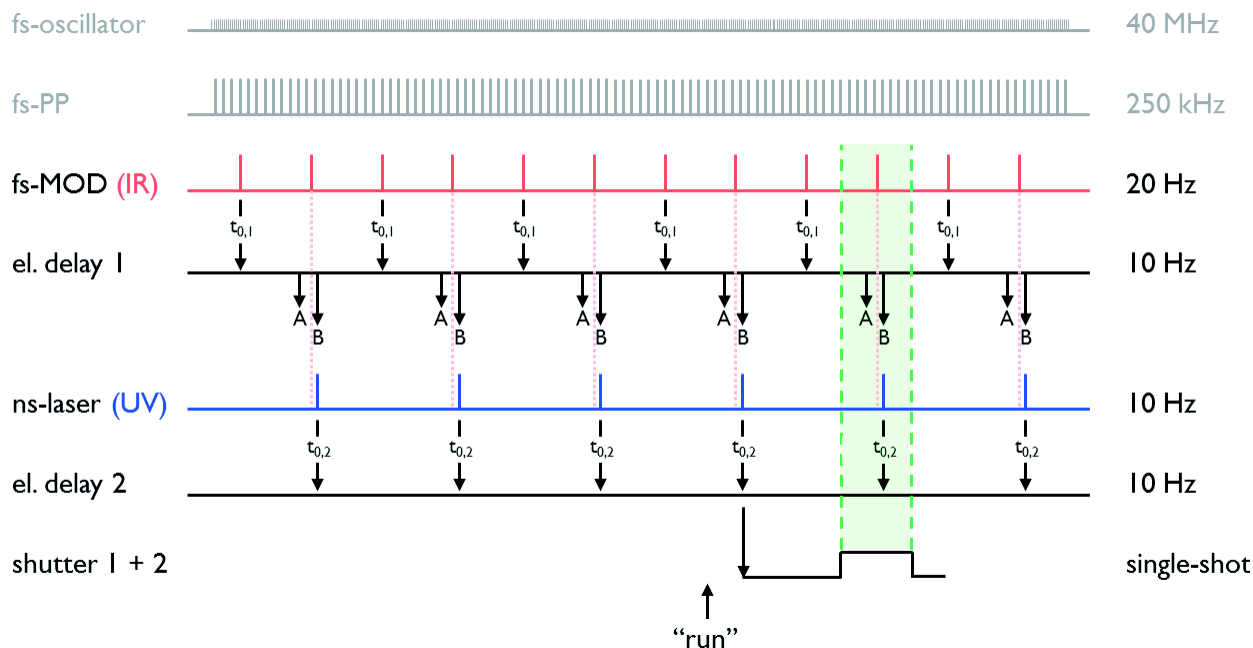

Figure 5.3: *Schematic drawing of the electronic triggers used for the electronic coupling in single-shot operation. On the right hand side the repetition rates are noted. Steps inside the fs-laser module are shown in gray (oscillator, pulse picker), the resulting fs beam in red (after modulator). The first electronic delay prompted by the fs-MOD triggers the ns-laser (A: flash-lamp, B: Q-switch). The resulting UV-pulses (blue) the second el. delay which actuates the shutters in single-shot operation mode, selecting one pair of pump-probe pulses after initiation ("run") to enter the microscope (highlighted in green).*

The MOD-signal of 20 Hz is used as time zero for the first electronic delay, which synchronizes both lasers. However, signal A must trigger the flash-lamp 170 μs before the desired ns-pulse (intrinsic to the laser). As a delay module can never be set to negative values, the ns-pulse has to be delayed by almost one period to match the next fs-pulse. In consequence, the delay module is busy when the next fs-signal arrives (red dotted lines), so every second fs-signal will be ignored. This is the reason, why the repetition rate of the ns-laser is divided by two in comparison to the fs-laser pulses.

The second delay module, responsible for the shutters, receives its time-zero from the ns-laser. This module is set to single-shot operation. After activating the "run"-button, the module waits for the next t_0-signal to execute the programmed electronic pulse, which opens and closes the shutters. In fact, the Thorlabs shutters used in this setup, open when the electric signal rises and close when the voltage drops. Thus, the opening time can be tuned with the duration of the 5 V signal.

5.2.3   Synchronization

The exact synchronization, as well as changing the delay of pump and probe pulse during time-resolved experiments, is done electronically. The tunable value is the delay of channel A in the first electronic delay unit ($A = t_0 + \mathbf{x}$). All other triggers refer to the parameter A.

To monitor the arrival of the fs-IR and the ns-UV pulses, photo-diodes are installed before the shutters of each beam. These sensitive detectors are able to operate below one percent of the pulse intensity, so they can be positioned behind any non-metallic mirror and give an online-signal during the operation of the microscope. The signal is monitored by an oscilloscope. The difference of the beam paths after the diode positions has to be calculated, including the electron trajectory with an approximated time for the acceleration. Evidently, this procedure is less precise than PINEM experiments in stroboscopic operation. But as the electron pulse length is three orders of magnitude larger, this method is sufficiently accurate for the temporal resolution required here. For example, electron trajectories or the retarding effect of the Wehnelt bias, which can rise up to a hundred picoseconds, are negligible for electron pulses of several nanoseconds.

5.3 Microscopy Techniques

5.3.1 Imaging

At first, the capabilities of imaging with nanosecond electron pulses were investigated. The image quality is generally limited by the noise on the camera and by lens errors (aberrations and astigmatism). In single-shot imaging the signal intensity is an even more important stake than in stroboscopic operation, because it can not be compensated by a longer acquisition time. Therefore, the loss within the microscope column has to be minimized. One important aspect is the removal of the condenser aperture. Furthermore, the lens current of the condenser lens (CL3) has been increased. This way the sample is no longer illuminated by a parallel electron beam as it is used in conventional electron microscopy, but the beam is focused onto the sample. These steps drastically increase the number of electrons reaching the detector, but compromise on the beam quality, e.g. in terms of coherence and aberration induced errors.

It has to be noted, that the setup is not yet fully optimized. Work will be continued on the quality of the UV laser profile, the quality of the cathode surface and the length of the UV pulse.

To determine the image resolution, one method is to look for the smallest particles observable in the image. This requires the calibration from a reference image taken in thermionic mode. Another method is the so-called edge resolution, [54] where the blurred edges of larger particles are measured. This way, a better comparison within image series is achieved.

Multi-Shot Studies

In a first set of experiments the contribution of lens errors on the image resolution was studied. In order to outmaneuver shot noise, the images were integrated over a large number of pulses. The image resolution was tested on a sample of gold nanoparticles with various sizes.

Chromatic Aberration

Images were taken for different UV laser pulse energies (equivalent to the number of electrons per pulse) and various bias voltages applied on the Wehnelt cone. The possible range of the laser energy goes from a minimum, where all signal is lost in shot noise of the detector, to a maximum when ablation of the cathode surface appears. In this study, the UV energy range was chosen as follows: the lowest UV energy yields

reasonable low-signal images, the highest energy was set just below the ablation limit. The condenser lens was kept at a constant voltage for parallel illumination. A selection of the image series is presented in figure 5.4, the complete data set can be found in the appendix C on page 105.
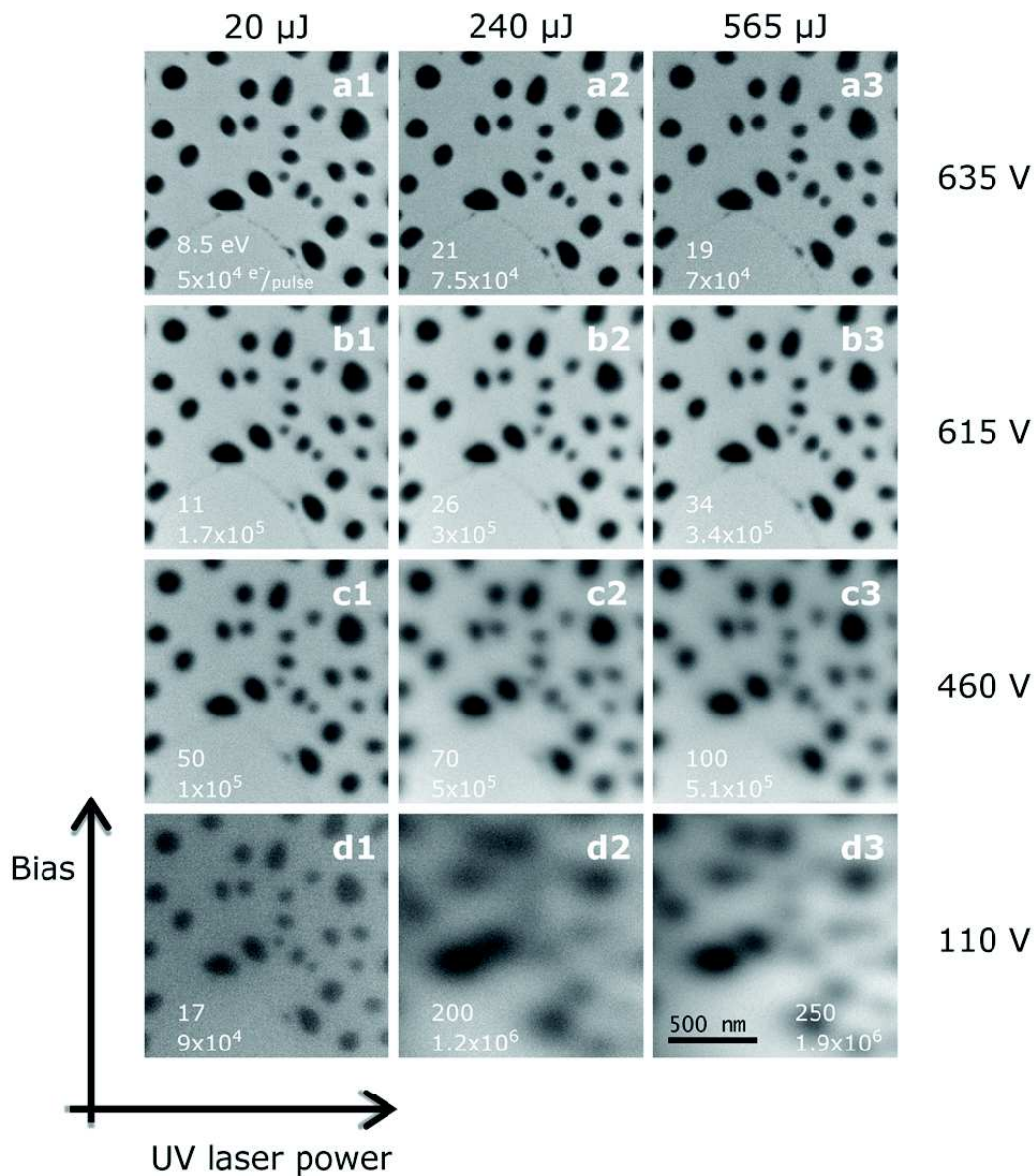

Figure 5.4: *Spatial resolution trends in imaging with ns-electron pulses. The UV laser pulse energy and Wehnelt bias were varied. As emitter a tantalum disc was used at a distance of 550 µm to the Wehnelt aperture. The energy width of accompanying EELS measurements is noted at the bottom of every image, together with the number of electrons per pulse. The shot noise limitation was excluded by integration over 2000 pulses.*

Images in the lowest row (d1-3) correspond to the minimum bias voltage on the Wehnelt cone. Upwards, the bias is increased, the exact values are noted on the right hand side. Row b corresponds to the "saturated" filament where the halo (comprising off-axis electrons) has appeared and merges with the central emission; the intensity shows a peak. The topmost row corresponds to an oversaturated filament. Here, the further increased bias voltage homogenizes the beam, but reduces the singal. A detailed description of the electron emission can be found in section 4.4.2 on page 39. The UV intensity was increased form the left to the right, the pulse energy is noted above each column.

The best result is obtained at lowest UV energy and highest Wehnelt bias (a1). With increasing laser energy and especially with decreasing bias voltage the images become blurry and small particles can no longer be resolved.

EELS measurements carried out in parallel for all images, show a quite narrow energy distribution of 8.5 eV (FWHM of the zero-loss peak) for the best image of this series (a1), whereas the other images were taken with electrons of several tens of electronvolts, and even hundreds of electronvolts for the images d2 and d3.

The trends seen here are similar to what was observed for picosecond electron pulses in stroboscopic UTEM, suggesting the same phenomena as evoked in the detailed study in chapter 4. The UV laser energy drives the number of electrons emitted per pulse. This changes the charge density and thus the Coulomb interactions within the electron packet. Higher laser pulse energy results in a lateral beam broadening and an enlarged energy spread, which increases the influence of chromatic aberration. Both factors reduce the spatial resolution. As shown before, the Wehnelt bias significantly impacts the energy distribution through chromatic filtering. This filtering is more efficient at a high bias as the gun cross-over is sharper and the beam is further expanded above the critical aperture.

In general, it can be stated that chromatic aberration is a huge issue for nanosecond imaging. Beam coherence is evidently poor, all contrast arises from scattering contrast. But the blurring in this set of images proves chromatic aberration far more important.

Spherical Aberration

As stated before, conventional electron microscopy uses parallel illumination for optimum imaging conditions. By focusing the electron beam onto the sample, the number of electrons can be increased dramatically, which is in favor of single-shot imaging where the main difficulty is signal intensity. The influence on the image quality and the spatial resolution is shown in figure 5.5. The low UV pulse energy of 20 µJ was kept for this study, the Wehnelt bias was set at the intensity peak (saturation, where the small halo and the central spot are merging), the images were integrated over 400 pulses. In the left image the beam is completely focused, towards the right the beam is spread by changing the lens current of the condenser aperture CL3 (two and three steps respectively in coarse setting).
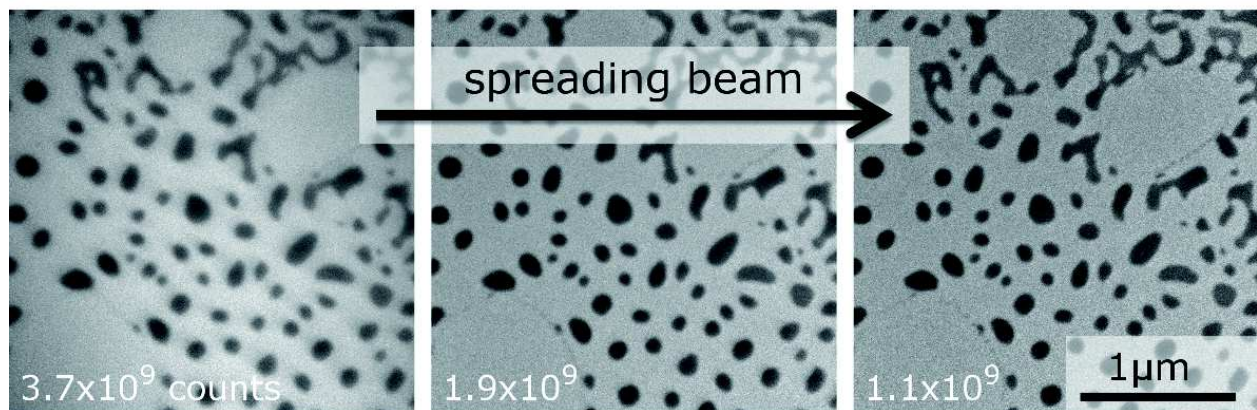

Figure 5.5: *Influence of the electron beam spread on the spatial resolution in imaging with ns-electron pulses. A UV pulse energy of 20 µJ was used with a cathode-Wehnelt gap of 550 µm and a bias of 500 V to achieve the intensity peak near the saturation. The number of counts on the detector is noted on each image. The images were integrated over 400 pulses.*

The left image taken with a focused electron beam shows blurry nanoparticles. As the beam is spread the particles become sharper. Yet, even the right image is still slightly blurry. The same experiment with thermionic electron emission gives a blurry image with the focused beam, but as soon as the the beam is spread, the nanoparticles are sharp. The images taken in thermionic mode can be found in the appendix C on page 106.

Having the same effect with the focused thermionic and photoelectron beam clearly states that the underlying phenomenon is caused by spherical aberration of the objective lens. Chromatic aberration would not be visible in thermionic mode, as the energy distribution is narrow in that case.

In conclusion, this image series shows that spherical aberration has to be considered when trading off resolution and signal intensity for single-shot operation.

Ultimate Resolution

The ultimate resolution achievable with the beam quality of nanosecond electron pulses and the lens errors intrinsic to the microscope can be estimated from an image showing small particles closely together. Figure 5.6 was taken at the same conditions as the image a1 in figure 5.4, being low UV pulse energy, high bias voltage and a parallel illumination of the sample. The image was integrated over 2000 pulses to outrun shot noise.
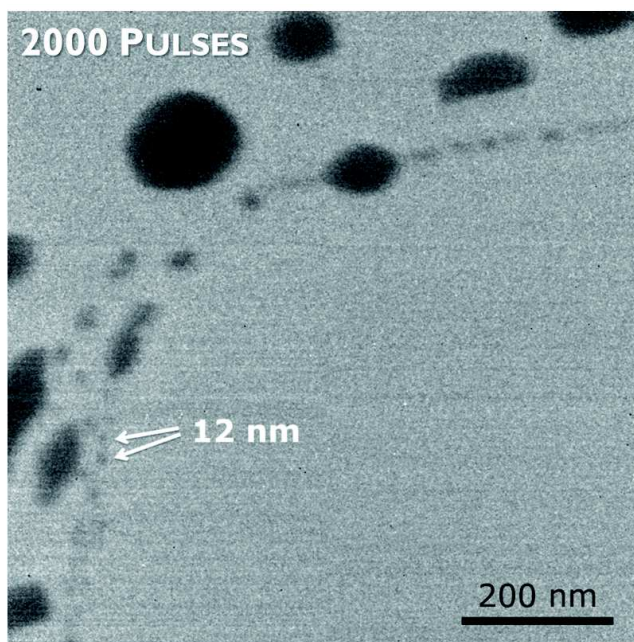
Figure 5.6: *Spatial resolution test using ultimate beam quality of ns-electron pulses in terms of coherence and aberration effects. $\Delta E = 8.5$ eV. Shot-noise was excluded by integration over 2000 pulses.*

Two particles with a diameter of 12 nm are visible in this image (calibrated from a reference image taken in thermionic mode).

Single-Shot Imaging

For real single-shot imaging using one unique electron pulse a compromise has to be found between chromatic, spherical aberration and signal intensity. In figure 5.7 the upper row shows images integrated over 100 pulses, the lower row contains images taken with one unique ns-pulse. The bias is increased from left to right. Note that these images are taken with the non-optimized setup; an improved image resolution is expected upon increased signal intensity.
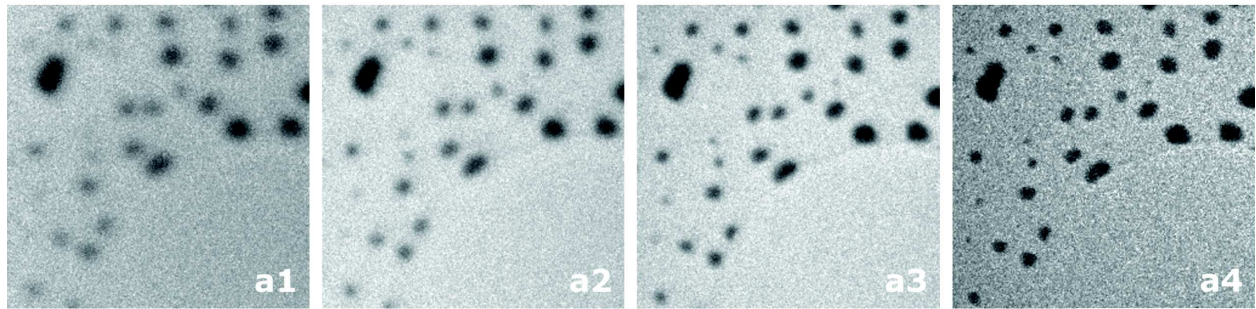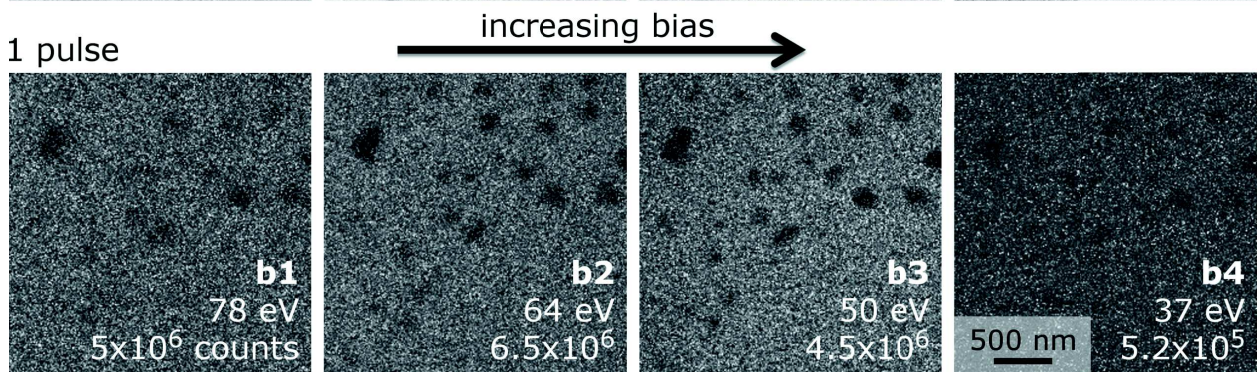

Figure 5.7: *Images taken at different Wehnelt bias voltages, integrated over 100 pulses (upper row) and single-shot images (lower row). The best compromise between chromatic aberration and signal intensity for single-shot imaging is at saturated emission (b3). A UV pulse energy of 20 µJ was used with a cathode-Wehnelt gap of 550 µm. Image size 250 × 250 px, the number of counts and the energy distribution are noted on each image.*

In the upper row the sharpness of the gold nanoparticles improves from left to right with increasing bias voltage, in accordance with figure 5.4. In terms of signal intensity, a2 and a3 are the brightest, corresponding to the appearance of the halo and the merged emission pattern respectively.

The single-shot images shown in the lower row are very noisy in general. At low bias (b1) the blurry nanoparticles are hardly distinguishable from the background. The image quality improves for b2 and b3 as the signal intensity increases together with the sharpness of the image. In the last image (b4) the low signal is completely lost in shot noise. The best image of this series is b3, where nanoparticles of a diameter of 50 nm can be resolved.

The image series demonstrates that spherical and chromatic aberrations have to be traded off with signal intensity for single-shot imaging. The best compromise is at the intensity peak where the filament image is "saturated" (central emission and halo are merging). The bias voltage has to be finely tuned, in order to achieve the lowest blur possible, just before the signal drops.

In contrast to stroboscopic operation with picosecond electron pulses, the different trajectories of the two

electron populations merged in saturated emission does not matter here, as a temporal difference of 100 ps is irrelevant for electron pules of a duration of several nanoseconds.

Best Resolution after Latest Improvements

The latest improvement was achieved by an elongation of the UV laser pulse. For this purpose, the UV laser beam was split in two and recombined after retarding one beam in such a way that the first pulse of one beam is immediately followed by the second one of the other beam path. Hereby, the pulse length is doubled and the electron density reduced approximately by a factor of two.

This pulse elongation significantly improved the image quality. Figure 5.8 shows the best single-shot image before and after filtering.

(a) *Single-shot image.*   (b) *Filtered single-shot image.*
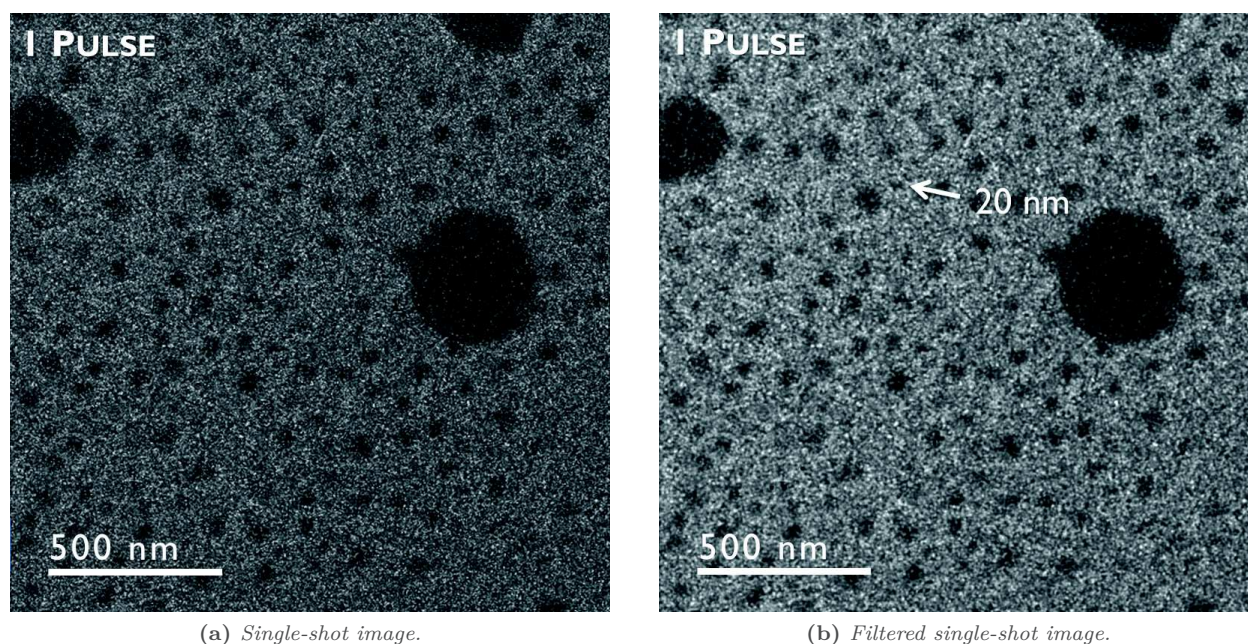
Figure 5.8: *Best single-shot image at the present day, taken with an elongated UV laser pulse by a factor of two. UV pulse energy 400 µJ, gap 570 µm, Wehnelt bias 670 V: slightly undersaturated emission (central emission and off-axis halo present), no condenser aperture, converged beam. Convergence angle $\alpha = 45$ mrad, $\Delta E = 35$ eV, 10^6 electrons per pulse. The image was filtered using Marr-Hildreth (sigma 0.391).*

The smallest particles visible in these images have a diameter of 20 nm. This is an improved image resolution by a factor of 2.5 compared to the previously used fundamental UV pulse length. Measuring the edge resolution yields 25 nm.

Excluding shot noise, the ultimate multi-shot resolution achievable with this improved setup is shown in figure 5.9. The image was integrated over 1000 pulses.

The image shows smallest particles with a diameter of 6 nm. This corresponds to an improvement by a factor of two. The edge resolution in this image is 5 nm.
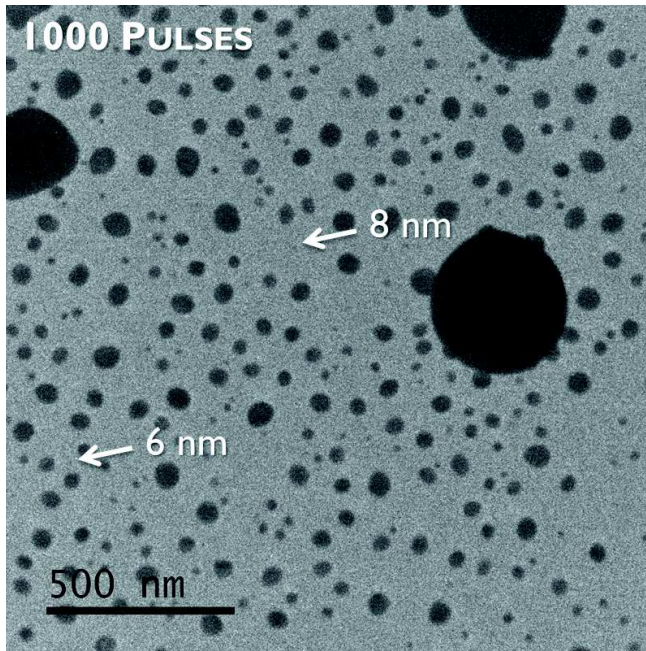
Figure 5.9: *Ultimate multi-shot resolution at the present day, upon integration over 1000 pulses to exclude shot-noise. UV pulse energy 400 µJ, gap 570 µm, Wehnelt bias 720 V: saturated emission (central emission and off-axis halo merged), no condenser aperture. Convergence angle $\alpha = 25$ mrad, $\Delta E = 25$ eV, 10^5 electrons per pulse.*

Theoretical considerations and approximations

The experimentally obtained image resolution can be compared to several instrumental limitations. In particular, these are aberration effects of the objective lens and shot noise on the detector.

The latter can be approximated by the Rose criterion, which states that the noise has to be inferior or equal to the contrast divided by the number of gray scale levels. [50] The shot noise is defined as $N^{-1/2}$ where N is the number of electrons per pixel. Standard values found in the literature (contrast of 0.5, 5 gray levels) [51] yield a shot noise of 0.1 and thus a minimum of 100 electrons per pixel.

The singe-shot image (figure 5.8) was formed by 10^6 electrons. Consequently, a maximum of 10^4 pixels (100×100 px) could be irradiated with 100 electrons each. Related to the illuminated specimen area of 1.7 µm $\times$ 1.7 µm, the pixel size is 1.7 µm / 100 = 17 nm. This is the noise-limited resolution r_{SN}.

The ultimate resolution image contains a total of 10^8 electrons, resulting in a noise-limited resolution of $r_{SN} = 1.7$ nm.

The other limitation originates in the lens system, especially the objective lens. Here, chromatic aberration and spherical aberration contribute. In general, the effects are small and only play a role in high resolution TEM. However, the UTEM works with energy distributions up to two orders of magnitude broader than in

conventional TEM and furthermore uses a convergent electron beam. Therefore, chromatic and spherical aberration are relevant even at lower magnification.

The following expression can be applied to approximate the resolution limit induced by chromatic aberration:

$$r_{chr} = C_C \cdot \alpha \cdot \frac{\Delta E}{E_0} \tag{5.4}$$

with α: convergence semi-angle and C_C: chromatic aberration.
Adapted from [78].

The convergence angle was calculated from convergent-beam electron diffraction measurements (CBED), and found to be 45 mrad in the conditions used for the single-shot image. With the C_C of the JEOL 2100 microscope of 1.4 mm, $\Delta E = 35$ eV and $E_0 = 200$ keV a resolution limit of $r_{chr} = 11$ nm can be expected due to chromatic aberration of the objective lens. For the ultimate image with $\alpha = 25$ mrad and $\Delta E = 25$ eV a resolution limit of $r_{chr} = 4.4$ nm is obtained.

The contribution of the spherical aberration of the objective lens can be approximated by:

$$r_{sph} = 0.25 \cdot C_S \cdot \alpha^3 \tag{5.5}$$

with C_S: spherical aberration. Adapted from [79].

With a C_S of 1.0 mm the resolution limit due to spherical aberration of the objective lens is $r_{sph} = 23$ nm in the case of the single-shot image and $r_{sph} = 3.9$ nm for the ultimate image.

The total resolution limit due to aberrations and shot noise can be calculated as:

$$r = \sqrt{r_{chr}^2 + r_{sph}^2 + r_{SN}^2} \tag{5.6}$$

For the single-shot image a total resolution limit of 31 nm is obtained, the case of the ultimate resolution image yields a total resolution limit of 6.1 nm. These values are in very good agreement with the measured edge resolution of 25 nm and 5 nm respectively. The experimentally obtained image resolution can thus be explained by a combination of shot noise and aberration effects of the objective lens.

5.3.2   Electron Diffraction

Another technique widely used in materials sciences is electron diffraction. In general, the quality of electron diffraction patterns (DP) is limited by the sample itself (crystallinity, thickness etc.) and by the electron beam coherence provided through the instrument. Here, the instrumental parameters are quite poor compared to conventional TEMs, as a large disc-shaped cathode is used, as well as electron pulses containing a wide energy spread.

Several instrumental parameters can be adapted though to optimize electron diffraction. First, there is the Wehnelt bias voltage. As discussed before, this acts on the chromatic filtering and thus the resulting energy distribution, but also changes the source (size of the gun cross-over and especially the divergence angle). Second, diaphragms can be inserted. By sheltering outer electrons, the energy width can be reduced, at the same time spatial beam coherence improves. A smaller beam diameter produces less error on subsequent lenses due to spherical aberration. And third, the condenser lenses can be adapted to reduce the convergence angle and optimize parallel illumination.

A test sample has been used to evaluate the capability of this nanosecond UTEM with respect to electron diffraction. The test sample is an ultrathin silicon single crystal, in order to exclude sample limitations.

Multi-Shot Studies

In the following, the influence of chromatic aberration is presented. In order to outmaneuver shot noise, the following diffraction patterns were integrated over 100 pulses.

Figure 5.10 shows DPs taken at different Wehnelt bias settings. From left to right the bias voltage was increased, resulting in a reduced energy distribution (values noted at the top of each DP). All other settings were kept constant. It is important to mention, that all bias settings are below saturation, in order to work exclusively with the central on-axis electrons. The apparition of the halo in the emission pattern would be reproduced in every diffraction spot.
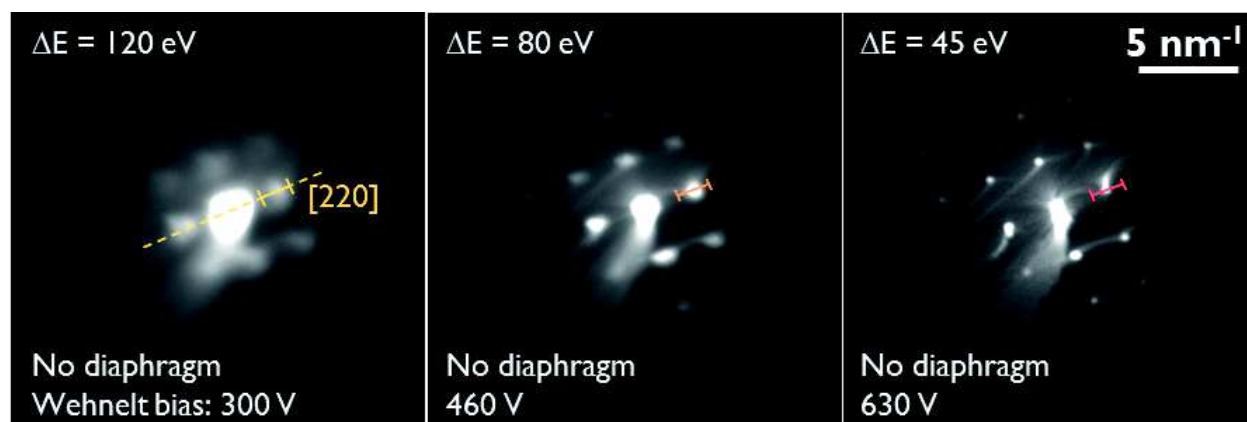
Figure 5.10: *Effect of chromatic aberration: Electron diffraction patterns of monocrystalline Si obtained at different Wehnelt bias voltages, changing the energy distribution of the beam. UV pulse energy 85 μJ, cathode-Wehnelt gap 570 μm, CL0-lens 23.3 V, spotsize 3, alpha 3, no diaphragms inserted. Integration over 100 pulses.*

The left diffraction pattern is very blurry, but diffraction spots are clearly visible. With increasing Wehnelt bias the spots become sharper and smaller. In order to quantify the quality of these diffraction patterns, profiles have been taken according to the dotted, yellow line depicted in the left pattern. The diffraction spot [220] was normalized, profiles of all DPs are displayed in figure 5.11. The full width at half maximum (FWHM) represents the diameter of the diffraction spot. The smaller this value, the better is the quality of the diffraction pattern. The FWHM shrinks with increasing Wehnelt bias.

The diameters of the diffraction spots (FWHM) can be compared to the energy spread, which was measured for each diffraction pattern. According to the Bragg law (eqn. 5.7) the wavelength and thus the electron energy defines the diffraction angle. In consequence, a distribution in electron energy results in a distribution of the diffraction angle.

$$\sin(\theta) = \frac{\lambda}{2d_{hkl}} = \frac{hc}{2d_{hkl}E} \tag{5.7}$$

Bragg law, with θ: diffraction angle, λ: wavelenth, d_{hkl}: interplanar spacing of the planes [hkl],
h: Planck's constant (6.626×10^{-34} Js), c: speed of light.

For the [220] plane with $d_{220} = 1.9194$ Å the angular distributions were calculated for the different ΔE, which were measured for each diffraction pattern. The results are presented in table 5.4.
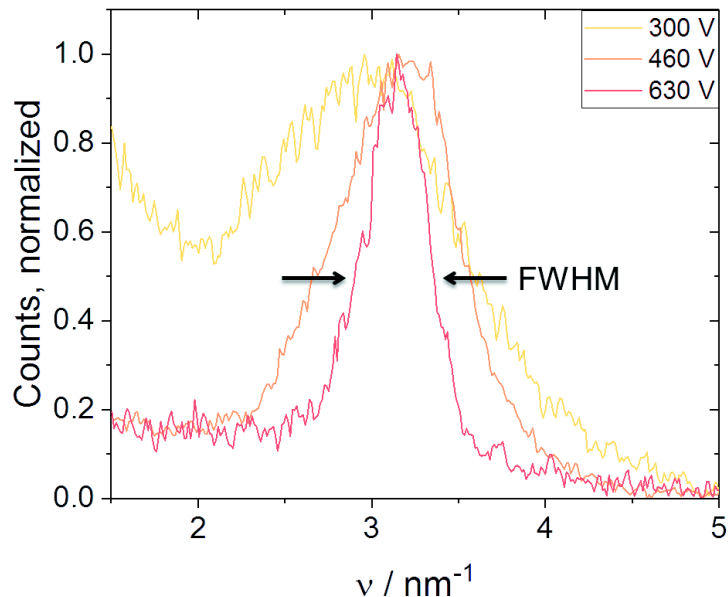
Figure 5.11: *Normalized profiles of the electron diffraction patterns of figure 5.10, taken through the [220] spot along the yellow line. The indicated FWHM describes the diameter of this diffraction spot.*

Table 5.4: *Angular distribution caused by the Bragg law for different energy distributions upon diffraction from the [220]-planes.*

Bias / V	ΔE / eV	$\Delta\theta$ / µrad
300	120	9.7
460	80	6.5
630	45	3.6

Table 5.5 shows the conversion of the diameter (FWHM) of the diffraction spots into an angular distribution.

Table 5.5: *Angular distribution related to the diameter of the diffraction spot (FWHM).*

Bias / V	FWHM / nm^{-1}	$\Delta\theta$ / µrad
300	1.48	7.9×10^3
460	0.89	4.6×10^3
630	0.46	2.5×10^3

Comparing both tables, the trends are the same showing lower $\Delta\theta$ with increasing Wehnelt bias. However, a difference of three orders of magnitude appears. Consequently, the angular distribution resulting from the Bragg law is not the dominating factor for the large diffraction spots observed in figure 5.10. Other effects can be suggested: As demonstrated in imaging with nanosecond electron pulses, chromatic aberration is a huge issue. Different focal lengths depending on the electron energy will cause a blurring of the diffraction spots and thus an increase of the FWHM. The impact of chromatic aberration is evidently reduced for a lower energy distribution, which is in accordance to the measured diameters.

In addition, all apertures have been retracted, a large spotsize and alpha-setting have been used in order to see a pronounced impact of the Wehnelt bias. This implies a large convergence angle. The size of the virtual source and the convergence angle vary at changing Wehnelt bias. Therefore, this series might not exclusively show the effect of chromatic aberration, but a mixed effect with the reduced convergence angle.

A second set of diffraction patterns was taken at constant Wehnelt bias (630 V). The condenser aperture was inserted into the beam path, spotsize and alpha-setting were reduced in a subsequent step. The diffraction patterns and the extracted profiles of the [220] diffraction spot are shown in figure 5.12. For comparison, the profile of the above shown DP at 630 V without further filtering was included into the graph (red curve).
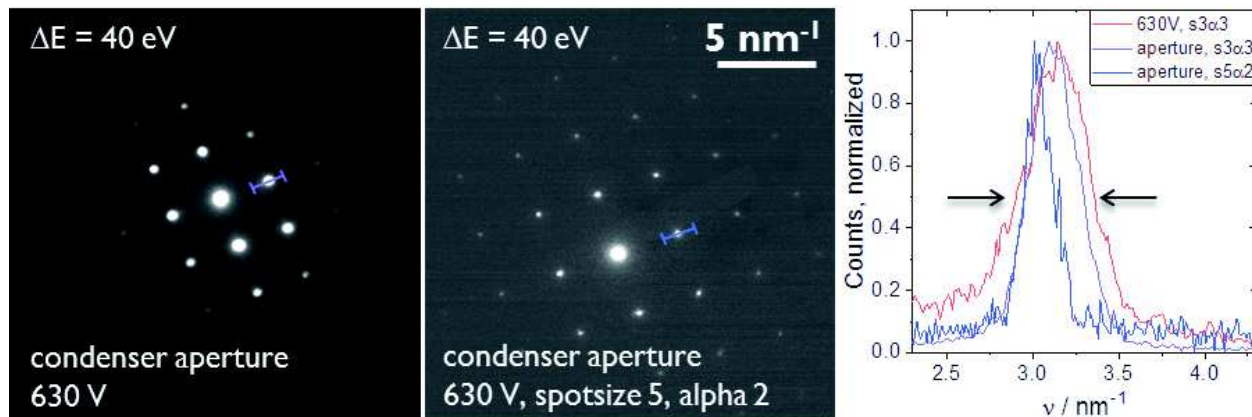

Figure 5.12: *Effect of spherical aberration: Electron diffraction patterns with various filtering by the condenser aperture, spotsize and convergence angle of monocrystalline Si. Constant Wehnelt bias of 600 V. UV pulse energy 85 µJ, cathode-Wehnelt gap 570 textmum, CL0-lens 23.3 V, (spotsize 3, alpha 3). Integration over 100 pulses.*

Looking at the diffraction patterns, the insertion of the condenser aperture removed the blur in between the diffraction spots (in comparison to the DPs shown above in fig. 5.10). The size of the diffraction spots can be judged looking at the profiles. The FWHM is reduced by each filtering step, yielding 0.34 and 0.18 nm^{-1} respectively.

This second series primarily demonstrates the trivial influence of the convergence angle on the quality of diffraction patterns. However, a closer look reveals that the insertion of the condenser aperture slightly improved the energy distribution and thus also reduced the effect of chromatic aberration.

Single-Shot Electron Diffraction

The conditions for real single-shot electron diffraction need to present a compromise between signal and energy width (effect of chromatic aberration). The single-shot diffraction pattern shown in figure 5.13 was taken with the newly optimized setup using an elongated laser pulse. The increased beam intensity allowed a strong filtering. A high bias was applied, the condenser aperture was inserted, spotsize and alpha were set to minimize the convergence angle.

This diffraction pattern demonstrates the feasibility of single-shot electron diffraction on this instrument, a complementary method to imaging widely used in materials sciences.
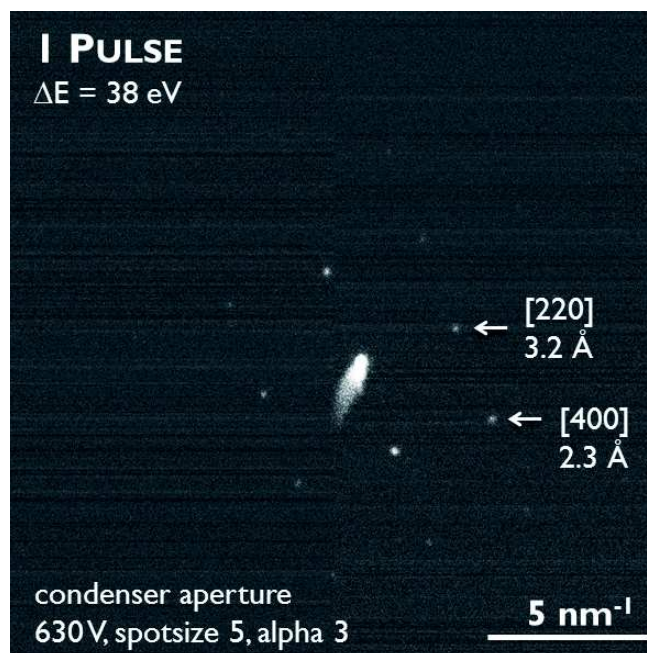
Figure 5.13: *Best electron diffraction pattern of a Si monocrystal with one single ns-electron pulse, taken with an elongated UV laser pulse by a factor of 2. UV pulse energy 450 µJ, cathode-Wehnelt gap 570 µm, Wehnelt bias 630 V, CL0-lens 22.7 V.*

5.3.3 Electron Energy Loss Spectroscopy

The nanosecond TEM in Strasbourg is the first single-shot setup worldwide which is equipped with an electron energy loss spectrometer. This opens research to a new domain of nanosecond experiments, speculated in the past to be too challenging to yield meaningful results. [29]

The study presented above on ns-imaging underlines the importance of understanding how the energy distribution evolves within nanosecond electron pulses. This enables the user to minimize chromatic aberration and significantly improve spatial resolution. The study furthermore shows the limitation of imaging and the impossibility to analyze materials transformations at the atomic scale. Diffraction contrast is too weak and the scattering contrast can not reveal these details. Spectroscopy, on the contrary, can potentially explore the chemical composition, structure and environment and thus enable nanosecond TEM to probe irreversible sample transformations at the atomic scale.

To begin with, figure 5.14a shows single-shot electron energy loss spectra generated with a medium UV pulse energy. The shape of the zero-loss region varies greatly between individual pulses. Figure 5.14b shows a spectrum integrated over 100 pulses, where an average energy distribution of 500 eV (FWHM) can be determined.

The large variations of the individual pulses can be related to unavoidable laser instabilities, which result from the complex and sensitive components for the fifth harmonic generation. Slight differences in the pulse profile result non-uniform photoemission which propagates through changed Coulomb interactions. The outcome are individually shaped EEL spectra. The operator can observe the same phenomenon by focusing the beam at the viewing screen. The shape of each pulse changes as blurry fluctuations around the optical axis. However, this does not prevent single-shot studies as these fluctuations can be removed by filtering.
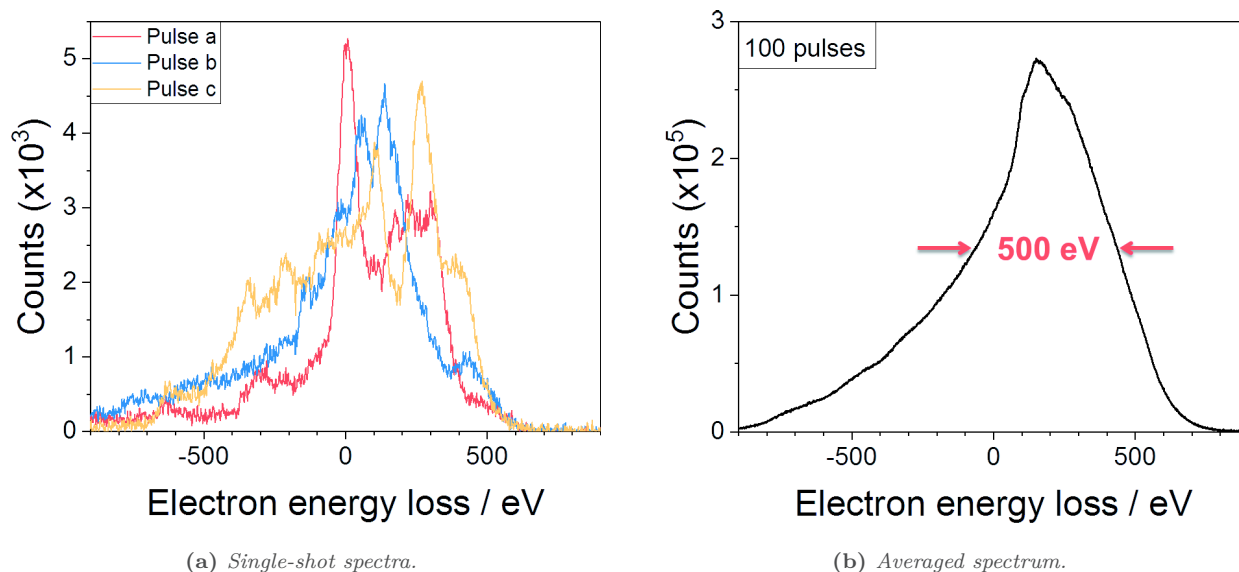
(a) *Single-shot spectra.*

(b) *Averaged spectrum.*

Figure 5.14: *Nanosecond electron energy loss spectra taken at minimum Wehnelt bias and medium UV pulse energies of 85 μJ. The spectra of single pulses (a) vary hugely. Averaging over 100 pulses (b) results in an broad energy distribution of 500 eV FWHM.*

Making use of the trends understood in previously demonstrated studies, the electron pulse can be refined and the energy width can be reduced. This is done firstly by an increased Wehnelt bias to perform chromatic filtering, and secondly by lowering the UV laser energy to reduce energy broadening in general. The ultimate result can be seen in figure 5.15.
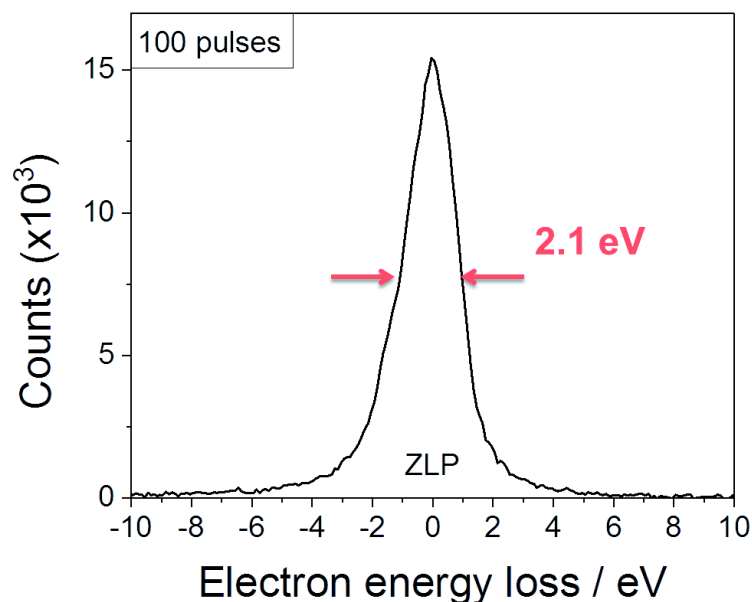
Figure 5.15: *EEL spectrum showing the ultimate energy width of nanosecond electron pulses, taken at maximum Wehnelt bias and 5 μJ laser pulse energy. The spectrum was integrated over 100 pulses.*

The zero-loss peak, integrated over one hundred pulses, shows an energy width of 2.1 eV (FWHM). The value is very close to the theoretical limit of 1.7 eV, which results from the initial kinetic energy. This demonstrates for the first time that narrow energy distributions can be achieved with intense ns-electron pulses, a fact which has been counter-argued until now.

However, the signal intensity is too weak for any single-shot application, neither EELS nor diffraction or real space imaging (600 electrons per pulse). As always, a compromise has to be found. Figure 5.16 shows EEL spectra which could be recorded under optimized conditions using an elongated electron pulse (14 ns). The core-loss region shows a distinct carbon K edge from a carbon nanotube sample and a nickel L edge from a nickel film. An energy width of 30 eV and 60 eV respectively has been used.

(a) *Single-shot carbon K edge.*   **(b)** *Single-shot nickel L edge.*
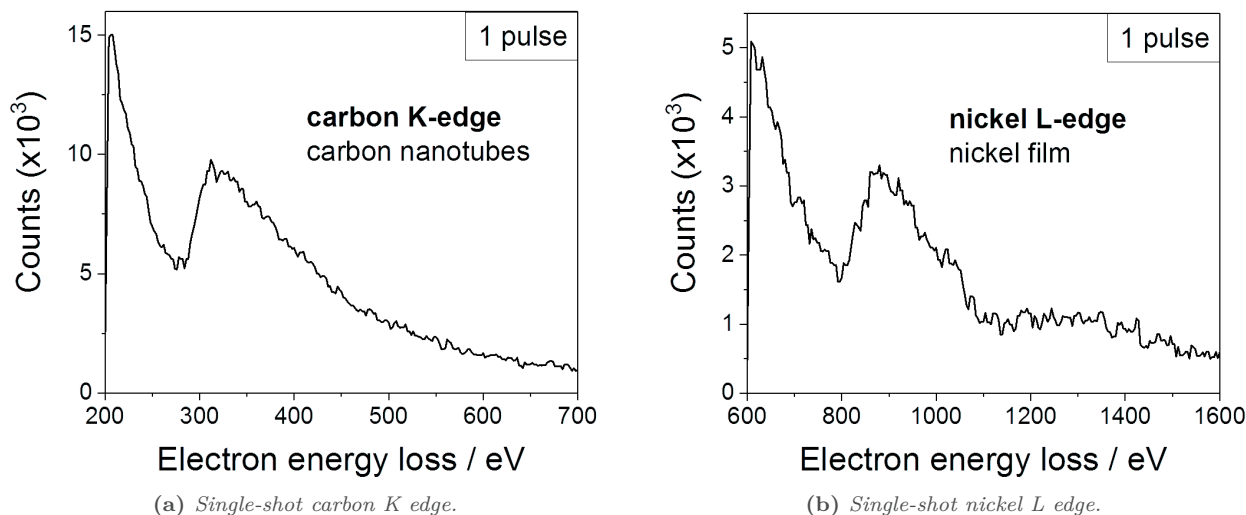
Figure 5.16: *Core-loss EEL spectra taken with one single electron pulse of 14 ns. (a) Carbon K edge of carbon nanotubes taken with $\Delta E = 30$ eV and 5×10^6 electrons/pulse (UV pulse energy 200 µJ, Wehnelt bias 665 V). (b) Nickel L edge of a nickel film taken with $\Delta E = 60$ eV and 5×10^7 electrons/pulse (UV pulse energy 450 µJ, Wehnelt bias 560 V). Cathode-Wehnelt gap 570 µm. The spectra were smoothened by averaging over 4 eV.*

The fine structure is not resolved in these spectra, but the K and L edges are unequivocally visible. These are the first core-loss EEL spectrum ever taken with one unique nanosecond electron pulse. It is a very promising result, as it proves the feasibility of chemical tracing of irreversible material transformations. Evidently, a ZLP of several tens of electronvolts can not resolve the fine structure. Nevertheless, the appearance or disappearance of characteristic peaks in the core-loss region allows to follow chemical reactions such as oxidation processes and to investigate their reaction speed at the nanoscale. This result is a world novelty.

5.4   Nanosecond Electron Pulse Dynamics

The big difference between the stroboscopic and single-shot setup in terms of their electron pulse dynamics is the fact that no significant temporal broadening occurs within nanosecond pulses. In stroboscopic operation it is crucial to understand the workable parameter space, which turned out to be limited by the explosion of the pulse length at a certain Wehnelt bias threshold. The particular importance arises from the fact that temporal resolution can not be monitored during experimental work. For single-shot TEM, which is operating with three orders of magnitude longer electron pulses, there is no such limit. In fact, the critical parameter space is reduced to two main variables being the energy spread and the signal intensity. Both can directly be measured when the materials science sample is inserted, in contrast to the stroboscopic operation mode, where the temporal resolution is a critical but "invisible" value which can only be determined with a particular test sample. Thus, in nanosecond operation it would even be feasible to look at the resolution and adapt it by pure trial and error before launching the time-resolved experiment.

Nevertheless, a guideline which clarifies the effect of instrumental parameters is helpful to a assure quick and target-oriented optimization. Especially, as there is not one perfect setting for all working methods presented previously. Furthermore, it is interesting to compare nanosecond pulse dynamics to those found for picosecond electron pulses.

A systematic study was carried out, where the influence of the gap between cathode and Wehnelt aperture, the Wehnelt bias voltage and the UV laser pulse energy have been varied. The energy distribution and the signal intensity were measured, the latter was converted to a number of electrons per pulse. For intense beams the current density on the small viewing screen was used, multiplied by the area and the conversion of the current to the number of electrons. Weak electron beams are below the detection limit of the viewing screen. These were quantified by the counts on the CCD camera, scaled by the sensitivity of the detector and a factor which takes into account the fraction of the beam blocked by the entrance aperture of the camera. Figure 5.17 shows a series of measurements taken at constant UV pulse energy. The energy distribution and the number of electrons per pulse are displayed as a function of the Wehnelt bias. Series were taken at different cathode-Wehnelt gaps (color-coded).

As described in detail throughout the investigation of the stroboscopic mode, the bias range depends on the distance between cathode and Wehnelt aperture. The higher the gap, the shorter is the workable range before the extinction of the beam, as the electrons have to combat the electrostatic potential on a longer path before exiting the Wehnelt cone. Thus, they are already blocked inside the Wehnelt at a lower voltage.
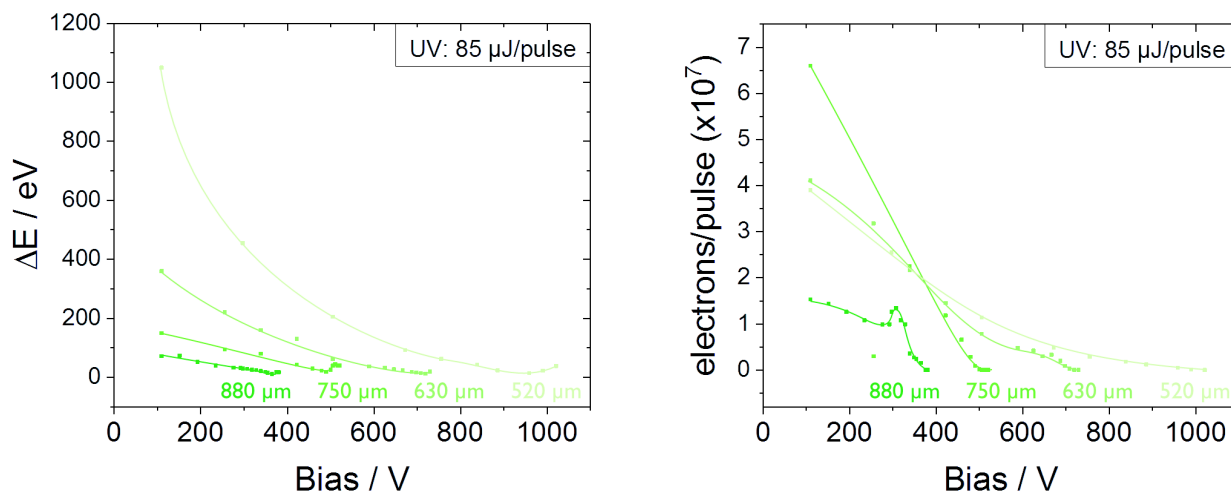
(a) *Evolution of the energy distribution.*

(b) *Evolution of the number of electrons per pulse reaching the detector.*

Figure 5.17: *Evolution of the electron beam characteristics as a function of the Wehnelt bias. An intermediate UV pulse energy of 85 μJ was used; measurements were recorded for different cathode-Wehnelt gaps (color-coded). A guide to the eye is drawn between the individual data points.*

For any cathode-Wehnelt gap the energy spread decreases with increasing bias voltage and rebounds slightly before the extinction of the beam. The rebound appears when the small off-axis halo merges with the central emission. The shortest Wehnelt gap produces the highest energy distributions measured at the spectrometer. Similarly, the number of electrons per pulse also decreases with increasing bias (figure 5.17b). Here however, the trends are less consistent. At the largest gap of 880 μm a pronounced peak appears at 300 V when the halo emerges. Among the other curves, only the gap of 630 μm shows a shoulder upon the emergence of

the halo, at the other gaps no feature is visible at the corresponding Wehnelt bias. Another peculiarity is the high number of electrons per pulse for the second largest gap. Yet, one of the few measurements at low voltage is an outlier (at 250 V). This curve taken at 750 µm might therefore not be very representative and reproducible.

As a general trend the bias voltage simultaneously reduces the energy distribution and the number of electrons per pulse. This concurs with the trend observed in stroboscopic operation. The same underlying phenomenon can be assumed, which is a chromatic filtering after the chromatic dispersion induced by the aberrations of the Wehnelt electrode.

A combination of both graphs helps to find the best compromise between energy spread and signal intensity, the two main parameters which need to be traded off. Figure 5.18 displays the number of electrons per pulse as a function of the energy width, using a bi-logarithmic scale.

The nonlinear interplay between energy spread and signal intensity is nicely visible in this graph. Tracking the curves from low to high bias means starting at the upper right corner and moving to the left and downwards. In a first low-bias regime ΔE and the number of electrons both decrease. After a *turning point*, the number of electrons shrinks further, whereas the energy spread rises again. Comparing the different cathode-Wehnelt gaps, for a given energy distribution large gaps yield the highest number of electrons on the detector. Or the other way round, for a given signal intensity a large cathode-Wehnelt gap achieves the lowest energy distribution.
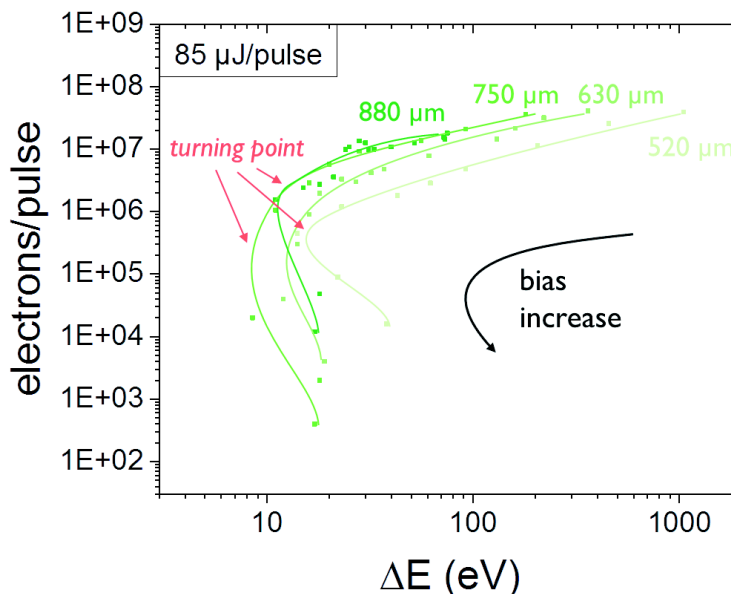
Figure 5.18: *Evolution of the pulse characteristics displayed as signal (number of electrons per pulse reaching the detector) versus energy spread, for varying Wehnelt bias voltages. A UV pulse energy of 85 µJ was used.*

Further data sets were recorded at four other UV pulse energies. All plots can all be found in the appendix D on page 107. Figure 5.19 regroups all measurements by their cathode-Wehnelt gap. This provides a user-oriented assembly, because in general the Wehnelt gap is fixed in advance and optimization is done using the other parameters (UV laser energy and Wehnelt bias). The laser energies are color-coded in analogy to the electromagnetic spectrum in red to violet from low to high energy, the gap is represented by different shades of each color in the same way as above, having the lightest color for the shortest gap.
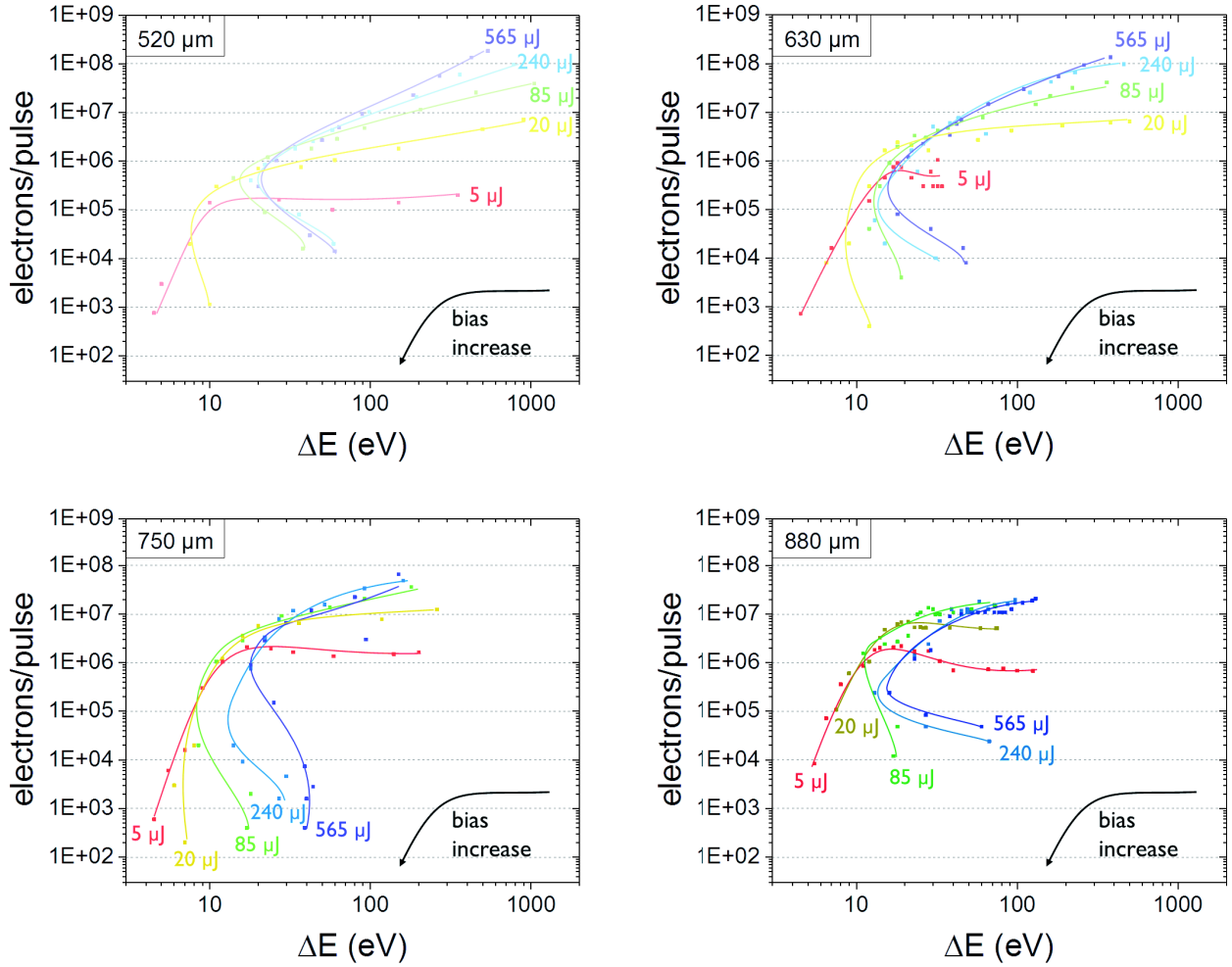
Figure 5.19: *Evolution of the main electron beam characteristics (number of electrons per pulse reaching the detector and energy distribution) for various UV laser pulse energies at different cathode-Wehnelt gaps.*

Comparing the four graphs, the accessible range of ΔE and the number of electrons are different depending on the cathode-Wehnelt gap. The maximum number of electrons reaching the detector decreases with increasing gap, about one order of magnitude between the shortest and largest gap. Furthermore, increasing the UV pulse energy has less influence on the maximum signal intensity for larger gaps. At 520 µm the curves of the different laser energies are well separated in the low-bias regime, as expected achieving higher signal for higher UV pulse energies. At 630 µm the curves of the two highest UV pulse energies are superimposed. For the two largest gaps also the medium UV energy of 85 µJ overlaps with the curves of higher laser energy in the low-bias regime. The larger the gap, the less room exists for pushing the maximum signal by increasing laser energy.

Regarding the energy distribution, an increasing gap reduces the maximum ΔE. With the smallest gap (520 µm) energy distributions up to 1000 eV can be reached, whereas the highest gap (880 µm) is limited below 200 eV. The combination of a lower signal and lower energy spread indicates a first filtering step through the distance between cathode and Wehnelt aperture. Most probably, the reason is that at high gap the electrons have to combat the potential barrier during along a larger distance, which is only possible for high energy electrons. This reduces the energy distribution of the electron pulse exciting the Wehnelt cone.

Coming back to the graph showing the shortest gap (520 µm), the curves of each UV energy show very different inclinations, both in the low-bias regime and in the high-bias regime after the turning point. In the regime of low bias (top right section of the graph), the slope decreases for decreasing laser energy. Interestingly, at 5 µJ the number of electrons stays constant while the energy spread changes.

Beyond the turning point, the behavior at high Wehnelt bias varies drastically depending on the UV pulse energy. For the weak laser pulses of 5 µJ the number of electrons per pulse drops quickly while the energy distribution is further reduced. Contrary, for higher laser pulse energy the ΔE rebounds and is enlarged even though the signal continues to decrease. This rebound is more pronounced for high laser pulse energies. In slightly different extents, these trends are consitent for any cathode-Wehnelt gap.

From an experimental point of view it is not mandatory to understand all evolutions in the presented graphs. It can suffice to use these graphs as reference in order to find workable conditions with the required trade-off between signal and energy spread. For this reasoning, no further work was put into an in-depth understanding of the pulse dynamics. However, some theoretical considerations can be discussed here.

The curve at lowest gap and lowest pulse energy of 5 µJ presents a particular case (light red curve). The plateau in the low bias regime, before the turning point, clearly states that chromatic filtering is not the only effect involved when the bias is increased. A second contribution seems to compensate the electrons lost through the filtering. The best guess is the collimation of the electron beam by the electrostatic Wehnelt lens, which focuses electrons emitted in a high angle onto the optical axis. At 5 µJ every lost electron through filtering is compensated by a newly collimated electron. Considering the curves taken at higher pulse energy, the chromatic filtering and the electron collection apparently act in a variable ratio. The underlying reason could be different initial energy spreads where the chromatic filtering is more or less efficient, and diverse emission profiles (angular distribution).

Beyond the turning point lies the high-bias regime. Starting again with the 5 µJ curve, the drop in intensity states that filtering is now dominating over a possibly happening electron collection. As the turning point approximately coincides with the appearance of the small halo, most emitted electrons are already focused onto the optical axis. A further increased lens strength is incapable of compensating the ongoing chromatic filtering.

With this picture in mind, the rebound of ΔE which is seen for all curves at higher laser pulse energy can be reconsidered. The rebound indicates that the chromatic filtering lost its efficiency. Apparently, the number of electrons per pulse decreases, so a filtering still takes place. However, the resulting part of the electrons possesses a higher energy distribution than at lower bias. One explanation could be an enhanced energy broadening after the chromatic dispersion and thus after the Wehnelt assembly - possibly in the gun cross-over. Another explanation might be an inhomogeneous energy spread as a function of the emission angle. High-angle electrons could have a larger energy dispersion which appears at high Wehnelt bias. Follow-up ray path simulations are certainly useful to understand this surprising behavior.

Regarding the application of the single-shot mode in materials sciences, the most important result of this parametric study is the knowledge about the rebound of ΔE at decreasing number of electrons per pulse, which has to be omitted. Furthermore, the existence of a turning point in every curve is a key finding as it represents a good trade-off between the two parameters. An increased cathode-Wehnelt gap generally shifts the turning point to higher numbers of electrons per pulse and slightly larger energy distributions. Regarding the laser pulse energy, the turning point is shifted to lower electron numbers with increasing laser

energy. This is better visible when the measurements are regrouped according to the laser pulse energy, the form of presentation which is shown in the appendix D on page 107.

For most applications, especially imaging and diffraction, a setting near the turning point should be used. In practice, compromises might be found on the low-bias regime, especially when the turning point does not provide enough signal. Guided by the data plots, the experimental conditions can quickly be optimized.

5.5 Summary

The work with intense nanosecond electron pulses implies great Coulomb interactions inside the pulse. Among them are inhomogeneous, statistical events. EEL spectra of individual pulses taken at minimum bias, i.e. lowest filtering, demonstrated energy spreads far above 500 eV and huge variations in the shape of the single-pulse spectra. These variations primarily result from unavoidable laser instabilities causing fluctuations in the pulse profile. The operator can observe the same phenomenon by focusing the beam at the viewing screen. The shape of each pulse changes as blurry fluctuations around the optical axis.

However, with accurate focusing and filtering of the beam it is possible to achieve electron pulses of sufficient quality and reproducibility for time-resolved single-shot experiments. Here, the in-depth understanding gained with the stroboscopic setup about electron beam dynamics and critical regions for Coulomb interactions are indispensable. An ultimate energy width as low as 2.1 eV could be presented at low laser pulse energy, high Wehnelt bias and with inserted apertures for best chromatic filtering. This value is close to the theoretical limit of $\Delta E_{kin} = 1.7$ eV.

A parametric study was carried out to investigate the main instrumental parameters (UV laser pulse energy, cathode-Wehnelt gap and Wehnelt bias voltage). The analysis of signal intensity versus energy spread shows a nonlinear correlation, revealing an optimum bias setting for high signal at a narrow energy distribution. This corresponds to the saturated emission, when central emission and the off-axis halo are merged. This setting represents the best compromise for single-shot imaging, where signal has to be traded off with image blurring. In addition to spherical aberration, the image blurring could also be related to chromatic aberration, a fact that has been widely discussed in the scientific community.

At present, the minimum particle size resolved in single-shot images were 20 nm in diameter. Nevertheless, spatial coherence would allow for better spatial resolution, at least a factor of 4, if shot noise was lower or signal was higher. The setup, still being in the process of optimization, is expected to yield higher signal in the near future and thus improve spatial resolution. Generally, all contrast in single-shot imaging arises from mass thickness, i.e. incoherent scattering contrast.

For electron diffraction other settings have to be chosen, as it is of utmost importance to work under uniform illumination conditions. Consequently, the contribution of a second electron population has to be omitted by working at lower bias voltages. The influence of chromatic aberration on diffraction patterns was demonstrated. The feasibility of single-shot electron diffraction on this instrument could be proved.

The most innovative contribution to the community of ultrafast electron microscopy is the demonstration that single-shot electron energy loss spectroscopy is possible. The proof of principle shows the carbon K edge of an amorphous carbon membrane. Even though the fine structure could not be resolved yet, this is a very promising result. The pure presence or disappearance of specific peaks in the core-loss region can be used to follow the dynamics of chemical reactions.

Conclusions

Studying dynamic processes at the nanoscale requires a high temporal resolution, which can only be provided by high-end instruments working in a pump-probe approach. This thesis presents an instrumental study on the new ultrafast transmission electron microscope (UTEM) installed in Strasbourg, which operates with a thermionic gun and Wehnelt electrode assembly with adjustable bias. In a first part, the pre-installed stroboscopic setup, was finalized and investigated in detail. It works with trains of picosecond multi-electron pulses in order to study ultrafast, reversible processes. Electron pulse dynamics and new mechanisms were unveiled, which define the electron pulse arriving at the sample. The second part was dedicated to the installation and test phase of a complementary operation mode working in single-shot approach with intense nanosecond electron pulses for the investigation of irreversible transformations.

This microscope is the first one worldwide capable to work in both operation modes, which makes it a versatile instrument for materials sciences. The operation mode can be adapted to the process under investigation, offering highest temporal and spatial resolution for reversible transformations but also offering time-resolved TEM at a reduced resolution for irreversible processes, which represent the vast majority of material transformations.

The stroboscopic setup includes a femtosecond laser system, which is used to excite the sample and to emit photoelectron pulses from the TEM cathode. After successful synchronization of the laser-pump and electron-probe pulses on the sample, the electron pulse characteristics were studied in detail. For this purpose, an aloof microscopy technique called photon induced near-field electron microscopy (PINEM) was exploited. It is based on the coupling of the electron wave with an optical near-field around the sample, causing the electrons to exchange entire quanta of photon energy, which can be followed in electron energy loss spectroscopy (EELS). In this stroboscopic TEM, the pump laser pulse generates the near-field. From PINEM scans with varying delay between optical pump and electron probe pulse the important characteristics of the electron pulse can be extracted. These are the temporal profile, the arrival time and the energy width.

In detail, the temporal length of an electron pulse and its energy distribution were found anti-correlated, which clearly states that Coulomb interactions between the electrons can not be the dominating effect. A parametric study revealed two regimes in the evolution of the temporal pulse length. A first one is governed by these Coulomb interactions. The second regime, showing a drastic increase of the pulse length, could be related to trajectory effects. At a certain Wehnelt bias voltage, two electron populations are mixed - the central emission along the optical axis, and a small halo comprising electrons emitted at high angle. Following different trajectories, the arrival time of these electron populations varies up to 100 ps, which explains the hugely increased temporal elongation of the overall pulse.

The energy distribution is initially driven by space charge and Boersch effect at the cathode surface, where the electron density is high, as well as the interaction time because the electrons are not yet accelerated. However, the strong chromatic aberration of the electrostatic Wehnelt lens induces a chromatic dispersion within the electron pulse, which leads to a chromatic filtering on subsequent apertures. This filtering effect could be identified as the determining factor for the energy width of the electrons reaching the sample.

Throughout this study, critical instrumental parameters could be identified. These are mainly the UV laser pulse energy, defining the initial number of electrons per pulse, and the bias voltage applied on the Wehnelt cone, which controls numerous effects in the gun area (extraction field, potential barrier, gun-cross over, beam convergence and spectral dispersion). The Wehnelt bias has been found to be of utmost importance, providing versatility when trading off temporal resolution, energy resolution and signal intensity.

Due to the chromatic filtering, ΔE and signal are correlated, whereas the temporal resolution is anti-correlated. For time-resolved experiments, compromises have to be found. Special care has to be attributed to the trajectory effects. Pulsed stroboscopic operation is limited to one unique electron population, which is the on-axis central emission. A 3D-plot was drawn, serving as reference when adapting the instrument to the experimental needs.

This study lead to a detailed understanding of the stroboscopic UTEM. It revealed phenomena which are on the one hand valuable from a fundamental point of view, possibly leading to improved instruments. On the other hand, the acquired knowledge enables a quick, target-oriented adaptation of the microscope to the experimental needs in materials sciences, which are quite different for imaging and EELS. Furthermore, an accurate interpretation of time-resolved experiments can be guaranteed knowing the characteristics of the probe pulses.

The versatility of the thermionic gun setup with Wehnelt electrode could be demonstrated. Apart from the Wehnelt itself, which enables diverse working conditions, the exchangeable cathode adds a degree of freedom. Large disc-shaped emitter can be used to maximize signal, truncated tips with a small emission area produce less intense but highly coherent electron pulses.

In the scientific community, stroboscopic imaging, electron diffraction and EELS experiments are carried out since several years. However, no study revealed the underlying phenomena. Coulomb interactions were widely discussed. This work could now attribute the main contribution to space charge and Boersch effect at the cathode; otherwise chromatic filtering would not be so efficient. The chromatic filtering explains the anti-correlation of temporal and energy resolution. Furthermore, trajectory effects could be identified as detrimental to temporal resolution when different electron populations are mixed. This happens especially at "saturated" emission, the standard working condition in conventional TEM which has to be omitted in time-resolved experiment.

The second part of this thesis focused on the single-shot operation mode. A first step was the design and implementation of a nanosecond laser system into the existing stroboscopic UTEM, which is needed for the generation of the intense electron pulses. Subsequently, the setup was put into operation and test runs were carried out to determine the potential and identify critical aspects. The parameter set is simplified with respect to the stroboscopic setup. A temporal pulse elongation in the order of picoseconds is irrelevant for a pulse length of several nanoseconds. Energy distribution and signal intensity remain key parameters.

Working on the first single-shot TEM worldwide which is coupled to an electron energy loss spectrometer, the analysis of the electron pulse properties could be taken to a new level. A parametric study has been

carried out, analyzing the interplay of energy distribution and signal intensity with varying instrumental parameters. Tracing the energy distribution, valuable information about the impact of chromatic aberration on diverse TEM techniques could be revealed.

A huge energy distribution above 500 eV was found for the intense ns-pulses under conditions when most electrons are focused onto the detector. Single-shot EEL spectra showed the statistical behavior of inhomogeneous Coulomb interactions, most probably due to unavoidable laser instabilities, which make the spectra of single pulses unreproducible. This fact has often been discussed in the scientific community and was thought detrimental for single-shot EELS. Nevertheless, this study demonstrates that severe filtering can refine the energy distribution down to 2.1 eV, which is very close to the intrinsic limitation of 1.7 eV due to the kinetic energy after photoemission. As soon as electrons far from the optical axis are sheltered, the resulting electron pulses are sufficiently uniform and reproducible for time-resolved single-shot experiments.

The general trends found in stroboscopic operation remain valid for nanosecond electron pulses of the single-shot setup. The Wehnelt bias voltage remains a key parameter driving chromatic filtering and the shape of the emission pattern, composed of individual electron populations which merge in "saturated" conditions.

The investigation of imaging conditions revealed a strong influence of chromatic and spherical aberration induced blurring. For single-shot images, an energy spread of several tens of electronvolts is inevitable, in order to maintain sufficient signal intensity. The "saturation" represents optimum imaging conditions, as the appearance of the off-axis halo electrons significantly increases the signal. Quantitative estimations confirmed the image resolution to be limited by the combination of shot noise and aberrations of the objective lens.

Furthermore, the effect of chromatic aberration could be demonstrated in electron diffraction, where it appears as blurring and an increased diameter of the diffraction spots.

A revolutionary result was achieved in electron energy loss spectroscopy. The feasibility of core-loss EELS with one unique ns-electron pulse could be demonstrated on the carbon K edge of an amorphous carbon membrane. In the scientific community, this was speculated to be too challenging. [29] This result is very promising, as it leads the way to chemical reaction dynamics studied by tracing the evolution of characteristic peaks in core-loss EELS.

Perspectives

Near-term perspectives focus on the optimization of the single-shot setup. Especially, an increase of the signal intensity is pursued at constant energy distribution. Therefore, Coulomb interactions have to be reduced. The UV beam profile has to be improve as much as possible in order to assure a homogeneous, even though Gaussian shaped energy distribution. Furthermore, the cathode might be revised (roughness, grain boundaries, defects) to reduce local hot-spots of electron emission.

For the stroboscopic setup, instrumental improvements are further ahead. An optimized design of the Wehnelt assembly would clearly improve the performance. More uniform electron trajectories without the fragmentation in distinct electron populations would eliminate the drastic loss of temporal resolution upon merged populations and allow the use of most emitted electrons for the image formation. An increased signal leaves more room for filtering in order to improve spatial or energy resolution and reduces the acquisition time.

Intriguing for both operation modes would be the possibility to correct chromatic aberrations. Particular care has to be attributed to the conservation of the temporal pulse length. Especially in stroboscopic mode working with ps-pulses this seems challenging.

Naturally, the perspectives of the ultrafast TEM comprise numerous projects in materials sciences. A detailed instrumental study forms the basis on which application will follow. In single-shot mode, the irreversible transformation of nanoparticles are generally speaking a hot topic.

The most intriguing projects to be carried out in Strasbourg are single-shot EELS experiments, being a world novelty. Once the oxygen peak can be resolved (most likely possible with slightly enhanced signal), the reduction and oxidation of diverse materials can be traced by the disappearance and reappearance of the oxygen peak. The reduction can easily be carried out inside the TEM. Studies about the stability of oxides are of great interest and will be one of the first materials sciences projects.

For stroboscopic operation all processes undergoing a lateral expansion upon laser irradiation are of great interest, provided the transformation is reversible. One example are photostrictive materials. Also, hybrid materials can present interesting behavior, e.g. in the case of molecular switches.

Ultrafast transmission electron microscopes are still rare, the number of investigated samples is limited. Consequently, there is plenty of room for interesting research projects aiming to unveil secrets in the nanoscale world.

Résumé de thèse en français
- Summary in French -

Caractérisation des impulsions électroniques pico- et nanoseconde en microscopie électronique en transmission ultrarapide

Cette thèse se situe dans le cadre des équipement d'excellence (Equipex 2011). Ce projet est intitulé *Ultrafast Transmission Electron Microscopy - UTEM*. Ma thèse porte sur le développement instrumental de ce microscope électronique à haute résolution temporelle. Concrètement, mon travail a débuté juste après la livraison du microscope et a constité à rendre opérationnel cet instrument pionnier dont il n'existe que quelques exemplaires à travers le monde.

Le manuscript anglais est constituée de six chaptitres, incluant une brève introduction, deux chapitres généraux sur la physique de la dynamique ultrarapide et la technique de microscopie ultrarapide, ainsi que deux chapitres présentant les résultats expérimentaux et un dernier chapitre de conclusions et perspectives.

Ce résumé contient une introduction au sujet suivie de deux parties qui résument les deux chapitres expérimentaux, correspondant aux deux différets modes de fonctionnement de l'UTEM.

7.1   Introduction

L'un des aspects les plus remarquables des nanomatériaux tient à l'étroitesse de leur relation structure-propriétés. La compréhension des transformations physico-chimiques qui affectent leur structure est donc un enjeu majeur tant d'un point de vue fondamental que technologique. Or, la dynamique des processus physico-chimiques accélère souvent à mesure que la taille des objets considérés diminue. Ainsi, les transformations que subissent les nanomatériaux telles que les changements de phase, les phénomènes magnétiques, les réactions chimiques, ou la migration de défauts structuraux se produisent à des échelles de temps allant de la microseconde à la femtoseconde, voir figure 7.1. Bien que nous disposions de connaissances détaillées sur les états initiaux et finaux de ces transformations, les états transitoires demeurent généralement inconnus, ou du moins sujets aux seules spéculations théoriques. Pour pouvoir les analyser, il est nécessaire de combiner hautes résolutions spatiale et temporelle.

Pour y parvenir, O. Bostanjoglo proposait pour la première fois dans les années 70 l'idée de coupler la résolution spatiale sub-nanométrique offerte par la sonde d'électrons relativistes d'un microscope électronique à transmission avec la résolution temporelle picoseconde des approches pompe-sonde. [12] En 2005, Ahmed Zewail, qui avait reçu le prix Nobel de chimie en 1999 pour ses travaux à Caltech sur la spectroscopie femtoseconde, a produit les premières images à haute résolution en mode stroboscopique. [80] En parallèle, N. Browning, T. Lagrange et W. King développaient au Lawrence Livermore National Laboratory le mode à impulsion unique : « single-shot ». [29] Ces deux modes sont complémentaires car si le mode stroboscopique permet d'atteindre de meilleures résolutions spatiale et temporelle il reste cantonné au domaine des processus réversibles, au contraire du mode à impulsion unique. L'UTEM développé à l'IPCMS est à ce jour le seul à être optimisé pour pouvoir opérer dans les deux modes.
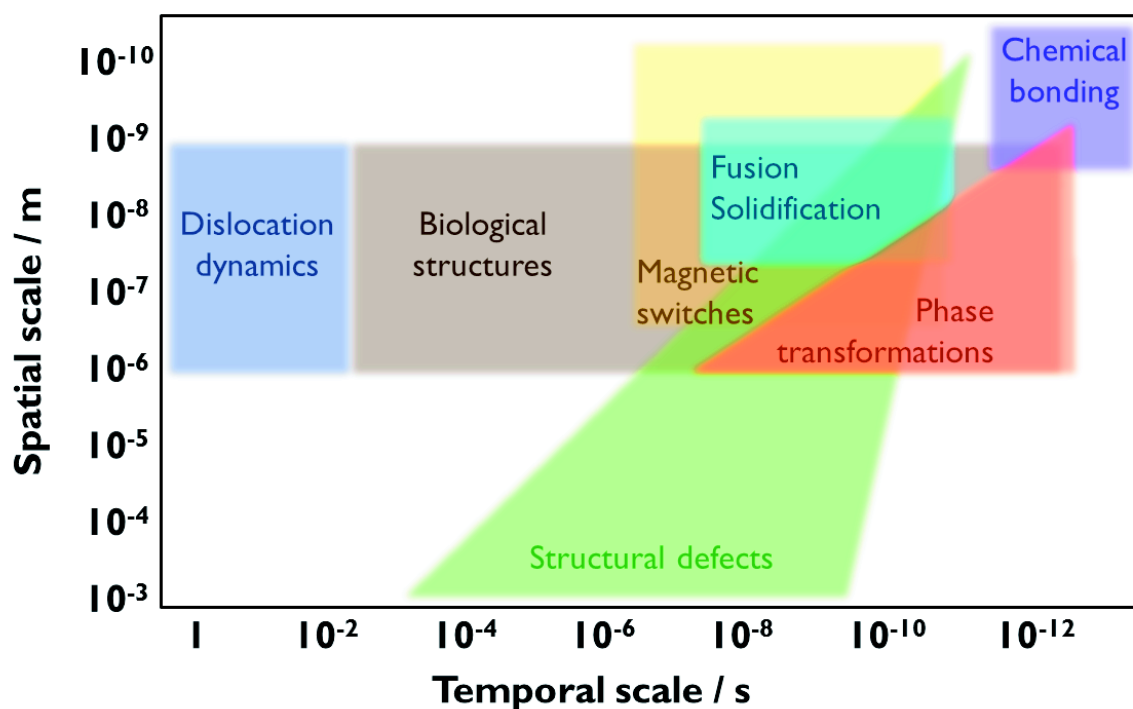
Figure 7.1: *Exemples de processus dynamiques classés selong leur échelle spatiale et temporelle. Adapté de [26].*

La principale limitation d'un UTEM tient au fait que les électrons sont des particules chargées, et que contrairement aux photons, on ne peut comprimer un grand nombre d'entre eux sans qu'ils n'interagissent mutuellement et se repoussent. Or, pour former une image TEM sur la caméra CCD, il faut de l'ordre de 10^8 à 10^9 électrons au moins. Dans l'approche TEM classique, le faisceau d'électrons est continu, c'est-à-dire que les électrons sont éjectés de la cathode les uns après les autres et sont suffisamment éloignés spatio-temporellement pour ne pas ou peu interagir. À contrario, l'approche UTEM comprime cette dose d'électrons nécessaire à la formation d'une image dans un temps/volume très restreint ce qui se traduit par interaction coulombienne, des dispersions énergétiques, temporelles et spatiales importantes et par les pertes en résolution résultantes. C'est autour de cette problématique que se sont articulées les recherches de cette thèse.

7.2 UTEM stroboscopique

La première partie de la thèse traite le mode stroboscopique, dont les pricipaux composants ont été préinstallé lors de mon arrivée à Strasbourg. Ce mode est basé sur l'utilisation d'un train d'impulsions. Les paires d'impulsions pompes (excitation de l'échantillon à t_0) et sondes (formation de l'image à $t_0 + \Delta t$) sont séparées par un retard Δt ajustable, et un grand nombre d'impulsions participent alors à la formation de l'image. Cela permet de réduire drastiquement le nombre d'électrons par impulsion, et donc de minimiser les phénomènes d'interaction électron-électron à l'origine des pertes en résolutions. L'inconvénient majeur de ce mode est qu'après avoir été excité, l'échantillon doit se rétablir à son état initial avant l'arrivée de l'impulsion suivante. C'est pourquoi cette méthode ne s'applique donc qu'aux processus réversibles.

Nous avons effectué une étude approfondie sur les dynamiques des impulsions d'électrons. Ainsi, nous avons pu identifier les paramètres clés et étudier de façon systématique leurs influences respectives : la puissance du laser UV générant les photoélectrons, la géométrie et la position de la photocathode, ainsi que la tension appliquée sur la lentille électrostatique du canon à électrons appelé « Wehnelt ».

La figure 7.2 montre l'évolution de la durée de l'impulsion électronique (Δt_e) et la dispersion énergétique (ΔE) en fonction du bias appliqué sur le Wehnelt. Le comportement du Δt_e montre deux régimes, dont le premier à faible bias comprend une légère augmentation lorsque le bias augmente. Passé un certain seuil, ici 350 V, l'impulsion électronique s'allonge de façon importante avec l'augmentation du bias. D'un autre côté, la distribution énergétique diminue lorsque le bias augmente.

(a) *Longuer temporelle.*   **(b)** *Distribution énergétique.*
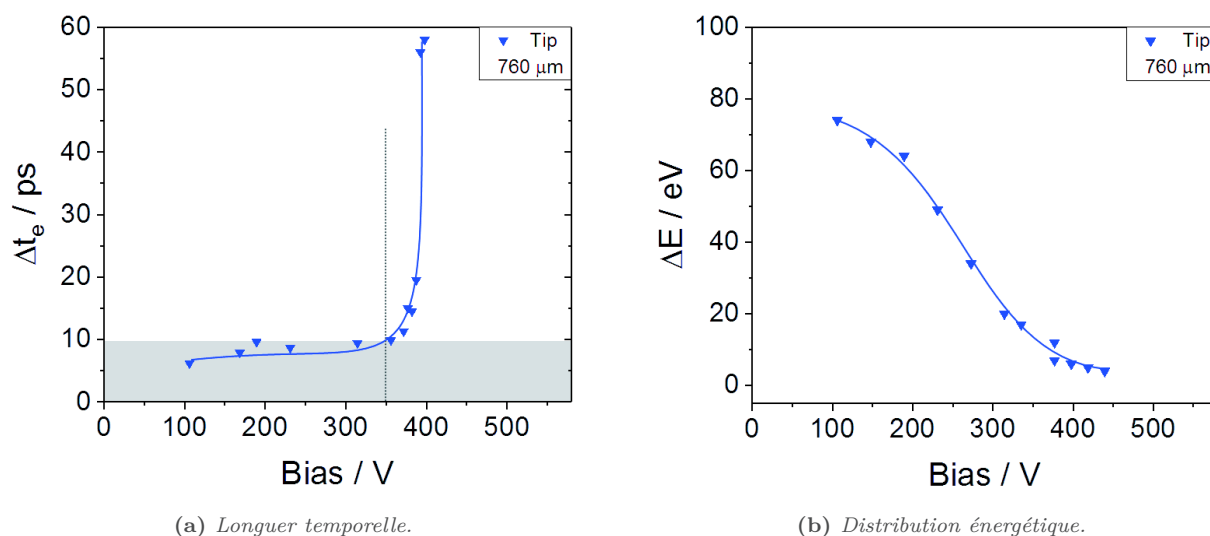
Figure 7.2: *Comportement des impulsions électroniques en fonction de la tension appliqué sur le Wehnelt. Cathode en forme de pointe aplatie, situé à 760 µm de l'ouverture du Wehnelt.*

Dans la litérature, seule l'interaction coulombienn entre les électrons (aussi appelée effet Boersch et charge d'espace) était jusqu'à ce jour considérée pour expliquer les évolutions relatives des résolutions temporelles (Δt_e) et énergétiques (ΔE). Selon ce modèle toute augmentation du ΔE (dispersion en énergie et donc en vitesse) se traduit nécessairement par un allongement temporelle de l'impulsion. Or, les résultats obtenus ont mis en évidence l'anti-corrélation de ΔE et Δt_e en fonction de la valeur de tension appliquée à l'électrode Wehnelt.

Suite à des investigations étendus nous avons pu dévoiler les mécanismes qui déterminent les caractéristiques des impulsions électroniques. Concernant l'élongation temporelle, il s'agit des effets de trajectoire. La figure 7.3 présente les différentes populations électroniques en foncion de leur zone et de leur angle d'émission. A haut bias deux populations électroniques, ayant suivi des trajectoires différentes, sont mélangées. Concrètement, il s'agit des électrons émis de la zone aplatie de façon *(i)* parallèle à l'axe optique ou *(ii)* avec un angle non nul (représentés en noir et rouge respectivement). Les différentes trajectoires se traduisent par différentes langueurs de trajet, donc par des temps d'arrivée hétérogènes. Par conséquent, l'impulsion électronique conprenant les deux populations se trouve allongée. Ceci explique le deuxième régime dans lequel Δt_e croit rapidement. Le premier régime, quant à lui, est gouverné par les interactions coulombiennes.
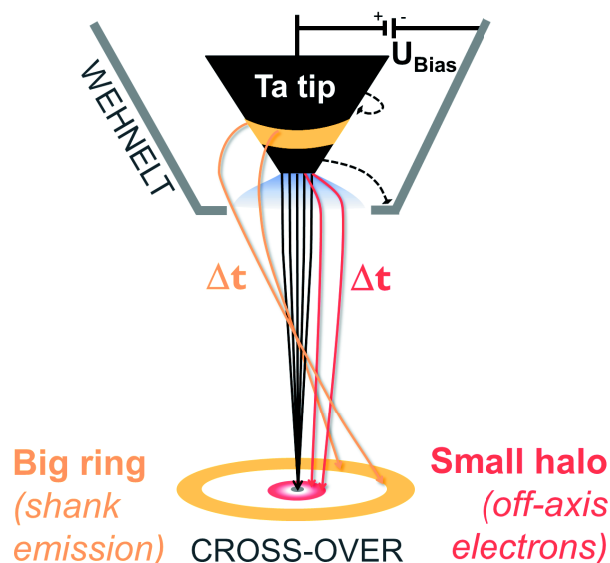
Figure 7.3: *Schema : Séparation des électrons émis en populations distincts.*

L'évolution de la distribution énergétique peut être expliqué par le filtrage chromatique excercé par le Wehnelt (voir figure 7.4). Le Wehnelt est une lentille électrostatique présentant une forte aberration chromatique. Les électrons sont donc dispersés énergétiquement. Par la suite, le filtrage s'opère au niveau du diaphragme de l'anode, situé sous le Wehnelt.
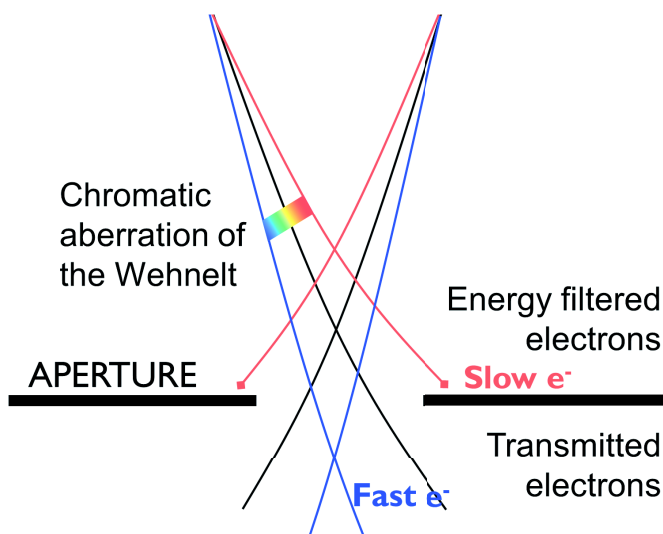
Figure 7.4: *Schema : Filtrage chromatique par un diaphragme, suite à la dispersion énergétique par l'aberration chromatique du Wehnelt.*

Grâce à ce travail de fond, il est désormais possible de tirer le maximum du potentiel de cet instrument. On comprend aujourd'hui les évolutions de la résolution temporelle, de la dispersion en énergie et de l'intensité de signal, trois paramètres entre lesquels il s'avère nécessaire de définir des compromis adaptés aux besoins expérimentaux (voir figure 7.5). Ceci est un grand pas en avant car jusqu'ici, le maniement des paramètres de l'UTEM avait une dimension essentiellement empirique. Les résolutions optimales obtenues séparément sont de 2.3 Å, 0.8 eV et de 2 ps.
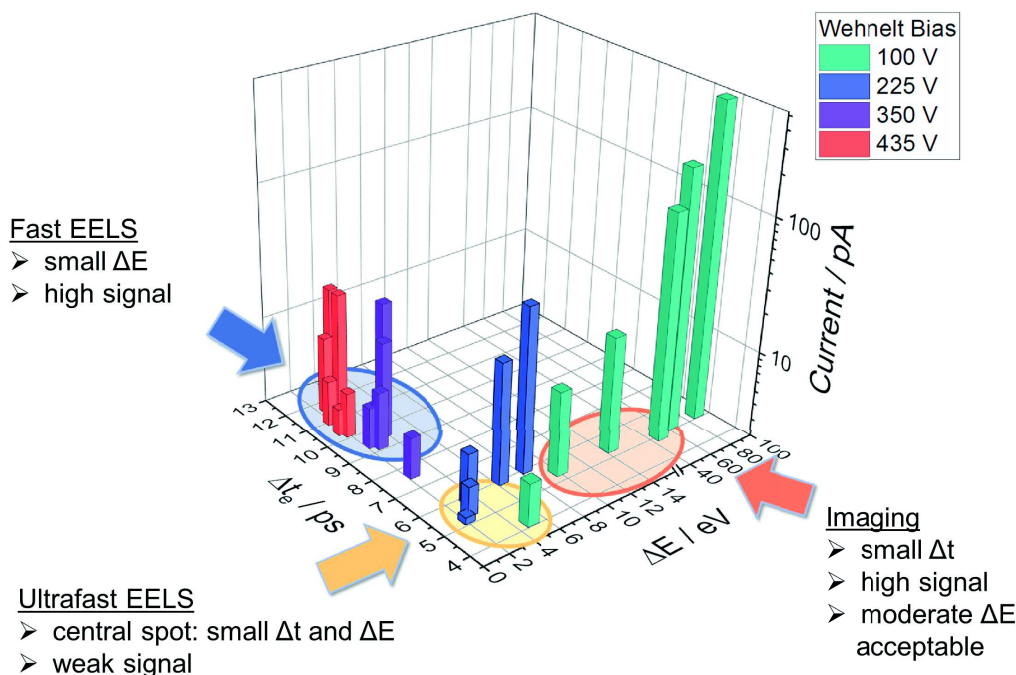
Figure 7.5: *Diagramme présentant les différentes conditions de travail de l'UTEM pour une configuration de photocathode donnée (disque de tantale, placé à 500 µm du Wehnelt). Les quatre séries de points correspondent à quatre réglages du Wehnelt différents. Pour chaque série, les points correspondent à différentes puissance du faisceau UV.*

7.3 UTEM à impulsion unique

La deuxième partie de la thèse porte sur le mode « single-shot ». Ici, on fait appel à une impulsion unique qui contient suffisamment d'électrons pour former une image, ouvrant la voie au champ des processus irréversibles. La contrepartie est une résolution spatio-temporelle moindre en raison du grand nombre d'électrons dans l'impulsion unique (10^8 à 10^{10}). Compte-tenu du grand nombre d'électrons présent dans le paquet sonde, celui-ci est plusieurs ordres de grandeur plus long et la résolution temporelle se situe autour de la dizaine de nanosecondes.

Ici le travail comprend la conception et le développement instrumental, ainsi que des tests de performance. La mise en place du mode single-shot a nécessité l'achat d'un nouveau laser produisant des impulsions à 213 nm (cinquième harmonique) d'une durée d'environ 7 ns. Le choix de cette longueur d'onde a été fait car l'efficacité quantique du tantale gagne un ordre de grandeur entre la fréquence quadruplée et quintuplée : à 213 nm, elle est de l'ordre de 10^{-4} électrons émis par photon, contre 10^{-5} à 258 nm. Ainsi, une impulsion unique génère un nombre d'électron suffisant pour former une image, soit environ 10^8 à 10^9 électrons atteignant la caméra, conformément à nos prévisions.

Dans cette configuration, le laser femtoseconde infrarouge du mode stroboscopique est utilisé pour la pompe, en impulsion unique. Les deux lasers sont interfacés avec une ligne à retard électronique, qui permet de décaler les impulsions sur une gamme allant de la nanoseconde à la seconde.

Compte-tenu des échelles de temps mises en jeu, les effets de trajectoire ainsi que les phénomènes d'allongement temporel des impulsions en général peuvent ici être négligés, rendant le système notoirement plus simple. En

revanche, l'intensité du signal est le paramètre clé dans le cas présent. Étant limité à une impulsion unique, une intensité faible ne peut pas être compensé par un temps d'acquisition plus long. Afin d'atteindre l'intensité requise, il est nécessaire de trouver un compromis avec la dispersion en énergie. Ces deux caractéristiques sont influencées par la puissance UV (le nombre d'électrons initialement émis) et par le bias du Wehnelt (filtrage chromatique). Un ΔE élevé correspond à une haute intensité mais limite la résolution à cause de l'aberration chromatique de l'objectif. Enfin, le nombre d'électrons qui contribuent à la formation de l'image ou du spectre peut être augmenté en convergeant le faisceau électronique sur l'échantillon. Ceci provoque l'aberration sphérique qui limitera également la résolution.

L'intensité du signal et la dispersion en énergie ont été étudiées systématiquement. A titre d'exemple, la figure 7.6 montre l'effet du bias pour des énergie d'impulsions laser UV données (en code couleur). Le résultat et représenté dans un diagramme montrant le nombre d'électrons pas impulsion en fonction de la dispersion en énergie.
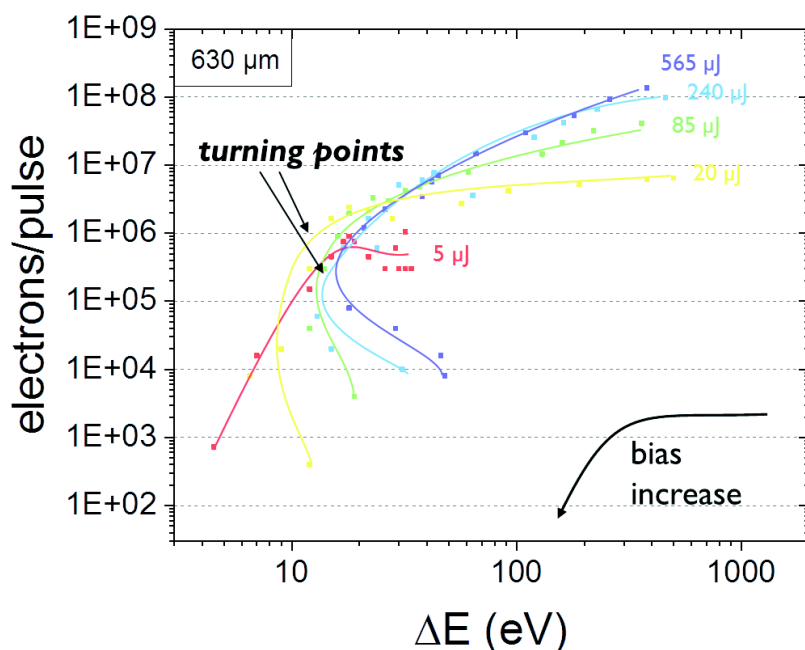
Figure 7.6: *Évolution des caractéristiques des impulsions électroniques nanoseconde : nombre d'électrons par impulsion en fonction de la dispersion en énergie pour plusieurs énergies UV. Chaque courbe.... correspond à une puissance UV donnée et différents caleurs de bias. La distance entre cathode (disque de tantale) et ouverture du Wehnelt est de 630 µm.*

Le « turning point » indiqué dans la figure s'avère important d'un point de vue expérimental, comme il représente un bon compromis entre signal et ΔE.

L'UTEM de Strasbourg étant le premier instrument single-shot équipé d'un spectromètre de perte d'énergie des électrons (EELS), il nous a permi d'investiger la distribution en énergie des impulsions électroniques. La figure 7.7a montre des spectres d'impulsions uniques, aquis à faible bias (sans filtrage chromatique). Les spectres montrent des distributions énergétiques de presque un 1000 électron volts, ainsi que des fluctuations prononcés entre les impulsions. Ces dernières résultent des instabilités intrinsèques au profil du laser UV. Évidemment, ces conditions ne permettent aucune expérience reproducible. Néanmoins, les mécanismes comprises lors de l'investigation du mode stroboscopique nous permettent d'affiner la dispersion énergétique. La figure 7.7b montre une largeur à mi-hauteur de 2.1 eV, ce qui est seulement 0.4 eV au dessus de la limite

théorique (énergie des photons UV à 213 nm de 5.8 eV retranchée du travail de sortie du tantale de 4.1 eV). Ici, l'application d'un bias élevé sur le Wehnelt effectue un filtrage chromatique sévère, et l'utilisation des impulsions laser de faible intensité diminue le nombre d'électrons par impulsion et ainsi les interactions coulombiennes. Le spectre est intégré sur 100 impulsion, étant donné que le signal est trop faible pour des mesures à impulsion unique.

(a) Spectres des impulsions uniques sans filtrage.

(b) Distribution énergétique ultime.
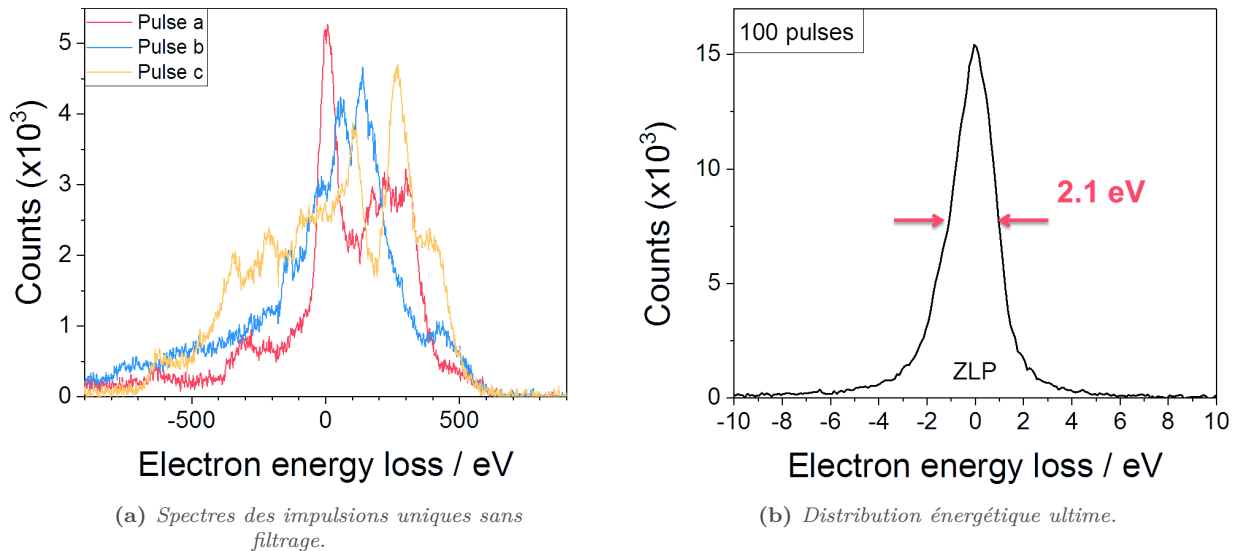
Figure 7.7: Spectres de perte d'énergie des électrons. (a) Spectres des impulsions uniques sans filtrage (à bias minimal) et à une énergie d'impulsions UV modéré de 85 µJ. (b) Spectre intégré sur 100 impulsion, montrant la résolution énergétique ultime en appliquant un filtrage chromatique sévère (bias maximal) et une énergie d'impulsions UV faible de 5 µJ.

Pour effectuer des mesures EELS à impulsion unique, un compromis entre l'intensité du signal et la résolution énergétique est nécessaire. La figure 7.8 montre les premier spectres EEL obtenus en mode « single-shot » montrant des seuils core-loss.

(a) Single-shot carbon K edge.

(b) Single-shot nickel L edge.
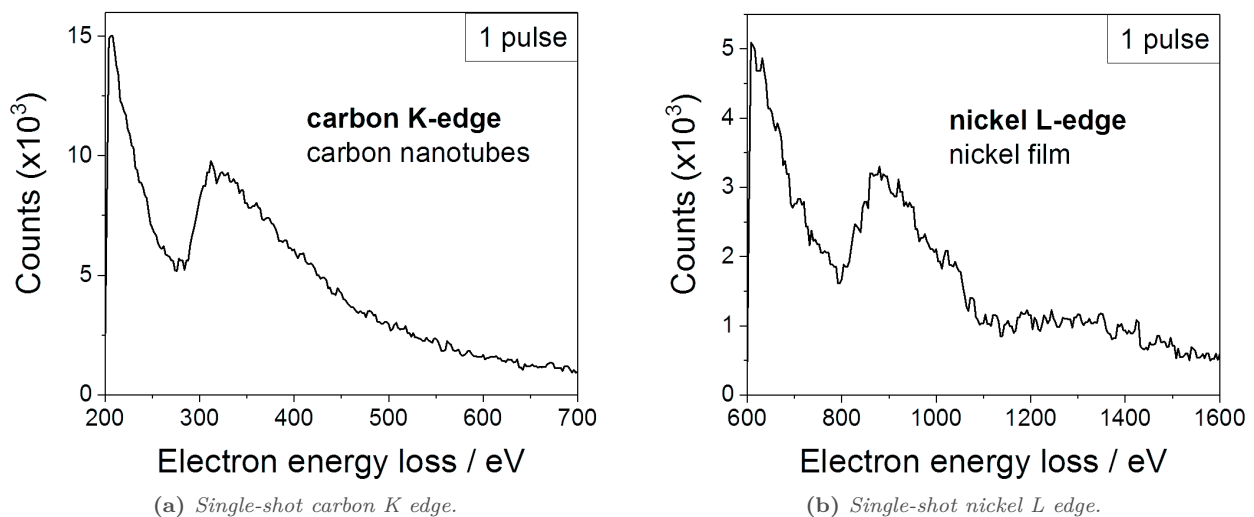
Figure 7.8: Premiers spectres EEL obtenus avec une impulsion unique de 14 ns, montrant (a) le seuil K du carbone et (b) le seuil L du nickel. Les spectres ont été obtenus avec un ΔE de 30 eV et 5×10^6 electrons/impulsion (energy impulsion UV 200 µJ, Wehnelt bias 665 V) et de 60 eV (energy impulsion UV 450 µJ, Wehnelt bias 560 V) respectivement.

En imagerie, les effect d'aberrations de la lentille objective ont été étudiés en détail. Due à la large dispersion en énergie comparée au mode conventionel, la résolution est limité par l'aberration chromatique. De plus, la nécessité de converger le faisceau et ne plus travailler en illumination parallèle, limite la résolution par l'effect de l'aberration sphérique. A ces deux effect se rajoute une limite de résolution due au rapport signal sur bruit. La figure 7.9 montre les meilleures images à cette date ; a noter que le système fait encore object d'améliorations. La résolution ultime multipulse rend une résolution de bord de 5 nm. La résolution de l'image à impulsion unique est de 25 nm.

(a) *Résolution ultime, image intégrée sur 1000 impulsions.*

(b) *Image à impulsion unique.*
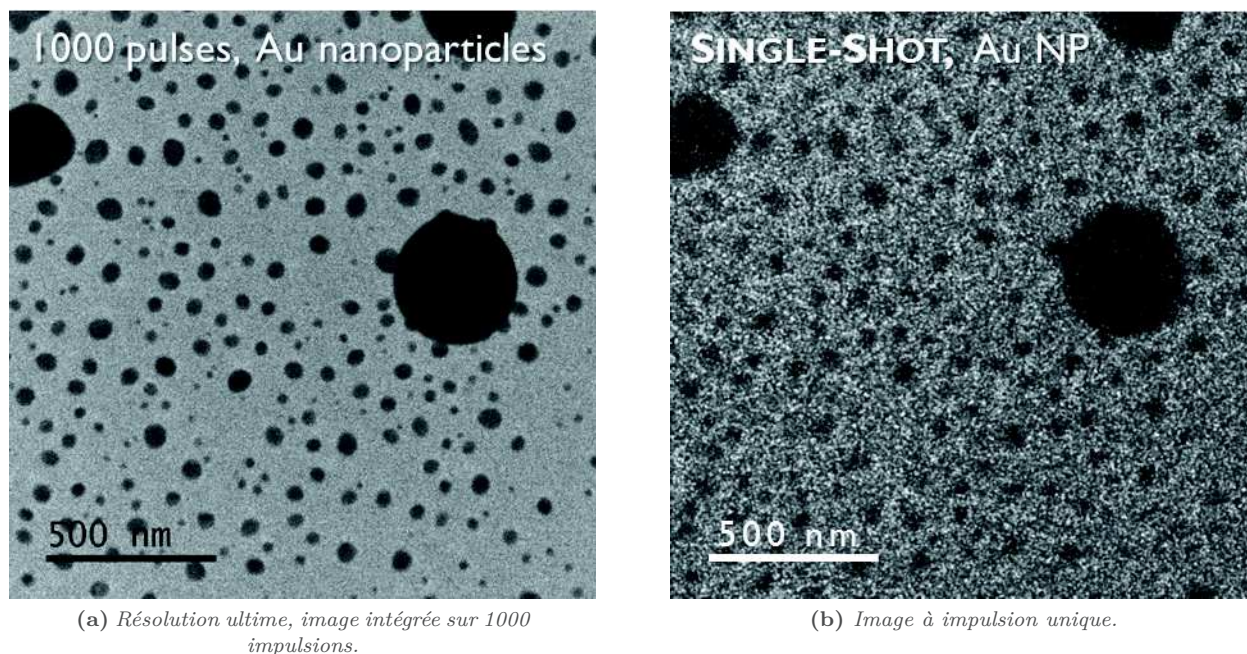
Figure 7.9: *Meilleures images obtenues avec des impulsions électroniques de 14 ns. La résolution de bord est de (a) 5 nm et de (b) 25 nm.*

Les résultats obtenus en mode single-shot suscitent beaucoup d'espoir et promettent l'étude d'une grande variété de processus physico-chimiques irréversibles en mode imagerie, diffraction et EELS à une échelle de temps de l'ordre de la dizaine de nanosecondes.

7.4   Conclucions et perspectives

Cette thèse présente une étude des impulsions électroniques ultra-brèves en utilisant le nouveau microscope électronique en transmission ultrarapide à Strasbourg. Ce travail à permis de découvrir qu'en mode stroboscopique en plus des interactions coulombiennes l'effet de trajectoires limite la résolution temporelle. Le filtrage chromatique du Wehnelt détermine la distribution en énergie et l'intensité du signal. Ces connaissances permettent aujourd'hui un paramétrage affiné de l'UTEM de manière à satisfaire les divers besoins expérimentaux.

Le mode « single-shot » a pu être installé avec succès. Des tests de performance ont démontré la nécessité d'ajuster le bon compromis entre l'intensité de signal et les aberrations chromatique et sphérique. La faisabilité de mener des études en EELS ultrarapide avec une seule impulsion nanoseconde a pu être démontrée

ce qui est une première mondiale.

Grâce à ce travail instrumental, plusieurs pistes d'améliorations sont maintenant envisagées : une modification de l'électrode Wehnelt, l'optimisation des optiques et de la photocathode. Pour minimiser les interaction coulombiennes, une émission d'électrons homogène est souhaitable. Pour cela, le profil du laser UV devra être amélioré, avec pour objectif d'obtenir un profil spatio-temporel de type « flat-top ». De même, une cathode sans rugosité, monocristalline et sans défauts devrait permettre d'éviter les inhomogénéités d'émission. L'optimisation de la géométrie du Wehnelt visera l'obtention de trajectoires plus uniformes, sans segregation en différentes populations avec des temps d'arrivés distincts, ainsi qu'un courant d'émission plus élevé à dispersion en énergie donnée.

En parallèle, le projet rentre dans sa phase expérimentale et plusieurs matériaux sont d'ores et déjà en phase de test. La dynamique de réduction des nanoparticules d'oxides métalliques est étudié en mode single-shot. En mode stroboscopique les dynamiques spatiales des matériaux photostrictifs et des intérupteurs moléculaires (matériaux hybrides inorganique-organique) seront étudiés, ainsi que les dynamiques de liquéfaction et resolidification des nanoparticules ou couches métalliques.

Bibliography

[1] A. H. Zewail, "Femtochemistry: Atomic-Scale Dynamics of the Chemical Bond Using Ultrafast Lasers (Nobel Lecture)," *Angewandte Chemie International Edition*, 39(15), 2586–2631, **2000**, doi:10.1002/1521-3773(20000804)39:15<2586::AID-ANIE2586>3.0.CO;2-O.

[2] A. H. Zewail, "Laser Femtochemistry," *Science*, 242(4886), 1645–1653, **1988**.

[3] R. Simpson *et al.*, "Interfacial phase-change memory," *Nature Nanotechnology*, 6(8), 501–505, **2011**, doi:10.1038/nnano.2011.96.

[4] B. S. Lee *et al.*, "Observation of the Role of Subcritical Nuclei in Crystallization of a Glassy Solid," *Science*, 326(5955), 980–984, **2009**, doi:10.1126/science.1177483.

[5] S. Bahr *et al.*, "Pump-Probe Experiments on the Single-Molecule Magnet Fe_8: Measurement of Excited Level Lifetimes," *Physical Review Letters*, 99, 147205, **2007**, doi:10.1103/PhysRevLett.99.147205.

[6] R. W. Schoenlein *et al.*, "Generation of Femtosecond Pulses of Synchrotron Radiation," *Science*, 287(5461), 2237–2240, **2000**, doi:10.1126/science.287.5461.2237.

[7] R. Schoenlein *et al.*, "Generation of femtosecond X-ray pulses via laser–electron beam interaction," *Applied Physics B*, 71(1), 1–10, **2000**, doi:10.1007/PL00021152.

[8] A. Maksimchuk *et al.*, "Signal averaging x-ray streak camera with picosecond jitter," *Review of Scientific Instruments*, 67(3), 697–699, **1996**, doi:10.1063/1.1146843.

[9] M. Altarelli, "From 3rd- to 4th-generation light sources: Free-electron lasers in the X-ray range," *Crystallography Reports*, 55(7), 1145–1151, **2010**, doi:10.1134/S1063774510070072.

[10] D. M. Mills, "Time resolved X-ray diffraction and spectroscopy using synchrotron radiation," *Nuclear Instruments and Methods In Physics Research*, 222(1), 159, **1984**.

[11] M. Chergui and A. H. Zewail, "Electron and X-Ray Methods of Ultrafast Structural Dynamics: Advances and Applications," *ChemPhysChem*, 10(1), 28–43, **2009**, doi:10.1002/cphc.200800667.

[12] O. Bostanjoglo and T. Rosin, "Ultrasonically Induced Magnetic Reversals Observed by Stroboscopic Electron Microscopy," *Optica Acta: International Journal of Optics*, 24(6), 657–664, **1977**, doi:10.1080/713819603.

[13] C. Bressler and M. Chergui, "Ultrafast X-ray Absorption Spectroscopy," *Chemical Reviews*, 104(4), 1781–1812, **2004**, doi:10.1021/cr0206667.

[14] B. E. Warren, *X-ray Diffraction*, Dover Publications, Inc., New York, USA, **1969**.

[15] D. Koningsberger and R. Prins, *X-ray absorption: principles, applications, techniques of EXAFS, SEXAFS, and XANES*, John Wiley and Sons, New York, USA, **1988**.

[16] D. M. Mills *et al.*, "Time-Resolved X-ray Absorption Spectroscopy of Carbon Monoxide-Myoglobin Recombination After Laser Photolysis," *Science*, 223(4638), 811–813, **1984**, doi:10.1126/science.223.4638.811.

[17] D. H. Bilderback, P. Elleaume and E. Weckert, "Review of third and next generation synchrotron light sources," *Journal of Physics B: Atomic, Molecular and Optical Physics*, 38(9), S773, **2005**, doi: 10.1088/0953-4075/38/9/022.

[18] R. Henderson, "The potential and limitations of neutrons, electrons and X-rays for atomic resolution microscopy of unstained biological molecules," *Quarterly Reviews of Biophysics*, 28(2), 171–193, **1995**, doi:10.1017/S003358350000305X.

[19] A. L. Ryland, "X-ray diffraction," *Journal of Chemical Education*, 35(2), 80, **1958**, doi:10.1021/ed035p80.

[20] P. Thibault and V. Elser, "X-Ray Diffraction Microscopy," *Annual Review of Condensed Matter Physics*, 1(1), 237–255, **2010**, doi:10.1146/annurev-conmatphys-070909-104034.

[21] G. Mourou and S. Williamson, "Picosecond electron diffraction," *Applied Physics Letters*, 41(1), 44–45, **1982**, doi:http://dx.doi.org/10.1063/1.93316.

[22] A. A. Ischenko *et al.*, "A stroboscopical gas-electron diffraction method for the investigation of short-lived molecular species," *Applied Physics B*, 32(3), 161–163, **1983**, doi:10.1007/BF00688823.

[23] C. Rischel *et al.*, "Femtosecond time-resolved X-ray diffraction from laser-heated organic films," *Nature*, 390, 490–492, **1997**.

[24] B. J. Siwick *et al.*, "Femtosecond electron diffraction studies of strongly driven structural phase transitions," *Chemical Physics*, 299(2-3), 285 – 305, **2004**, doi:http://dx.doi.org/10.1016/j.chemphys.2003.11.040. Ultrafast Science with X-rays and Electrons.

[25] S. Chen, M. T. Seidel and A. H. Zewail, "Ultrafast Electron Crystallography of Phospholipids," *Angewandte Chemie International Edition*, 45(31), 5154–5158, **2006**, doi:10.1002/anie.200601778.

[26] W. E. King *et al.*, *Science of Microscopy*, chapter 5 - High-Speed Electron Microscopy, 406–444, Springer, New York, **2007**, ISBN 978-0-387-49762-4, doi:10.1007/978-0-387-49762-4_5.

[27] O. Bostanjoglo and F. Heinricht, "Producing high-current nanosecond electron pulses with a standard tungsten hairpin gun," *Journal of Physics E: Scientific Instruments*, 20(12), 1491, **1987**.

[28] O. Bostanjoglo and T. Nink, "Hydrodynamic instabilities in laser pulse-produced melts of metal films," *Journal of Applied Physics*, 79(11), 8725–8729, **1996**, doi:http://dx.doi.org/10.1063/1.362499.

[29] T. LaGrange *et al.*, "Single-shot dynamic transmission electron microscopy," *Applied Physics Letters*, 89(4), 044105, **2006**, doi:http://dx.doi.org/10.1063/1.2236263.

[30] V. A. Lobastov, R. Srinivasan and A. H. Zewail, "Four-dimensional ultrafast electron microscopy," *Proceedings of the National Academy of Sciences of the United States of America*, 102(20), 7069–7073, **2005**, doi:10.1073/pnas.0502607102.

[31] D. A. Plemmons, P. K. Suri and D. J. Flannigan, "Probing Structural and Electronic Dynamics with Ultrafast Electron Microscopy," *Chemistry of Materials*, 27(9), 3178–3192, **2015**, doi:10.1021/acs.chemmater.5b00433.

[32] R. Bormann *et al.*, "Tip-Enhanced Strong-Field Photoemission," *Physical Review Letters*, 105, 147601, **2010**, doi:10.1103/PhysRevLett.105.147601.

[33] L. Wimmer *et al.*, "Terahertz control of nanotip photoemission," *Nature Physics*, 10(6), 432, **2014**.

[34] A. Feist *et al.*, "Quantum coherent optical phase modulation in an ultrafast transmission electron microscope," *Nature*, 521, 200–203, **2015**, doi:10.1038/nature14463.

[35] K. Echternkamp *et al.*, "Ramsey-type phase control of free-electron beams," *Nature Physics*, 12, 1000–1004, **2016**, doi:10.1038/nphys3844.

[36] F. Houdellier *et al.*, "Design and realization of an ultrafast cold field emission source operating under high voltage," in "The 16th European Microscopy Congress, Lyon, France," **2016**, doi: 10.1002/9783527808465.EMC2016.4759.

[37] H. Dömer and O. Bostanjoglo, "High-speed transmission electron microscope," *Review of Scientific Instruments*, 74(10), 4369–4372, **2003**, doi:10.1063/1.1611612.

[38] J. S. Kim *et al.*, "Imaging of Transient Structures Using Nanosecond in Situ TEM," *Science*, 321(5895), 1472–1475, **2008**, doi:10.1126/science.1161517.

[39] T. LaGrange *et al.*, "Strongly driven crystallization processes in a metallic glass," *Applied Physics Letters*, 94(18), 184101, **2009**, doi:http://dx.doi.org/10.1063/1.3125429.

[40] T. LaGrange, B. W. Reed and D. J. Masiel, "Movie-mode dynamic electron microscopy," *MRS Bulletin*, 40, 22–28, **2015**, doi:10.1557/mrs.2014.282.

[41] S. P. Weathersby *et al.*, "Mega-electron-volt ultrafast electron diffraction at SLAC National Accelerator Laboratory," *Review of Scientific Instruments*, 86(7), 073702, **2015**, doi:10.1063/1.4926994.

[42] K. Tanimura, "Toward Ultrafast Electron Microscope with Femtosecond Temporal Resolution, Atomic-Level Spatial Resolution, and Single-Shot Imaging Capability," *Microscopy and Microanalysis*, 21(S3), 651–652, **2015**, doi:10.1017/S143192761500405.

[43] R. F. Egerton, "Outrun radiation damage with electrons?" *Advanced Structural and Chemical Imaging*, 1(1), 1–11, **2015**, doi:10.1186/s40679-014-0001-3.

[44] R. Egerton, "Mechanisms of radiation damage in beam-sensitive specimens, for TEM accelerating voltages between 10 and 300 kV," *Microscopy research and technique*, 75(11), 1550–1556, **2012**.

[45] A. H. Zewail and J. M. Thomas, *4D Electron Microscopy - Imaging in Space and Time*, Imperial College Press, **2010**.

[46] R. Neutze *et al.*, "Potential for biomolecular imaging with femtosecond X-ray pulses," *Nature*, 406(6797), 752, **2000**, doi:10.1038/35021099.

[47] M. S. Hunter *et al.*, "X-ray diffraction from membrane protein nanocrystals," *Biophysical Journal*, 100(1), 198–206, **2011**, doi:10.1016/j.bpj.2010.10.049.

[48] T. Akashi *et al.*, "Information transfer of 25.5 nm^{-1} in a 1-MV field-emission transmission electron microscope," *Microscopy*, 65(4), 378, **2016**, doi:10.1093/jmicro/dfw009.

[49] T. Tanigaki *et al.*, "chapter 3 - Quest for Ultimate Resolution Using Coherent Electron Waves: An Aberration-Corrected High-Voltage Electron Microscope," in P. W. Hawkes, (ed.) "Advances in Electronics and Electron Physics," , volume 198 of *Advances in Imaging and Electron Physics* 69 – 125, Elsevier, **2016**, doi:http://dx.doi.org/10.1016/bs.aiep.2016.08.004.

[50] A. Rose, "Television Pickup Tubes and the Problem of Vision," *Advances in Electronics and Electron Physics*, 1, 131 – 166, **1948**, doi:http://dx.doi.org/10.1016/S0065-2539(08)61102-6.

[51] T. Lagrange *et al.*, *In-situ Electron Microscopy*, chapter 3 - Dynamic Transmission Electron Microscopy, 71–97, Wiley-VCH Verlag GmbH & Co. KGaA, **2012**, ISBN 9783527652167, doi:10.1002/9783527652167.ch3.

[52] W. E. King *et al.*, "Ultrafast electron microscopy in materials science, biology, and chemistry," *Journal of Applied Physics*, 97(11), 111101, **2005**, doi:http://dx.doi.org/10.1063/1.1927699.

[53] M. Reiser, *Theory and design of charged particle beams*, John Wiley & Sons, Weinheim, Germany, 2nd edition, **2008**.

[54] P. Kruit and G. Janasen, *Handbook of Charged Particle Optics*, chapter 7 - Space change and statistical Coulomb effects, Taylor & Francis Group, **2009**.

[55] H. Rose and R. Spehr, "Energy broadening in high-density electron and ion beams: The Boersch effect," *Advances in Electronics and Electron Physics, Supplement C*, 13, 475–530, **1983**. No access.

[56] R. Spehr, "Broadening of charged particle microprobes by stochastic Coulomb interactions," *Optik*, 70(3), 109–114, **1985**.

[57] S. T. Park, M. Lin and A. H. Zewail, "Photon-induced near-field electron microscopy (PINEM): theoretical and experimental," *New Journal of Physics*, 12(12), 123028, **2010**.

[58] K. Mizuno *et al.*, "Experimental evidence of the inverse Smith-Purcell evffect," *Nature*, 328, 45–47, **1987**.

[59] W. D. Kimura *et al.*, "Laser Acceleration of Relativistic Electrons Using the Inverse Cherenkov Effect," *Phys. Rev. Lett.*, 74, 546–549, **1995**, doi:10.1103/PhysRevLett.74.546.

[60] P. A. Čerenkov, "Visible Radiation Produced by Electrons Moving in a Medium with Velocities Exceeding that of Light," *Physical Review Letters*, 52, 378–379, **1937**, doi:10.1103/PhysRev.52.378.

[61] R. H. Pantell and M. A. Piestrup, "Free-electron momentum modulation by means of limited interaction length with light," *Applied Physics Letters*, 32(11), 781–783, **1978**, doi:10.1063/1.89893.

[62] F. J. García de Abajo and M. Kociak, "Electron energy-gain spectroscopy," *New Journal of Physics*, 10(7), 073035, **2008**.

[63] B. Barwick, D. J. Flannigan and A. H. Zewail, "Photon-induced near-field electron microscopy," *Nature*, 462, 902–906, **2009**, doi:10.1038/nature08662.

[64] F. J. García de Abajo, A. Asenjo-Garcia and M. Kociak, "Multiphoton Absorption and Emission by Interaction of Swift Electrons with Evanescent Light Fields," *Nano Letters*, 10(5), 1859–1863, **2010**, doi:10.1021/nl100613s.

[65] N. Talebi *et al.*, "Numerical simulations of interference effects in photon-assisted electron energy-loss spectroscopy," *New Journal of Physics*, 15(5), 053013, **2013**.

[66] D. J. Flannigan, B. Barwick and A. H. Zewail, "Biological imaging with 4D ultrafast electron microscopy," *Proceedings of the National Academy of Sciences*, 107(22), 9933–9937, **2010**, doi:10.1073/pnas.1005653107.

[67] S. T. Park *et al.*, "Graphene-layered steps and their fields visualized by 4D electron microscopy," *Proceedings of the National Academy of Sciences*, 110(23), 9277–9282, **2013**, doi:10.1073/pnas.1306661110.

[68] D. A. Plemmons *et al.*, "Characterization of fast photoelectron packets in weak and strong laser fields in ultrafast electron microscopy," *Ultramicroscopy*, 146, 97 – 102, **2014**, doi:http://dx.doi.org/10.1016/j.ultramic.2014.08.001.

[69] B. Leblond, G. Kuznetsov and M. Batazova, "Short pulse photoemission from LaB6-based materials," *Nuclear Instruments and Methods in Physics Research Section A: Accelerators, Spectrometers, Detectors and Associated Equipment*, 372(3), 562 – 566, **1996**, doi:http://dx.doi.org/10.1016/0168-9002(95)01449-7.

[70] J. M. Lafferty, "Boride Cathodes," *Journal of Applied Physics*, 22(3), 299–309, **1951**, doi:10.1063/1.1699946.

[71] R. H. Fowler, "The Analysis of Photoelectric Sensitivity Curves for Clean Metals at Various Temperatures," *Physical Review*, 38, 45–56, **1931**, doi:10.1103/PhysRev.38.45.

[72] D. E. Eastman, "Photoelectric Work Functions of Transition, Rare-Earth, and Noble Metals," *Physical Review B*, 2, 1–2, **1970**, doi:10.1103/PhysRevB.2.1.

[73] P. E. Oettinger, "Measured brightness of electron beams photoemitted from multicrystalline LaB6," *Applied Physics Letters*, 56(4), 333–334, **1990**, doi:10.1063/1.103290.

[74] M. Cardona and L. Ley, "Introduction," in "Photoemission in Solids I: General Principles," , volume 26 of *Topics in Applied Physics* 1 – 51, Springer Berlin Heidelberg, **1978**, doi:10.1007/3-540-08685-4.

[75] T. Anderson, I. V. Tomov and P. M. Rentzepis, "Laser-driven metal photocathodes for picosecond electron and x-ray pulse generation," *Journal of Applied Physics*, 71(10), 5161–5167, **1992**, doi:10.1063/1.350571.

[76] M. E. Haine and P. A. Einstein, "Characteristics of the hot cathode electron microscope gun," *British Journal of Applied Physics*, 3(2), 40, **1952**.

[77] A. Gahlmann, S. Tae Park and A. H. Zewail, "Ultrashort electron pulses for diffraction, crystallography and microscopy: theoretical and experimental resolutions," *Physical Chemistry Chemical Physics*, 10, 2894–2909, **2008**, doi:10.1039/B802136H.

[78] S. J. Pennycook and P. D. Nellist, (eds.), *Scanning Transmission Electron Microscopy*, Springer, New York, USA, **2011**, ISBN 978-1-4419-7200-2, doi:10.1007/978-1-4419-7200-2.

[79] D. Williams and C. Carter, *Transmission Electron Microscopy*, Springer Science, New York, USA, 2nd edition, **2009**, ISBN 978-0-387-76500-6.

[80] H. S. Park *et al.*, "Atomic-Scale Imaging in Real and Energy Space Developed in Ultrafast Electron Microscopy," *Nano Letters*, 7(9), 2545–2551, **2007**, doi:10.1021/nl071369q. PMID: 17622176.

List of Figures

List of Tables

Appendix

CONTENTS

A   UV Conversion Efficiency

The conversion of electromagnetic radiation to higher harmonics is a nonlinear process. Special birefringent crystals are used to perform this task. A prominent example is β-barium borate (BBO). The efficiency of the formation of high harmonics depends greatly on the photon density inside the material. Practically, a laser beam should be focused in the nonlinear crystal for optimum conversion.

In the case of the stroboscopic UTEM setup, only one part of the initial infrared laser is sent into the UV-module to be frequency quadruplicated. The conversion efficiency depends on the IR beam intensity. In fact, it scales nonlinearly. The graphs show the power of the two laser beams, the IR beam (not used for UV generation) and the resulting UV beam. The laser powers were measured for different rotations of a half wave plate which is located right before the UV module. In combination with a polarizing beam splitter, the position of the half wave plate defines fraction of IR which will be converted to UV. The measurements were done for a repetition rate of 500 kHz and 2 MHz.
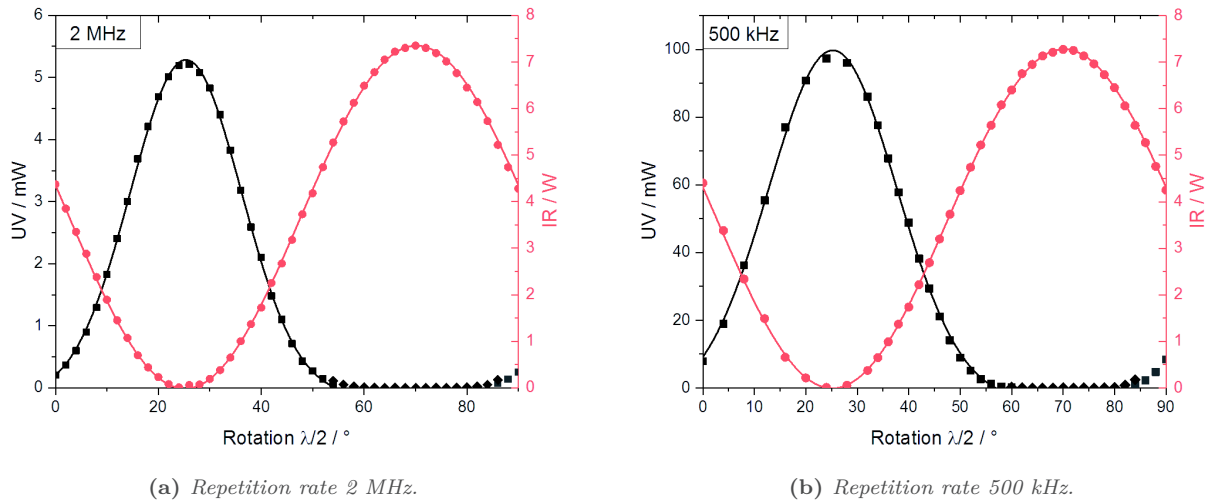

(a) *Repetition rate 2 MHz.*   **(b)** *Repetition rate 500 kHz.*

Figure A.1: *Power of infrared and ultraviolet beam as a function of the position of the half wave plate. The measurements were done at different repetition rates. Note the different scales for the UV power when comparing the graphs.*

B   Ray Path Simulations at different Wehnelt Bias Voltages

These simulations have been carried out by Sang Tae Park, scientist at Integrated Dynamic Electron Solutions, Inc., Pleasanton, CA, USA.

Parameter set:
- Cathode-Wehnelt gap: 800 µm
- Beam size at cathode: 100 µm
- Initial $E_{kin} = 0$
- Acceleration voltage: 200 keV
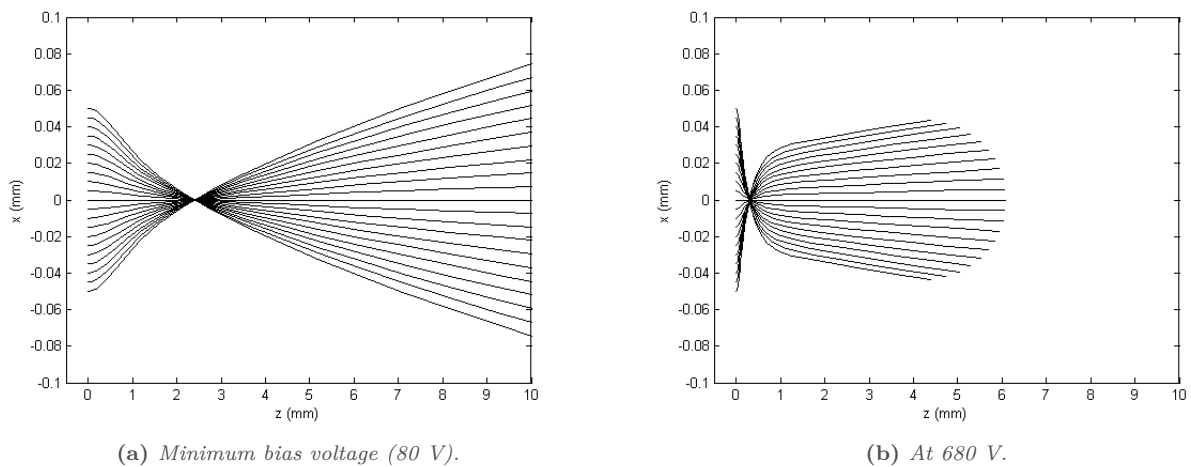- 21 electrons simulated in 31 time steps

(a) *Minimum bias voltage (80 V).*   (b) *At 680 V.*

Figure B.1: *Ray path simulations for different Wehnelt bias voltages show the influence on the position of the gun cross-over and the convergence of the electron beam. Note the different scales of x and z.*

Comparing the two scenarios, two aspects are striking. First, the gun cross-over is further away from the cathode at low bias voltage. This corresponds to the low lens strength when a low voltage is applied. Second, the electron beam diverges strongly at constant angular distribution at low bias. In contrast, a higher bias converges the beam again after the cross-over. Apparently, the electrostatic field of the Wehnelt does not only provoke the cross-over, but influences the beam beyond that point.

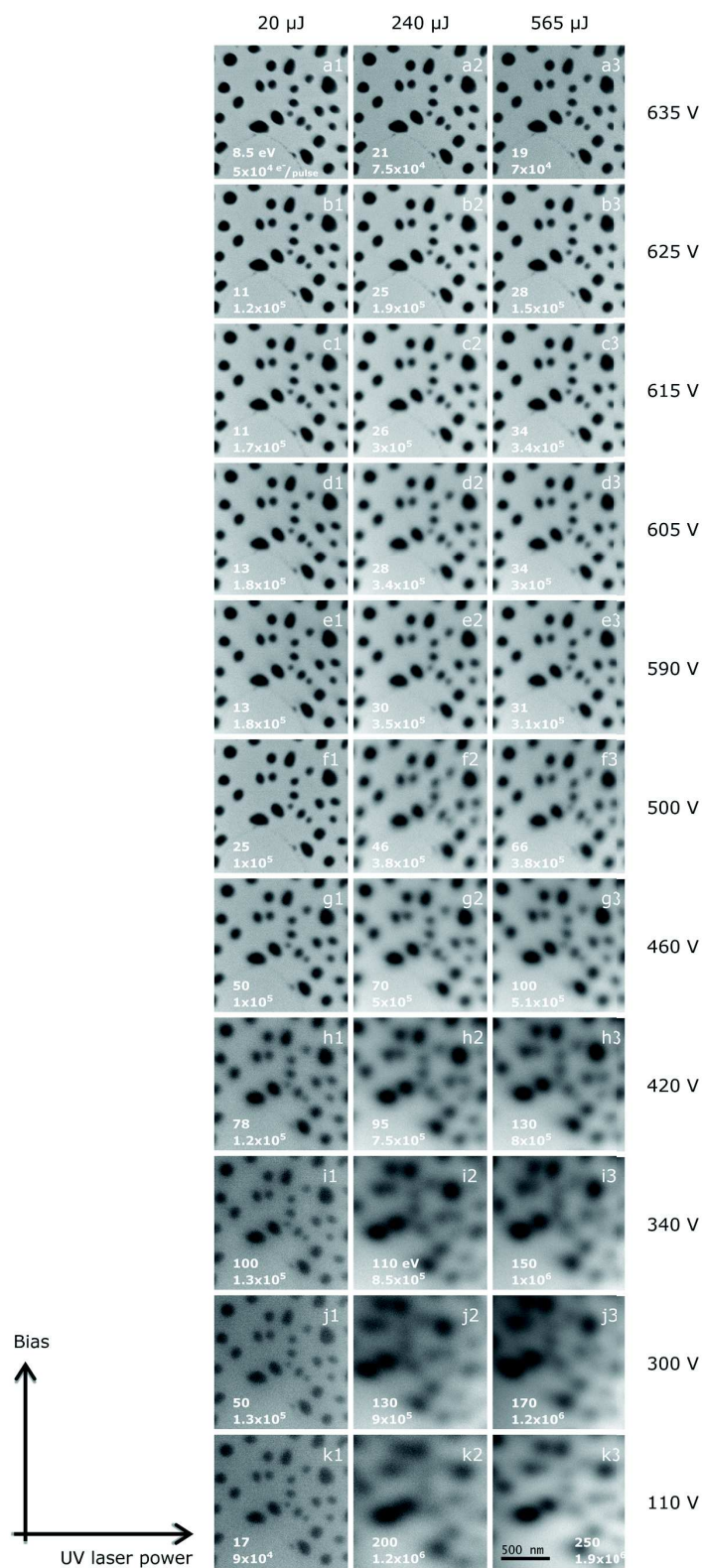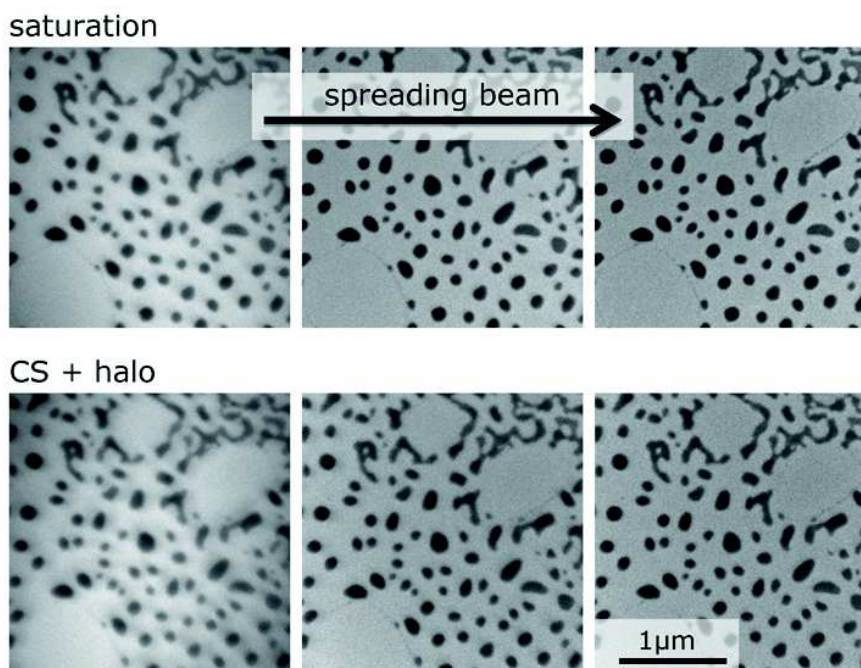# C   Imaging with Nanosecond Electron Pulses

Figure C.1: *Complete set of images taken with ns-electron pulses, changing the UV power and the Wehnelt bias. The energy width of accompanying EELS measurements is noted at the bottom of every image, together with the number of electrons per pulse.*
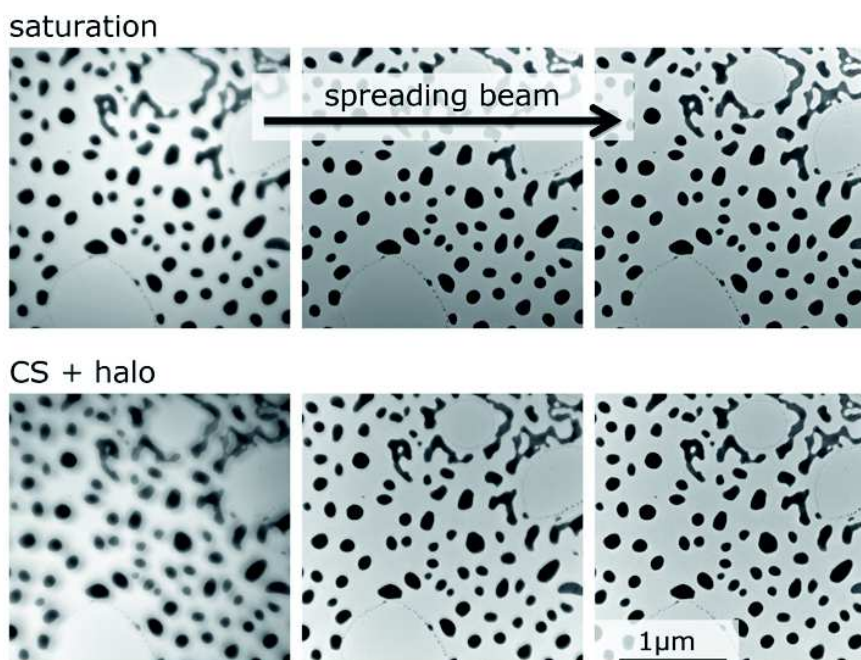
Figure C.2: *Influence of the electron beam spread on the spatial resolution. Image series are taken at two bias settings, which correspond to saturation (merged populations) and unsaturated emission (central spot and halo separated). UV pulse energy 20 µJ, at photoemission integration over 400 pulses. The comparison between ns-photoemission and thermionic emission show the same blurring, which proves spherical aberration as underlying phenomenon. The undersaturated, focused image shows a superposition of two images formed by the different populations which are focused on a different planes.*

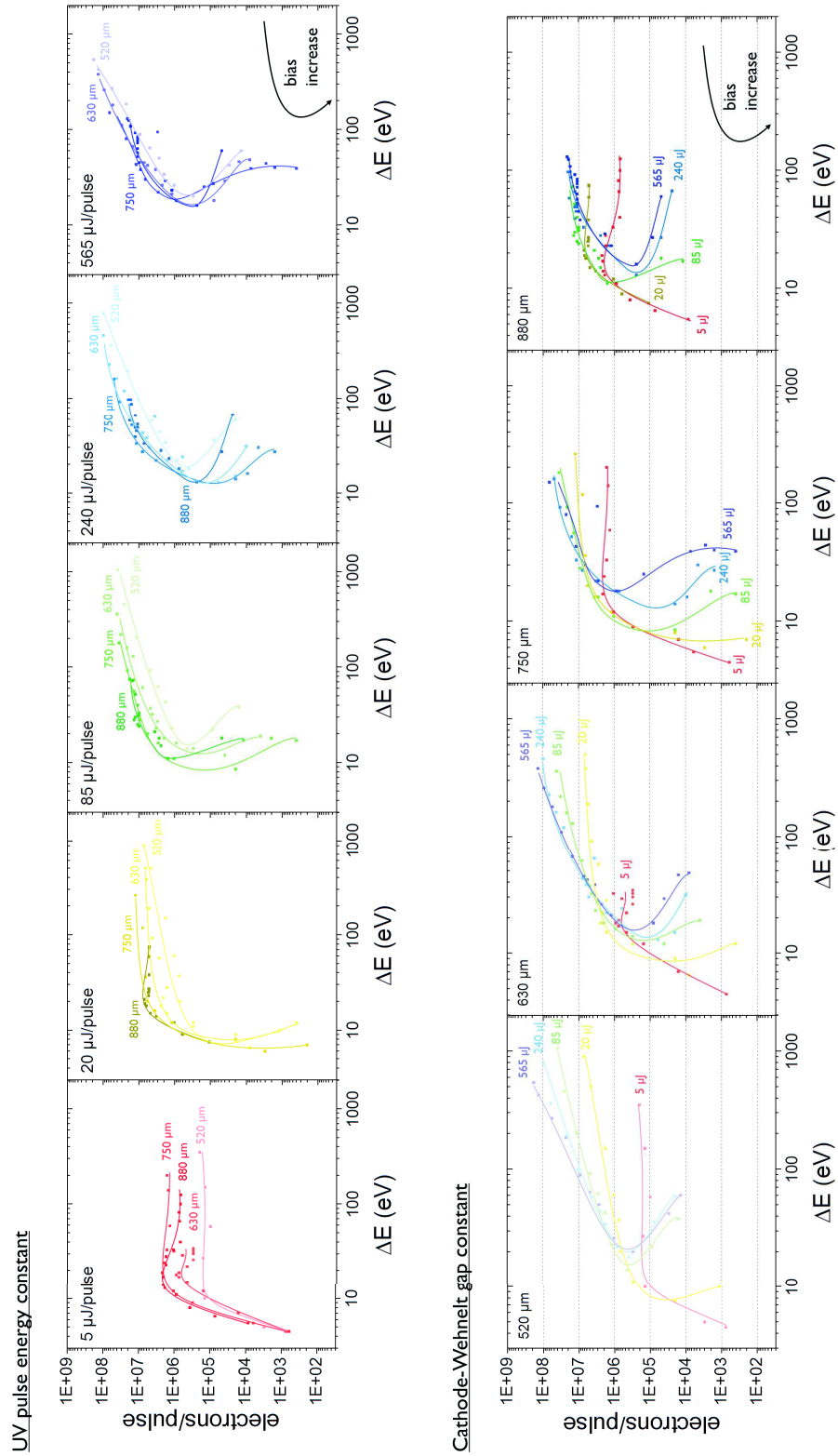# D   Parametric Study of Nanosecond Electron Pulses

Figure D.1: *Data set of the parametric study with ns-electron pulses, sorted by constant UV pulse energy and constant cathode-Wehnelt gap.*

Scientific Contributions resulting from this Thesis

Published Articles

"The Electron Dynamics in an Ultrafast Transmission Electron Microscope with Wehnelt Electrode", K. Bücker, M. Picher, O. Crégut, T. LaGrange, B. W. Reed, S. T. Park, D. J. Masiel, F. Banhart, *Ultramicroscopy*, 171, 8-18, **2016**, doi:https://doi.org/10.1016/j.ultramic.2016.08.014.

"Imaging and Electron Energy-Loss Spectroscopy using Single Nanosecond Electron Pulses", K. Bücker, M. Picher, T. LaGrange, F. Banhart, *submitted*.

Conference Contributions

Co-Organization

"Electron Microscopy with High Temporal Resolution" (EMHTR 2017)
May 29-31, 2017 in Strasbourg, France.

Oral Presentations

"Développement d'un Microscope Électronique en Transmission Ultrarapide", <u>K. Bücker</u>, M. Picher and F. Banhart; 23e Congrès Général de la Société Française de la Physique, Strasbourg, France, 2015.

"Design of a New Ultrafast Transmission Electron Microscope", <u>K. Bücker</u>, M. Picher and F. Banhart; Microscopy Conference, Göttingen, Germany, 2015.

Poster Presentations

"Design of a New Ultrafast Transmission Electron Microscope", F. Banhart, K. Bücker, M. Picher, T. LaGrange; 3rd International Conference on Ultrafast Structural Dynamics, Zurich, Switzerland, 2015.

"Ultrafast Transmission Electron Microscopy", F. Banhart, K. Bücker, M. Picher, T. LaGrange, B. Reed, S.T. Park, D. Masiel; Imaging with Femtosecond Electron and X-ray pulses, Trieste, Italy, 2016.

"Ultrafast Transmission Electron Microscopy reveals Electron Dynamics and Trajectories in a Thermionic Gun setup", K. Bücker, M. Picher, O. Crégut, T. LaGrange, B. Reed, S.T. Park, D. Masiel, F. Banhart; 16th European Microscopy Congress, Lyon, France, 2016.

"Ultrafast Transmisison Electron Microscopy", M. Picher, K. Bücker, F. Banhart; Session plénière du GDR Ultrafast Phenomena, Paris, France, 2016.

"The electron dynamics in ultrafast stroboscopic TEM", K. Bücker, M. Picher, T. LaGrange, B. Reed, S.T. Park, D. Masiel, F. Banhart; Electron Microscopy with High Temporal Resolution, Strasbourg, France, 2017.

"The characteristics of electron pulses in single-shot dynamic TEM", M. Picher, K. Bücker, T. LaGrange, B. Reed, S.T. Park, D. Masiel, F. Banhart; Electron Microscopy with High Temporal Resolution, Strasbourg, France, 2017.

Kerstin BÜCKER

Characterization of Pico- and Nanosecond Electron Pulses in Ultrafast Transmission Electron Microscopy

Résumé

Cette thèse présente une étude des impulsions électroniques ultra-brèves en utilisant le nouveau microscope électronique en transmission ultrarapide (UTEM) à Strasbourg. La première partie porte sur le mode d'opération stroboscopique, basé sur l'utilisation d'un train d'impulsions d'électrons de l'ordre de la picoseconde pour l'étude des phénomènes réversibles ultrarapides. L'étude paramétrique effectuée a permis de révéler les dynamiques fondamentales des impulsions électroniques. Des mécanismes inconnus jusqu'alors et décisifs dans les caractéristiques des impulsions ont été dévoilés. Il s'agit des effets de trajectoire, qui limitent la résolution temporelle, et du filtrage chromatique, qui impacte la distribution en énergie et l'intensité du signal. Ces connaissances permettent aujourd'hui un paramétrage affiné de l'UTEM de manière à satisfaire les divers besoins expérimentaux.

La deuxième partie concerne l'installation du mode d'opération complémentaire : le mode « singel-shot ». Ce mode fait appel à une impulsion unique d'intensité élevé et d'une durée de l'ordre de la nanoseconde pour l'étude des phénomènes irréversibles. L'UTEM de Strasbourg étant le premier instrument single-shot équipé d'un spectromètre de perte d'énergie des électrons (EELS), l'influence de l'aberration chromatique a pu été étudiée en détail. Elle s'est dévoilée être une limitation majeure pour la résolution en imagerie, nécessitant d'ajuster le bon compromis avec l'aberration sphérique d'une part et l'intensité du signal d'autre part. Enfin, la faisabilité de mener des études en EELS ultrarapide avec une seule impulsion nanoseconde a pu être démontrée, ceci constituant une première mondiale. Ce résultat très prometteur ouvre un tout nouveau domaine d'expériences résolu en temps.

Mots-clés : microscopie électronique en transmission ultrarapide, stroboscopique, single-shot, dynamique des impulsions électroniques

Abstract

This thesis presents a study of ultrashort electron pulses by using the new ultrafast transmission electron microscope (UTEM) in Strasbourg. The first part focuses on the stroboscopic operation mode which works with trains of picosecond multi-electron pulses in order to study ultrafast, reversible processes. A detailed parametric study was carried out, revealing fundamental principles of electron pulse dynamics. New mechanisms were unveiled which define the pulse characteristics. These are trajectory effects, limiting the temporal resolution, and chromatic filtering, which acts on the energy distribution and signal intensity. Guidelines can be given for optimum operation conditions adapted to different experimental requirements.

The second part starts with the setup of the single-shot operation mode, based on intense nanosecond electron pulses for the investigation of irreversible processes. Having the first ns-UTEM equipped with an electron energy loss spectrometer, the influence of chromatic aberration was studied and found to be a major limitation in imaging. It has to be traded off with spherical aberration and signal intensity. For the first time, the feasibility of core-loss EELS with one unique ns-electron pulse is demonstrated. This opens a new field of time-resolved experiments.

Keywords: ultrafast transmission electron microscopy, stroboscopic, single-shot, electron pulse dynamics